Illuminating the Potential of Thin-Film Photovoltaics

John K. Katahara

A dissertation

submitted in partial fulfillment of the

requirements for the degree of

Doctor of Philosophy

University of Washington

2017

Reading Committee:

Professor Hugh Hillhouse, Chair

Professor Guozhong Cao

Professor Daniel Gamelin, GSR

Professor Vincent Holmberg

Program Authorized to Offer Degree:

Chemical Engineering

University of Washington

Abstract

Illuminating the Potential of Thin-Film Photovoltaics

John K. Katahara

Chair of the Supervisory Committee:

Professor Hugh Hillhouse

Chemical Engineering

Widespread adoption of photovoltaics (PV) as an alternative electricity source will be predicated upon improvements in price performance compared to traditional power sources. Solution processing of thin-film PV is one promising way to reduce the capital expenditure (CAPEX) of manufacturing solar cells. However, it is imperative that a shift to solution processing does not come at the expense of device performance. One particularly problematic parameter for thin-film PV has historically been the open-circuit voltage (V_{OC}). As such, there is a pressing need for characterization tools that allow us to quickly and accurately evaluate the potential performance of solution-processed PV absorber layers. This work describes recent progress in developing

photoluminescence (PL) techniques for probing optoelectronic quality in semiconductors. We present a generalized model of absorption that encompasses ideal direct-gap semiconductor absorption and various band tail models. This powerful absorption model is used to fit absolute intensity PL data and extract quasi-Fermi level splitting (maximum attainable V_{OC}) for a variety of PV absorber technologies. This technique obviates the need for full device fabrication to get feedback on optoelectronic quality of PV absorber layers and has expedited materials exploration. We then use this absorption model to evaluate the thermodynamic losses due to different band tail cases and estimate tail losses in $Cu_2ZnSn(S,Se)_4$ (CZTSSe). The effect of sub-bandgap absorption on PL quantum yield (PLQY) and voltage is elucidated, and new analysis techniques for extracting V_{OC} from PLQY are validated that reduce computation time and provide us even faster feedback on material quality. We then use PL imaging to develop a mechanism describing the degradation of solution-processed $CH_3NH_3PbI_3$ films under applied bias and illumination.

ACKNOWLEDGMENTS

You hold in your hands (or on your hard drive, cloud, or some as-yet-uninvented data storage tool) the culmination of nearly six years of work. It has been a long journey to reach this point, and I wouldn't have made it here if not for the support and contributions of numerous people. I am grateful to my supervisory committee members—Prof. Vincent Holmberg, Prof. Guozhong Cao, and Prof. Daniel Gamelin—for their support during my graduate experience. You all pushed me to approach my research from different perspectives and helped me to plot my path forward even when the road wasn't that clear.

I would like to thank my research advisor, Prof. Hugh Hillhouse, for his guidance and mentoring. His involvement and enthusiasm in my work has been unparalleled, and has contributed immensely towards my professional and personal development. He has surrounded me with a suite of characterization tools that is at the cutting edge and with groupmates who are, objectively, the best in the world.

I am also indebted to many support staff at the University of Washington. Dr. Darick Baker, Duane Irish, Scott Braswell, and Gerry Hammer were all instrumental to my work on lateral devices and the hybrid perovskites. I would also like to thank Allison Sherrill, the ChemE graduate student advisor, for helping me through the last push to finish up my degree.

Thanks are also due to the wonderful students in the UW ChemE program. To my cohort (Matthew Crane, Kyle Caldwell, Dr. Edward Michor, Dr. Trevor Braun, and Dr. Mark Borysiak)—you all are the classiest gents I have ever met. I will forever have fond (and perhaps fuzzy) memories of late nights downtown capped, when possible, with a Seattle dog. Matt, Kyle, and William Voje Jr.—thank you for humoring my requests to play MTG every now and then.

Thanks also for always being willing to grab a cup of coffee (or beer) and commiserating with me on failed experiments or grad school craziness in general. Dr. Kevin Tan (a bioE, but still)—thanks for putting up with my shenanigans as a roommate. I owe you many future boba.

During my tenure in Seattle, I have had the good fortune to work alongside a phenomenal group of talented researchers and, more importantly, amazing human beings. We've laughed together, cried together, and weathered the highs and lows of this rollercoaster of emotions called graduate school. The best laid plans of mice and grad students often (always?) go awry, and you all helped me get through those inevitable setbacks:

Dr. Felix Eickemeyer—our overlap in the group has been relatively brief, but I've appreciated the perspective you've brought from your time in industry. Thank you for hosting some delicious group potluck/game nights and for getting us to appreciate the Seattle Peace Choir.

Kyle Harrigan—you remind me of myself from four years back (not sure if that's a good or bad thing). I've enjoyed discussing the merits of video game music and playing late night smash in Benson 109. May the soundtrack of your graduate experience include the emotional gravity of "Wind Scene" and the triumphant fanfare of Super Mario Bros' "Level Clear."

Ryan Stoddard—your boundless enthusiasm and passion for your experiments have energized me and kept me thinking about fun and interesting problems. Thank you for helping me out with making films for my lateral device work—you truly are a perovskite wizard. I've enjoyed discussing research and your outdoor adventures—always make time for those excursions.

Luke Huang—thank you for all your help with the PLQY setup. I know how difficult it can be to take charge of an instrument and calibrate it. Your hard work made my project on the hybrid perovskites possible to execute.

James A. Clark—your inquisitive nature and culinary talents have provided me with much food for thought (and for eating) over the years. I will never refer to a cookout as a BBQ again and will forever be a faithful adherent to the mustard-based school of BBQ sauces.

Warren Pinkard—you always inserted joy and humor into the day, whether it be through lunchtime discussions of things that shall not be repeated in print here or through Rocky references in your presentations. Thank you for showing me that some (many) things are more important than research and that you've got to make time for those important to you.

B. Wes Williamson—you are the most meticulous researcher I know, and I've regularly marveled at your attention to detail and hard work. In addition, you're a fantastic baker and a kind soul. I know that these traits will serve you well in the post-UW life.

Ian Braly—thanks for being such a good person and a delight to work with. I muddled about best I could with the PL calibrations and Mathematica coding, but things really took a step forward once you started working on these projects as well.

Sarah Vorpahl—I'm glad to have found another baseball fanatic in grad school (though somehow we never ended up at an M's game together). If your Cubs can win a World Series, then maybe getting through grad school isn't too tall an order.

Trevor Martin—thank you for being generous with your time and for helping me out with microscopy. I enjoyed collaborating on the Raman work with you and brainstorming on the crazy things you've seen with the polymers and nanocrystals. Get that diode!

Joe Zhou—your dogged optimism and tireless work ethic have served as inspiration to me. Thank you for encouraging me to keep things in perspective when I've encountered setbacks.

Dr. Christopher Wolcott—thank you for organizing weekend hikes and for single-handedly winning us trivia with your movie expertise. I didn't truly appreciate/understand your advice and comments at the time, but thank you for sharing your thoughts all the same.

Cori Bucherl—your effervescent laugh is identifiable in an instant. Thank you for guiding me in my role as symposium organizer and for injecting sunniness into the lab.

Dr. Hao Xin—I will be forever thankful that you joined the group when I did. You taught me so much about device fabrication, chemistry, and dumpling making.

Dr. Alexander Uhl—thank you for sharing your wealth of knowledge on the chalcopyrites, on research techniques in general, and on feuerzangenbowle. You are a wonderful teacher, and your future students will be lucky to have you as a mentor. Our trip to Phoenix for MRS will be one of my fondest memories in grad school. Let me know if you ever want to go off-roading again.

Dr. Robert McCarthy—thank you for teaching me the intricacies of glovebox maintenance and for helping me understand device physics. I'll treat you to your favorite, sushi, anytime.

Dr. Steven Gaik—I still tell stories of your handiness in lab and practical knowledge to this day. Thank you for teaching me about gas fittings and the finer points of sandwich-making. Thanks also for passing along pearls of wisdom about what it takes to make it through grad school.

Dr. Andrew Collord—your quick wit and dry humor made it a pleasure to come to lab each day. You are a lab hero, an inspiration, and a much-needed friend. There is no one I'd rather have in the trenches with me, making last-minute changes to a proposal at 4am, than you.

Dr. Susan Liu—thank you for being patient with me, even when I was extremely grumpy after tough days at lab. You could salvage any bad day solely with your smile. Somehow, we made it. The rest has to be easier than this, right?

Lastly I would like to thank my parents. I've missed birthdays and holidays back east due to the demands of lab, but you always welcome me back when I do find the time to get away. Thank you for loving me and for supporting me in all my endeavors. All of this work is possible because of you.

TABLE OF CONTENTS

LIST OF FIGURES

LIST OF TABLES

Chapter 1. INTRODUCTION

1.1 THE POTENTIAL OF SOLAR POWER

The world currently stands at a crossroads. A burgeoning population and concomitant increase in demand for energy is pitted against a world already strained by rapid industrialization and decades of consumption of vast amounts of carbon-based energy sources. The ancillary costs of coal-fired power plants (including pollution and exacerbation of climate change) are formidable and increase the pressure on society to pursue more sustainable energy pathways to development and growth. At the same time, there are pressures toward continued consumption, as the surplus of energy provided by hydrocarbons has driven technological advances and economic growth in the developed world. One must also consider the resources required to provide power and lift people out of poverty in the less developed regions across the globe.

One potential route to a more sustainable energy pathway would be an enhanced role of solar energy in global electricity generation. Solar power is an abundant energy resource, and some estimates peg the practically available power at 600-1000TW per annum.[1] This value is orders of magnitude larger than the average global electricity consumption in 2012 (2.24TW).[2] While there are significant challenges in energy storage and an outdated grid, our job in the solar community is to make photovoltaics (PV) more efficient and less expensive. If the economics make sense, then there will be continued growth in the global installed capacity of PV, allowing us to plot a sustainable course for generations to come.

1.2 Recent Progress in Photovoltaics

At the time of the writing of this dissertation, six years have passed since former Secretary of Energy Steven Chu rolled out the Department of Energy (DOE) SunShot Initiative (a convenient time point as it matches roughly with the start of the work detailed here). The goal in 2011 was to make solar energy competitive with conventional hydrocarbon-based sources of electricity by 2020. To compare prices between different energy technologies, the field has used the concept of levelized cost of electricity (LCOE):[3]

$$\text{LCOE} = \frac{\text{Lifecycle cost}}{\text{Lifetime energy production}} [=] \frac{\$}{\text{kWh}} \tag{1.1}$$

This metric compares the total cost of a technology (systems costs, maintenance, etc.) with the energy produced during the lifetime of the system. The SunShot goal aimed to reduce the LCOE of PV-derived electricity by nearly 75% during this time (a target of LCOE = \$0.09 per kWh for residential-scale PV, \$0.07 per kWh for commercial-scale PV, and \$0.06 per kWh for utility-scale PV). This initiative has injected millions of dollars of funding into hundreds of projects at the university-, government lab-, and industry-level in order to realize this vision.

Since 2011, there has been tremendous growth in PV. The annual PV installations in the US increased from roughly 2 GW in 2011 up to 7.26 GW in 2015, resulting in a total installed capacity of 29 GW of solar power. This increase in capacity has been accompanied by decreases in the cost of PV modules from \$3/W to \$0.75/W.[4] In 2016, the LCOE of utility-scale solar electricity had dropped to \$0.07/kWh (from \$0.27/kWh), leading DOE to release even more ambitious goals for 2030 (LCOE = \$0.05/kWh for residential-scale, \$0.04/kWh for commercial-scale, and \$0.03/kWh for utility-scale solar).

1.3 ENABLING A SOLAR-POWERED FUTURE

While we have made strides in making PV a feasible player in the American energy markets, there remains significant work to be done. It is imperative that solar-derived electricity reach grid parity with traditional energy sources in order for simple economics to drive market acceptance of PV. Such parity has been achieved in some locations even without subsidies (southwest US and Hawaii);[5] however, continued progress is needed in order for more widespread adoption of solar power.

Much of the recent decrease in PV pricing can be attributed to increase in polysilicon supply and improved economies of scale.[6] In order to realize the new SunShot goals for 2030, it will be necessary to push forward with more disruptive technologies. An important metric in evaluating potential technologies is the required capital expenditure (CAPEX).[7] CAPEX quantifies the amount of money a company must initially invest in order to construct a manufacturing plant (including all the equipment). It is often presented as the upfront investment divided by the annual manufacturing capacity in watts ($/$W_{aCap}$). In 2015, Powell and coworkers calculated a CAPEX of $1/$W_{aCap}$ for c-Si, which means that a 1 GW/year manufacturing plant would require an initial investment of $1 billion USD. High CAPEX presents a barrier to growth in the PV industry, and it is important that researchers work on ways to bring this value down. CAPEX can be reduced by increasing the efficiency of modules or by investing in less capital-intensive technologies. Powell *et al*. noted that CdTe offers some improvement in CAPEX compared to Si ($0.8/$W_{aCap}$ for a module with an efficiency of 12.8%). The biggest room for innovation in their view was for a solution-processed, roll-to-roll technology. If one were able to achieve a module efficiency of 15% for this type of processing, then the CAPEX would be reduced to

$0.06/$W_{aCap}$.[7] For this reason, an active area of research in the Hillhouse group has been to improve the efficiency of solution-processed PV technologies.

The efficiency of a device dictates the amount of PV-covered-area that is necessary to obtain a desired power. The power conversion efficiency (PCE) of a solar cell is dependent upon the short-circuit current density (J_{SC}), open-circuit voltage (V_{OC}), fill factor (FF), and the input power density (in this case the power density of the sun):

$$PCE = \frac{J_{SC} V_{OC} FF}{P_{Sun}} \tag{1.2}$$

As will be shown in the following chapter, one of the factors that limits the PCE of many PV technologies is the V_{OC}. The work presented in this dissertation details our efforts to develop a suite of characterization tools that enable rapid evaluation of the potential of solution-processed PV absorber layers. Such experiments allow us to identify promising technologies that will make PV cost-competitive with traditional sources of electricity.

In the next chapter, we will examine the best-case scenario for these device performance parameters and how real materials measure up to these limits.

Chapter 2. VOLTAGE AND LIGHT

The operation of a solar cell is an inherently non-equilibrium process. Illumination of the absorber layer leads to photoexcited carriers that build up across the forbidden gap. This distribution of carriers splits the Fermi level into two quasi-Fermi levels, one for the population of electrons in the conduction band and another for the population of electrons in the valence band (assuming quasi-thermal equilibrium—i.e. that the carriers within the bands experience scattering events that lead to fast thermal equilibration *within* the bands but not across the gap). The difference between these two levels, the quasi-Fermi level splitting ($\Delta\mu$), provides us with the maximum attainable V_{OC} for the absorber. There are reasons why actual device V_{OC} might deviate from this value (poor band alignment, damage during subsequent processing steps, etc.), but $\Delta\mu$ represents the inherent potential of the absorber layer. Thus, $\Delta\mu$ is an attractive parameter through which to evaluate and compare absorber materials or processing techniques. However, before we compare voltage characteristics between different materials, it is imperative that we have a framework with which to compare a material's actual performance to its maximum achievable performance. This discussion will begin with an overview of the thermodynamic limit of a single-junction solar cell, the so-called "Shockley-Queisser" limit.

2.1 Detailed Balance in Solar Cells

Since Sadi Carnot first revolutionized the way we thought about heat engines,[8] it has been commonplace for engineers to measure their devices against the theoretical limits imposed by thermodynamics. It makes little sense to devote resources into improving a device that is already at the limits of what can be attained. However, in the early years of PV research, such limits weren't clear, and researchers relied on a semi-empirical analysis to estimate the ceiling of PV

performance.[9,10] In 1961, Shockley and Queisser (SQ) published their seminal paper championing a detailed balance framework for modeling the upper limits of solar cell performance.[11] Their calculations considered an ideal absorber with step absorptivity (no absorption below the bandgap and perfect absorption above it), single exciton generation (each absorbed photon produces a single pair of excited carriers), perfect charge extraction (infinite carrier mobility), and band-band radiative pathways as the sole source of recombination. These assumptions highlight the fundamental, unavoidable[a] losses in a single junction solar cell: thermalization of high-energy carriers to the band edge; wasted photons (those below bandgap), thermodynamic losses, and radiative recombination. One additional assumption we will include here is that the device has a perfect back reflector, so there is no additional loss of radiative recombination out the back. Many technologies have a metallic contact with relatively high reflectivity, making this assumption the relevant case to consider for our purposes.

Assuming an ideal diode model for the current-voltage behavior of the solar cell and a diode quality factor of one, it is possible to calculate the V_{OC} from the photocurrent density, J_{ph}, and reverse saturation current density, J_0.

$$V_{OC} = \frac{kT}{q} \ln\left(\frac{J_{ph}}{J_0} + 1\right) \tag{2.1}$$

Here k is the Boltzmann constant, T is the absolute temperature, and q is the elementary charge. The photocurrent is dictated by the net absorbed photon flux that excites the solar cell:

$$J_{ph} = q \int_0^{\infty} \eta_c a(E) \varphi_{sun}(E) dE \tag{2.2}$$

[a] Discussion of 3rd generation photovoltaics is beyond the scope of this work.

Here η_C is the probability of collecting the excited carriers (assumed to be unity in the SQ case), a(E) is the spectral absorptivity, and $\varphi_{sun}(E)$ is the excitation flux. We shall use the AM1.5GT solar spectrum for the excitation flux.[12]

The reverse saturation current may be expressed as:

$$J_0 = q\int_0^\infty \varphi_e(E)dE \tag{2.3}$$

where the spectral blackbody emission flux at ambient temperature (T_a) is given by:

$$\varphi_e(E) = \frac{2\pi}{h^3c^2}\frac{a(E)E^2}{\exp\left(\frac{E}{kT_a}\right)-1} \tag{2.4}$$

Here h is the Planck constant, and c is the speed of light. We can plug these values into the ideal diode equation and numerically solve for the maximum power as a function of bandgap. Normalizing this power to the incident power under one-sun conditions, we obtain the quintessential SQ plot for PCE and V_{OC} as shown below.

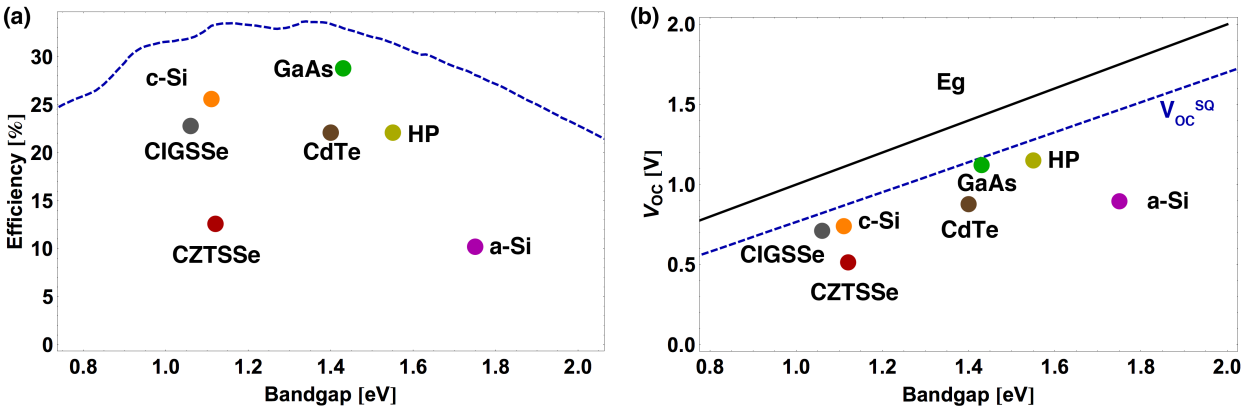

Figure 2.1. SQ limits under AM1.5GT ("one sun") excitation and ambient temperature of 298.15°K for (a) PCE and (b) V_{OC}. Champion values for selected technologies are presented underneath the detailed balance curves (dashed blue lines).

Included in these plots are the champion PCE and V_{OC} for selected technologies, including single crystalline Si (c-Si), amorphous Si (a-Si), GaAs, CdTe, Cu(In,Ga)(S,Se)$_2$ (CIGSSe),

$Cu_2ZnSn(S,Se)_4$ (CZTSSe), and hybrid perovskite (HP).[13,14] Of the PV technologies available currently, GaAs comes the closest to achieving its theoretical limits in V_{OC} and PCE. However, the manufacturing of high-quality GaAs is too expensive for terrestrial applications. CZTSSe and a-Si, technologies that are appealing due to their inexpensive raw materials and processing, experience the most severe voltage losses and lag behind other technologies in PCE.

CZTSSe is a relatively young technology (~20 years), while a-Si has been under development for 40 years. To put the performance of CZTSSe in perspective, we compare it to its chalcogenide kin CIGSSe, which has over 40 years of devoted research. In Figure 2.2 we plot the development history of these two thin-film PV technologies as described by the champion device PCE, V_{OC}, J_{SC}, and FF normalized to the detailed-balance limits.

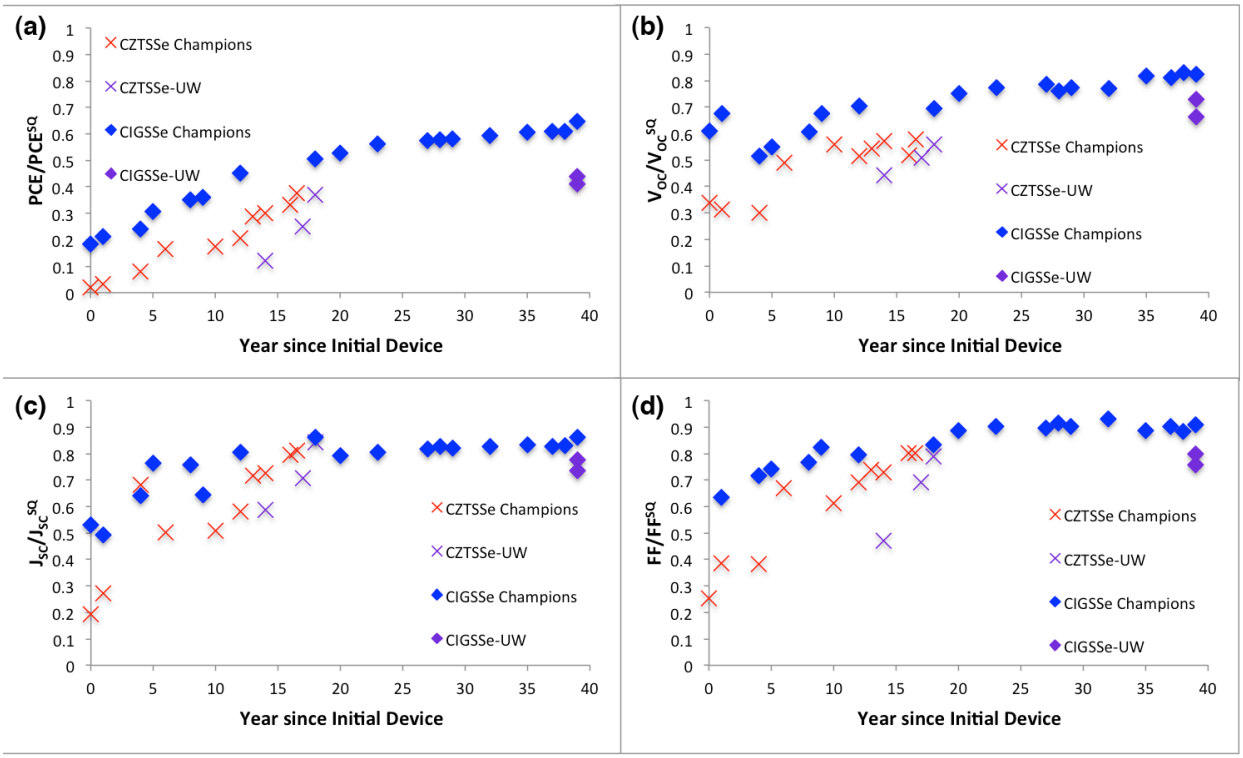

Figure 2.2. Historical progress in CIGSSe (blue diamond) and CZTSSe (red X) thin-film PV for champion device (a) PCE, (b) V_{OC}, (c) J_{SC}, and (d) FF. All values have been normalized to their SQ limits. Champion UW devices are also plotted for reference (purple markers).

Note that the abscissa is the time (in years) since the first device data was published in the literature.[b] CIGSSe, with over 40 years of active research dedicated to its development, is one of the top-performing thin-film PV technologies and has achieved PCE>22% in the lab scale.[13] CZTSSe, developed in response to concerns over indium scarcity and potential price volatility, has a record efficiency of only 12.6%,[15] well below where CIGSSe was at a comparable point in its development. Examining the specific performance parameters, it is clear that the main aspect holding back CZTSSe is the voltage. CZTSSe achieves less than 60% of the theoretical limit, and improvements in V_{OC} and PCE have stagnated in recent years. We also note that V_{OC} was the slowest parameter to achieve 80% of the SQ limit in CIGSSe. It is thus of prime importance that we develop tools that can quickly evaluate V_{OC} performance to accelerate the screening of new technologies and/or manufacturing processes.

When analyzing real materials, it is instructive to consider which ideal assumptions have broken down to explain losses in actual devices. This then allows us to identify research areas deserving of more extensive analysis. Rau and coworkers have succinctly summarized many extensions of detailed balance calculations to account for various non-idealities.[16] One ubiquitous loss is non-radiative recombination.

2.2 Radiative Efficiency and V_{OC}

The performance of a solar cell is greatly influenced by its ability to efficiently emit light. Having established the maximum V_{OC} and PCE obtainable when radiative band-band transitions are the only allowed recombination pathway, we turn our attention to the non-ideal (and more realistic) case when radiative efficiency is not perfect. Radiative recombination of photoexcited

[b] The CIGSSe timeline considers zero to be the publication of the thin-film polycrystalline device from the University of Maine. A single-crystal device (PCE=12%) was produced a year prior at Bell Labs.

electrons and holes is a fundamental process and cannot be turned off. However, defect-mediated recombination may be dramatically reduced by eliminating or passivating native point defects, impurities, and grain boundaries (all three commonly limit the open-circuit voltage in photovoltaics). Thus, the magnitude of the steady-state photoluminescence quantum yield (PLQY) of the semiconductor has been itself used as a metric of semiconductor quality or used to estimate the quasi-Fermi level splitting ($\Delta\mu$).

$$\eta_{ext} = \text{PLQY} = \frac{\text{Photons Emitted}}{\text{Photons Absorbed}} \tag{2.5}$$

This is of significant importance since the quasi-Fermi level splitting divided by the unit of fundamental charge (q) gives an upper estimate of the open-circuit voltage ($V_{OC} \leq \Delta\mu/q$) that a photovoltaic device may generate if it is the primary absorber and exposed to the same flux of above-bandgap photons. Alternate non-radiative recombination pathways reduce the PLQY. Losses in PLQY were shown to translate into decreases in maximum chemical potential (quasi-Fermi level splitting), $\Delta\mu$, by Ross.[17] Smestad then expressed this relation in terms of the V_{OC} of a solar cell as:[18]

$$\Delta\mu^{max} = qV_{OC}^{max} = qV_{OC}^{Rad} + kT\ln(\eta_{ext}) \tag{2.6}$$

Here η_{ext} is the external radiative efficiency (PLQY), and V_{OC}^{Rad} is the ideal radiative-limited V_{OC}, which in the simplest case is the SQ V_{OC}. Derivation starting from a photon balance at open-circuit conditions shows that the accuracy of the equation breaks down for $\eta_{ext} \leq \exp(-qV_{OC}^{Rad}/kT)$, but eq. 2.6 is a good approximation for $\eta_{ext} >> \exp(-qV_{OC}^{Rad}/kT)$. Note that at room temperature for a 1.5 eV bandgap semiconductor $\exp(-qV_{OC}^{Rad}/kT) \approx 10^{-21}$ for the SQ case, so this is not a serious restriction.

V_{OC}^{Rad} is a function of the incident spectrum, solid angle of incident light, the spectral absorptivity of the semiconductor, the solid angle of radiative emission, and the ambient temperature. There has been some recent debate over the correct expression for V_{OC}^{Rad} in the high-concentration limit,[19-21] but at lower concentrations, with emission into the full hemisphere above the semiconductor, and without effects of carrier multiplication or harnessing voltage from cooling of hot carriers, V_{OC}^{Rad} becomes the Shockley-Queisser V_{OC} (V_{OC}^{SQ}) if one assumes that the absorptivity is 1 above bandgap and 0 below bandgap.

$$\frac{\Delta\mu}{q} = V_{OC} = V_{OC}^{SQ} + \frac{kT}{q}\ln(\eta_{ext}) \tag{2.7}$$

Plotting this relation for a few representative bandgaps, we can see how a sub-unity PLQY degrades the attainable V_{OC}.

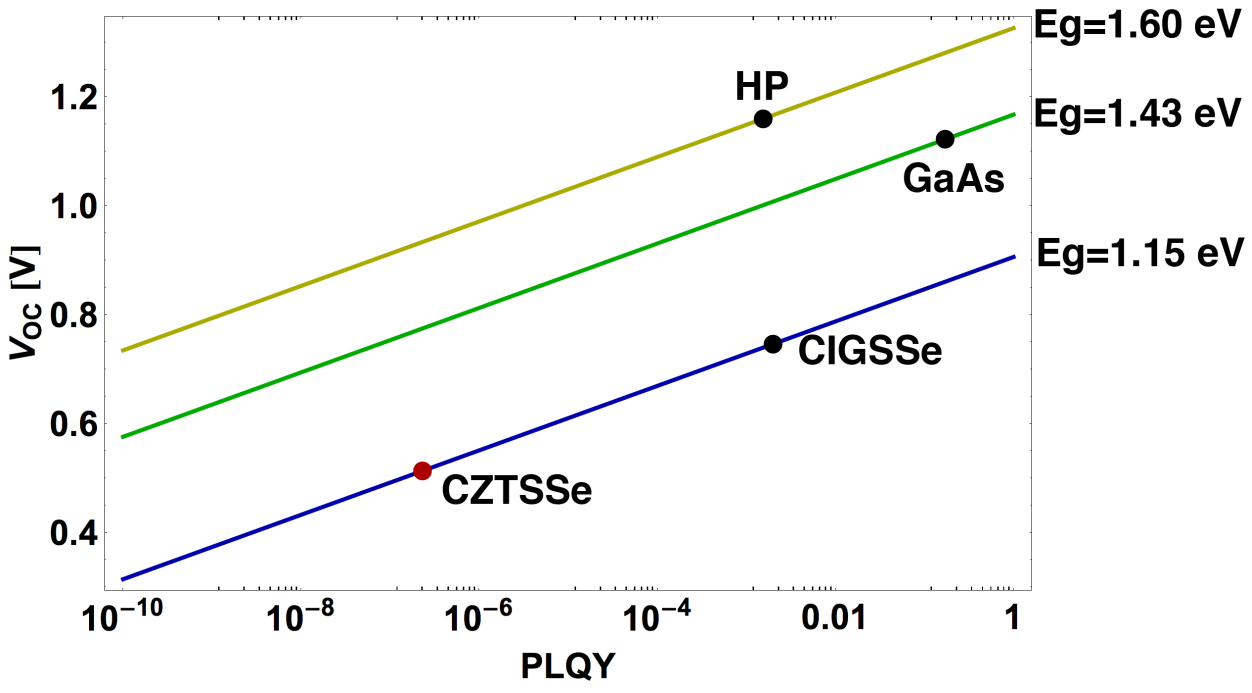

Figure 2.3. Simulated V_{OC} losses due to sub-unity PLQY (equation 2.6) for semiconductors with bandgaps ranging from 1.15 eV to 1.6 eV. Calculations assumed

AM1.5GT excitation and ambient temperature of 298.15 K. Discrete data points represent the PLQY corresponding to champion V_{OC} marks in select technologies for the case where all voltage losses were due to non-radiative recombination.

Included in this plot are points representing the high-water mark V_{OC} for key solar cell technologies and their associated radiative efficiency assuming that all losses in voltage can be attributed to non-radiative recombination. This plot highlights the importance of engineering solar cells to be efficient emitting materials. Recognizing this importance, researchers have achieved new records in V_{OC} and efficiency of GaAs solar cells by engineering better external photoluminescence efficiency.[22] However, most technologies have a PLQY well below 1%, and even a PLQY of 1% results in over a 100 mV loss in voltage for PV-relevant bandgaps.

2.3 CONCLUSIONS

In this chapter, we have grounded the discussion with a survey of the thermodynamic limits of solar cells. This framework gives us the best-case scenario for PV performance, which we can then compare to real devices. From these results, it is clear that achieving high V_{OC} remains a problem for many PV technologies, which directs us to luminescence techniques as a way to probe internal potentials. We will now move on to our contributions in quantifying specific optoelectronic losses in non-ideal solar cells.

Chapter 3. QUASI-FERMI LEVEL SPLITTING AND SUB-BANDGAP ABSORPTIVITY FROM SEMICONDUCTOR PHOTOLUMINESCENCE

3.1 INTRODUCTION

The capacity for photoemission of a material is inextricably linked with the capacity for photoabsorption. van Roosbroeck and Shockley (vRS) famously demonstrated the relationship between the volumetric rate of *internal* spontaneous radiative emission and the spectral absorption coefficient at thermal equilibrium.[23] Later, Lasher and Stern[24] and Würfel[25] generalized the vRS result to express the non-equilibrium *external* flux of spontaneous radiative emission in terms of the spectral absorptivity and $\Delta\mu$. This "Lasher-Stern-Würfel" (LSW) equation is:

$$I_{PL}(E) = \frac{2\pi E^2}{h^3 c^2} \frac{1}{\exp\left(\frac{E-\Delta\mu}{kT}\right) - 1} a(E) \; [=] \; \frac{\text{photons}}{\text{area}\cdot\text{time}\cdot\text{bandwidth}} \tag{3.1}$$

This equation is the product of three factors: (1) the photon density-of-states for emission into the full hemisphere above the semiconductor surface, (2) Bose-Einstein distribution, and (3) the spectral absorptivity.

The LSW equation provides an excellent avenue through which to analyze the externally emitted absolute intensity photoluminescence (AIPL) provided that the absorption spectrum is known. Unfortunately, models of above-bandgap absorption alone are unsuitable for use in the above equation, as many new and exciting PV materials have sub-bandgap absorption and sub-bandgap PL. In addition, there has been no consensus on a general way to treat sub-bandgap

absorption in materials. Models of disorder, both compositional and positional in nature, have been discussed and a variety of functional forms proposed. Werner and Rau looked at electrostatic potential and bandgap fluctuations and their effect on a detailed balance limit applied to CIGSe.[26,27] Assuming a Gaussian distribution of bandgaps due to local inhomogeneities, they obtain a smeared absorptivity with increasing sub-band absorption for larger fluctuations.[28] However, the functional form of this sub-bandgap absorption does not fit the observed PL for the materials in this study.

Here we develop a generalized theory of sub-bandgap absorption. Furthermore, we note that the absorption coefficient buried in the absorptivity in eq. 3.1 is not the conventional absorption coefficient that is simply related to the joint density-of-states (DOS). In this equation, the absorption coefficient and the absorptivity are occupation dependent (as noted by Würfel and emphasized by Bhattacharya *et al.*).[29,30] As a result, we develop a simplified expression for the photoluminescence spectral flux that accounts for occupation explicitly, allowing one to use absorption coefficient models based on DOS (i.e. the ideal square-root dependence above bandgap for a direct bandgap semiconductor and other DOS models of sub-bandgap absorption). We then combine these two new theoretical formulations and compare our theory to measured AIPL for GaAs, CIGSSe, and CZTSSe.

3.2 Theory of Sub-Bandgap Absorption

Sub-bandgap states in absorption spectra (so called "band tails") have been of interest in disordered materials since Urbach first noted the simple exponential tailing of absorption spectra in AgBr crystals:[31]

$$\alpha(E) \sim \exp\left(-\frac{E - E_1}{E_0}\right) \tag{3.2}$$

E_1 is a characteristic energy of transition, and E_0 is an energy parameter that dictates the width of the tail (the so-called Urbach Energy). This type of behavior has been used to analyze absorption in semiconductors like GaAs (E_0~5-10meV) as well as amorphous Si (E_0~50meV).[32] There have been a variety of proposed mechanisms behind the simple exponential band tails of these materials, including dynamic thermal disorder and internal electric-field induced absorption. Sa-yakanit and Glyde demonstrated that disorder on the scale of the interatomic bond length could explain Urbach tails regardless of the source of disorder.[33] As the length scale of disorder increased, they found that the tail states decayed more rapidly than a simple exponential.

Behavior encompassing a sharper decay of tail states has been analyzed for heavily doped materials.[34-36] A general treatment using a semiclassical approach to determine the density-of-states (and DOS-based absorption coefficient) of heavily doped semiconductors was simultaneously realized by Bonch-Bruevich,[37] Keldysh,[38] and Kane.[39] Using this semiclassical (Thomas-Fermi) approach, Kane showed that the functional form of the tail states is given by a Gaussian: [40]

$$\alpha(E) \sim \exp\left(-\left(\frac{E - E_1}{\sqrt{2}\sigma}\right)^2\right) \tag{3.3}$$

Here σ is the root-mean-square depth of the potential well created by the charged impurity distribution: $\sigma = \frac{e^2}{4\pi\varepsilon\varepsilon_0}(Nr_0)^{1/2}$, where N is the average impurity density, ε is the dielectric constant, and r_0 is the screening length**.** It should be noted that this model overestimates deep tails because it doesn't account for quantum effects (the spacing of discrete energy levels actually increases as the potential well narrows).[36]

Shklovskii and Efros demonstrated that the functional form of the absorption coefficient may deviate from the Thomas-Fermi result for certain cases.[41] They found that for potential

fluctuations of magnitude less than the screening length, the absorption coefficient does not exhibit Gaussian behavior but rather a 5/4 exponential dependence on energy. This screened Thomas-Fermi approach yields an absorption coefficient with the following functional form:

$$\alpha(\mathrm{E}) \sim \exp\left(-\frac{2}{5\sqrt{\pi}}\left(\frac{\mathrm{E}-\mathrm{E}_1}{\mathrm{E}_0}\right)^{\frac{5}{4}}\frac{1}{(\mathrm{N_t a^3})^{\frac{1}{2}}}\right) \tag{3.4}$$

where N_t is the total number of charged impurities, E_0 is the impurity binding energy, and a is the Bohr radius. Dirnstorfer *et al.* related N_t to a tunneling barrier, which allowed them to express the potential fluctuations affecting luminescence in the following form:[42]

$$\gamma_{\mathrm{opt}}^5 = \left(\frac{\mathrm{e}^2}{4\pi\varepsilon\varepsilon_0}\right)^4 \frac{\mathrm{N_t^2}\hbar^2}{\mathrm{m_e}} \tag{3.5}$$

Band tails have also been attributed to photon-assisted tunneling (the Franz-Keldysh effect) in the presence of electric fields (from charged impurities).[43,44] Tharmalingam noted that the absorption due to tunneling in the presence of a constant electric field could be expressed in terms of Airy functions.[45] In the limit of energies far below the band edge, the asymptotes of the Airy functions result in absorption related to an exponential of energy to the 3/2 power. Duke and Alferieff examined the effects of the Coulombic interaction of the electron and hole on optical transitions in the presence of an electric field and found the same asymptotic dependence.[46] Summarizing, the energy dependence of the absorption coefficient for the Franz-Keldysh effect may be expressed as follows:[47]

$$\alpha(\mathrm{E}) \sim \exp\left(-\frac{\sqrt{2\mathrm{m_e^*}}}{3\mathrm{e}\mathrm{E}\hbar}(\mathrm{E}-\mathrm{E}_1)^{3/2}\right) \tag{3.6}$$

Here $\mathcal{E}$ is the electric field, which can be externally applied or due to the internal fields from a distribution of charged impurities. Dow and coworkers derived the same form when using the theory of internal electric microfields to consider band-acceptor luminescence.[48]

A different approach for examining the DOS deep in the tail was taken by Halperin and Lax, who used a numerical technique (minimum counting method).[49] They found that Gaussian statistics result in a DOS related to exponential energy dependence of powers ranging from 0.5 to 2.0 depending on the range over which the potential is felt. Sa-yakanit *et al.* applied Feynman Path Integrals to obtain analytic expressions for the Halperin & Lax model and were able to express the exponential energy dependence continuously from 0.5 for short-range disorder to 2.0 for long-range disorder.[33]

In addition to these models, a model of sub-bandgap absorption based on inhomogeneities in bandgap has been proposed by Mattheis, Rau, and Werner.[28] For a Gaussian distribution of bandgaps occurring over small length scales (compared to the carrier diffusion length), they showed that a complementary error function could describe the absorptivity both above and below the average bandgap. One can then plug this absorptivity model into the LSW equation. However, this model imposes significant restrictions on the shapes of absorption and luminescence spectra due to the assumption of a Gaussian distribution of bandgaps.

Despite the numerous competing theories to describe band tails in disordered systems, there have been few experimental studies. Lee and coworkers fit full-spectrum PL from n-type GaAs of varying dopant levels using a Gaussian distribution of tailing states.[50] They did not use the LSW equation to fit their data and provide limited description of their fitting procedure. Their model reproduces the PL data for highly doped GaAs:Si but exhibits deviations for lower doping levels.

Dirnstorfer *et al.* used the screened Thomas-Fermi model to fit the sub-bandgap absorption spectra from CIGSe and to extract an estimate of the charged impurity concentration and potential fluctuations.[42] They reported increasing potential fluctuations as samples became more Cu-poor. Siebentritt *et al*. examined the PL from $CuInSe_2$ and $CuGaSe_2$ and fit the low energy tail for "Defect" and "Tail" models to extract the amplitude of fluctuations.[51] In their nomenclature, the Defect model corresponds to Gaussian sub-bandgap DOS tails while the Tail model indicates Urbach behavior. They claim that with increasing deviation from stoichiometry the Gaussian DOS better fit the data.

More recently, Gokmen *et al*. have used 5/4 and Gaussian models to examine fluctuations in hydrazine-synthesized $Cu(In,Ga)(S,Se)_2$ (CIGSSe) vs. $Cu_2ZnSn(S,Se)_4$ (CZTSSe) and the effects on device efficiency.[52] They extract absorption data from internal quantum efficiency (IQE) measurements and fit the low-energy tail of ln(1-IQE) data to examine the amplitude of fluctuations. Fits from both models indicate that the CZTSSe samples suffer from larger disorder than the CIGSSe samples.

As evident from the above discussion, there is no consensus on the appropriate interpretation or analysis of absorption coefficients in the presence of sub-bandgap absorption. In addition, the ubiquity of band tailing in material systems as diverse as GaAs,[53] a-Si,[54] CIGSSe,[55] and CZTSSe[56,57] demonstrates the need for a broadly applicable approach. In the next section, we develop a general model of absorption that encompasses the above descriptions as limiting cases.

3.3 General Model of Sub-Bandgap Absorption

Given the copious experimental data showing sub-bandgap absorption, the simple parabolic band density-of-states model for the ideal direct-gap absorption coefficient is insufficient to

describe real materials. However, it is not immediately evident that any of the previously discussed models can be universally applied for all material systems. Here, we note that most of the proposed functional forms of tail states are related to a decaying exponential of varying magnitude. We take inspiration from Kane's original semiclassical treatment for Gaussian tail states[58] and derive a model of DOS-based absorption coefficients that convolute the sub-bandgap states with an ideal model for band-band transitions:

$$G(E) = \int_{-\infty}^{\infty} g_{tail}(E')g_{ideal}(E - E')dE' \tag{3.7}$$

One may substitute any model for the ideal DOS. For the materials in this study, we will use the square-root dependence of the joint-density-of-states that results from parabolic bands of a direct-bandgap semiconductor. For the sub-bandgap tail states, we propose a general functional form:

$$g_{tail}(E) = N \exp\left(-\left|\frac{E - E_1}{\gamma}\right|^{\theta}\right) \tag{3.8}$$

E_1 is a characteristic energy of emission, taken to be the bandgap for band-band transitions. The decay of the tail states depends on the exponent θ and the energy broadening parameter γ. N is a normalization constant that is determined by requiring the integral of $g_{tail}(E)$ from positive to negative infinity be equal to 1:

$$N \int_{-\infty}^{\infty} \exp\left(-\left|\frac{E - E_1}{\gamma}\right|^{\theta}\right) dE = 1$$

Integration shows that:

$$N=\frac{1}{\gamma\, 2\, \Gamma\left(1+\frac{1}{\theta}\right)}$$

where Γ is the standard mathematical Gamma function. This normalization is required for asymptotically matching the absorption coefficient above bandgap and ensures that the tail states do not change the overall strength of absorption above bandgap. Here, θ may vary between 0.5 and 2.0, reflective of the Halperin & Lax and Sa-yakanit treatment of band tails.[49,59] The discrete values of 1.0, 1.25, 1.5, and 2.0 may reduce to the following analytic models: Urbach (γ = Urbach energy), screened Thomas-Fermi (γ proportional to the 2/5 root of the total charged impurity concentration), Franz-Keldysh (γ proportional to internal electric field), and Thomas-Fermi cases (γ proportional to the root-mean-square magnitude of potential fluctuations, which is in turn proportional to the square root of the charged impurity concentration), respectively. However, we note that the model is agnostic towards the mechanism behind the tailing behavior, and data fitted to an exponent of 3/2 does not prove that an internal Franz-Keldysh effect is present.

Convoluting this tail model with an ideal square-root dependence of the DOS above the bandgap and introducing a change of variables ($\Delta E=E'-E_1$), we obtain the following expression for the DOS:

$$G(E)=\frac{1}{\gamma 2\Gamma(1+1/\theta)}\int_{-\infty}^{\infty}\left(\exp\left(-\left|\frac{\Delta E'}{\gamma}\right|^{\theta}\right)\sqrt{(E-E_1)-\Delta E'}\right)d\Delta E' \tag{3.9}$$

For θ = 2.0, this equation reduces exactly to the full Thomas-Fermi density of states as derived by Kane.[40] This fact becomes clear if we recast the density-of-states in terms of the energy difference: $\Delta E = E - E_1$.

$$G(\Delta E)=\frac{1}{\gamma 2\Gamma(1+1/\theta)}\int_{-\infty}^{\Delta E}\exp\left(-\left|\frac{\Delta E'}{\gamma}\right|^{\theta}\right)\sqrt{\Delta E-\Delta E'}\,d\Delta E'$$

(3.10)

Here we have replaced the upper limit of the integral to avoid introducing complex values from the square-root term.

The absorption coefficient is proportional to the DOS and the matrix element relating the initial and final states. This matrix element is absorbed into a constant α_0, which is a material-dependent parameter that characterizes the strength of the direct transition (α_0 is typically in the range of 10^4 to 10^5 $cm^{-1}eV^{-0.5}$ but depends on the oscillator strength). This leaves a simple expression for the absorption coefficient:

$$\alpha(E) = \alpha_0 G(E)$$

(3.11)

Note that it has been assumed that the energy ranges of interest are small such that the usual 1/E dependence in the denominator of the absorption coefficient will not significantly affect the absorption. With this model for the absorption coefficient, the absorptivity may be calculated:

$$a(E) = 1 - \exp(-\alpha(E)d)$$

(3.12)

Here d is the characteristic length scale over which carriers are generated, travel, and recombine radiatively. For simplicity we neglect the contribution of reflection from the top surface, but spectral reflectivity data can be included if needed or available for a sample. The extent of sub-bandgap absorption may be quantified by integrating the absorptivity below bandgap and normalizing to the bandgap, which we define as the average sub-bandgap absorptivity, $\bar{a}_{SB}$:

$$\bar{a}_{SB} = \frac{1}{E_g}\int_0^{E_g} a(E)dE \tag{3.13}$$

For an ideal material with no tail states, this value would be zero. A comparison of the absorption behavior from this general model for limiting cases of θ is presented in Figure 3.1. To compare the different exponent cases, γ is chosen to produce equivalent sub-bandgap absorptivity (eq. 3.13) among the various curves. As can be seen in Figure 3.1, the functional form of the model has a powerful effect on the behavior of the sub-bandgap absorption, with higher exponents θ resulting in curves that decay more rapidly at energies below the bandgap.

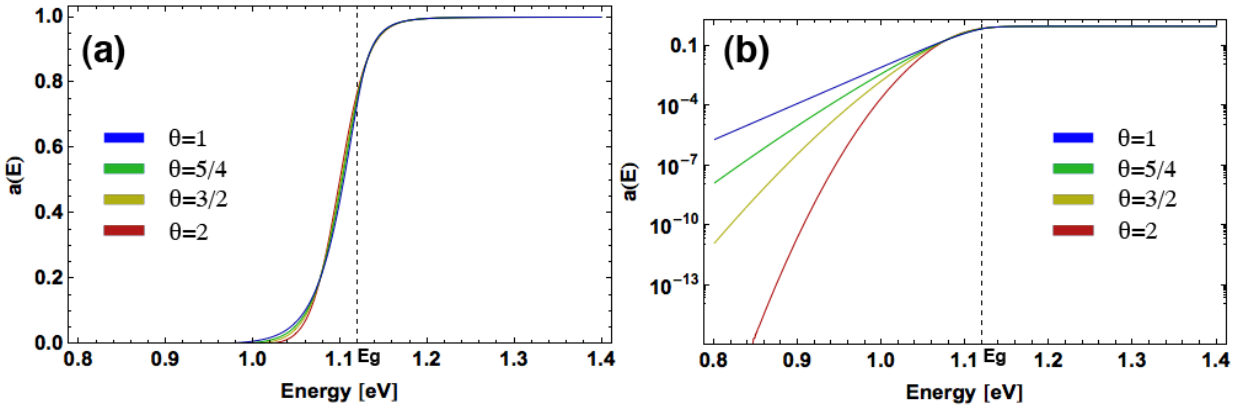

Figure 3.1. (a) Absorptivity curves for limiting cases of exponent with γ values for each case to create equivalent fraction of sub-E_g absorption ($\bar{a}_{SB} = 2.3 \times 10^{-2}$). (b) Same curves as (a) but plotted on logarithmic scale.

Further, we compared our general model of sub-bandgap absorption with the Gaussian distribution of bandgaps model.[28] Our general model can yield very similar absorption coefficients, However, it results in values of θ greater than 2.0 and did not fit the experimental data in the materials examined in this study.

3.4 SIMULATING PHOTOLUMINESCENCE SPECTRA

3.4.1 *Effect of Non-Zero Band Occupation*

Having established a general model for semiconductor absorption, we return to a discussion on the reverse process—radiative recombination. The connection between photon absorption and emission at equilibrium was first recognized by Kirchhoff in 1860.[60] In 1917, Einstein then articulated the principle of the detailed balance in terms of absorption, stimulated emission, and spontaneous emission between two discrete levels in terms of coefficients B_{12}, B_{21}, and A_{21} (the "Einstein coefficients").[61] In this detailed balance, the rates of absorption (transition from state 1 up to state 2) and emission (transition down from state 2 to state 1) will be the same.

$$\begin{gathered} R_{12} = R_{21} \\ n_1 B_{12} \rho_E(E) = n_2 A_{21} + n_2 B_{21} \rho_E(E) \end{gathered} \tag{3.14}$$

Here n_1 and n_2 are the carrier populations in the ground and excited states, respectively. ρ_E is the photon density-of-states given by Planck's Law.[62]

$$\rho_E(E) = \frac{8\pi E^3}{h^3 c^3 \left(\exp\left(\frac{E}{kT}\right) - 1\right)} \tag{3.15}$$

Shortly thereafter, Kennard showed that the fluorescence emission could be related to the coefficient of absorption and the black body spectrum.[63,64] However, it wasn't until 1954 that van Roosbroeck and Shockley (vRS) revealed the exact form of spontaneous emission from band transitions in terms of the absorption coefficient (α) and refractive index of the emitting material (n_r):[23]

$$R(E) = \frac{8\pi n_r^2}{h^3 c^2} \frac{E^2 \alpha(E)}{\exp\left(\frac{E}{kT}\right) - 1} \; [=] \; \frac{\text{photons}}{\text{volume·time·bandwidth}} \tag{3.16}$$

Note that in this equation, R(E) is the spectrally resolved rate of *internal* photon emission per unit volume *at thermal equilibrium*.

Later, Lasher and Stern generalized the vRS result for emission under non-equilibrium conditions in terms of the quasi-Fermi level splitting, $\Delta\mu$:[24]

$$R(E) = \frac{8\pi n_r^2}{h^3 c^2} \frac{E^2 \alpha(E)}{\exp\left(\frac{E - \Delta\mu}{kT}\right) - 1} \tag{3.17}$$

Note that the Lasher-Stern formulation is valid only when quasi-thermal equilibrium holds, which is the condition where exactly two different effective or "quasi" Fermi energies accurately describe the energy dependence of the two separate populations of electrons in the conduction band and valence band, resulting in one "quasi-Fermi level splitting." In addition, this form was demonstrated to be applicable for band to impurity transitions.[65]

Würfel[25] then extended the Lasher-Stern generalization to show that the *external* flux of radiative emission could be related to the spectral absorptivity of the material (see eq. 3.1 above). This expression dramatically simplifies the analysis of data since it focuses only on the emission that escapes the material. The generalization holds true under the assumption of Lambertian emission into a medium with refractive index close to unity.[66] The Lasher-Stern-Würfel equation has been referred to in the literature as a generalized Kirchhoff law or generalized Plank law.[67]

Here, we note that the LSW equation diverges at $E = \Delta\mu$ unless the absorptivity is rigorously zero when the photon energy equals the $\Delta\mu$, which is unphysical. We resolve this issue by noting that the absorption coefficient in the vRS equation and the LSW equation are not the familiar density-of-states based absorption coefficients, but are highly occupation dependent functions as emphasized by Bhattacharya *et al.*:[30]

$$\alpha(E) = \alpha_{0K}(E)(f_V - f_C)$$

(3.18)

Here f_v and f_c are the occupation probabilities of the valence band and conduction band, respectively, and α_{0K} is the absorption coefficient accounting only for the joint DOS (eq. 3.11). This correction accounts for the effect of occupation of the conduction and valence bands on absorption probability at non-zero temperatures and excitation. Accounting for occupation, we arrive at the following expression for the PL spectral flux:

$$I_{PL}(E) = \frac{2\pi}{h^3c^2}\frac{E^2\left(1-\exp(-\alpha_{0K}(E)(f_V-f_C)d)\right)}{\exp\left(\frac{E-\Delta\mu}{kT}\right)-1}$$

(3.19)

The occupation probabilities can be expressed using the Fermi-Dirac distributions:

$$f_V = \frac{1}{\exp\left(\frac{E_v-E_{Fv}}{kT}\right)+1}$$
$$f_C = \frac{1}{\exp\left(\frac{E_c-E_{Fc}}{kT}\right)+1}$$

(3.20)

Here, E_v and E_c are energy levels in the valence and conduction bands, respectively, not the band edge energies. It is convenient to express f_C and f_V in terms of a single quasi-Fermi level splitting (E_{Fc}-E_{Fv}) and the energy of the optical transition (E_c-E_v), which is equal to the photon energy ($h\nu$). If we consider the case where the electron and hole effective masses are equal and the material is intrinsic, then the quasi-Fermi energies will split symmetrically about the intrinsic equilibrium Fermi energy at $E_g/2$. While this is not a good approximation for a doped semiconductor at low injection, it becomes a good approximation even for doped semiconductors at high injection. Since it is at high injection where we expect effects from occupation, this is generally a reasonable assumption. For simplicity, we take the zero of energy to be $E_g/2$. If we consider any single photon absorption event, we may express E_c and E_v and E_{Fc} and E_{Fv} as a

function of a parameter, p, which characterizes how the excess photon energy (the portion greater than E_g) partitions between exciting electrons higher into the conduction band and holes deeper into the valence band:

$$E_c = \frac{E_g}{2} + p\left(h\nu - E_g\right)$$

$$E_{Fc} = \frac{\Delta\mu}{2}$$

$$E_v = -\frac{E_g}{2} - (1-p)(h\nu - E_g)$$

$$E_{Fv} = -\frac{\Delta\mu}{2}$$

(3.21)

p = 1 represents excitation from the valence band maximum to an energy level in the conduction band, ($h\nu$-E_g) greater than the conduction band minimum. p = 0 represents an excitation from an energy level in the valence band, ($h\nu$-E_g) lower than the valence band maximum, up to the conduction band minimum. The average value of p over many absorption events depends on the density-of-states in each band. However, if the density-of-states is similar in each band and each increases going from the band edge into the band, then p will average to about 1/2. It is exactly 1/2 when the effective masses are equal. For this case, the expressions above simplify:

$$E_c = \frac{h\nu}{2}$$

$$E_{Fc} = \frac{\Delta\mu}{2}$$

$$E_v = -\frac{h\nu}{2}$$

$$E_{Fv} = -\frac{\Delta\mu}{2}$$

(3.22)

Plugging these into f_V and f_C and letting E without subscripts be the transition energy, E = hν:

$$f_C = \frac{1}{\exp\left(\frac{E-\Delta\mu}{2kT}\right)+1}$$
$$f_V = \frac{1}{\exp\left(-\frac{E-\Delta\mu}{2kT}\right)+1} \tag{3.23}$$

Thus the Fermi occupation factor for net absorption with equal effective masses and symmetric splitting of the quasi-Fermi energies is:

$$f_V - f_C = 1 - \frac{2}{\exp\left(\frac{E-\Delta\mu}{2kT}\right)+1} \tag{3.24}$$

Plugging this correction into the LSW equation, we obtain the following:

$$I_{PL}(E) = \frac{2\pi}{h^3c^2}\frac{E^2}{\exp\left(\frac{E-\Delta\mu}{kT}\right)-1}\left(1-\exp\left(-\alpha_{0K}d\left(1-\frac{2}{\exp\left(\frac{E-\Delta\mu}{2kT}\right)+1}\right)\right)\right) \tag{3.25}$$

Note that $\left(1-\exp(-x)\right) \to x$ when x is close to zero. Also note that $(f_v - f_c) \to 0$ when $E \to \Delta\mu$. When $E \approx \Delta\mu$, one can perform a Taylor expansion on the absorptivity, and:

$$\left(1-\exp(-\alpha_{0K}(E)(f_v-f_c)d)\right) \sim \alpha_{0K}(E)(f_v-f_c)d \tag{3.26}$$

Farther away from $E = \Delta\mu$ this becomes a poor approximation. However, taking the absorptivity with no occupation effects and multiplying it by the Fermi occupation factor gives the absorptivity the correct functional form when $E > \Delta\mu$ but is still accurate at $E = \Delta\mu$ (and removes the pole in PL). We thus arrive at a much simpler approximate form where the familiar density-of-states based absorption coefficient (eq. 3.11) may be used:

$$I_{PL}(E) = \frac{2\pi}{h^3c^2}\frac{E^2\left(1-\exp(-\alpha_{0K}(E)d)\right)}{\exp\left(\frac{E-\Delta\mu}{kT}\right)-1}\left(1-\frac{2}{\exp\left(\frac{E-\Delta\mu}{2kT}\right)+1}\right) \tag{3.27}$$

We can evaluate the validity of our simplifications by simulating PL spectra, as shown in Figure 3.2a.

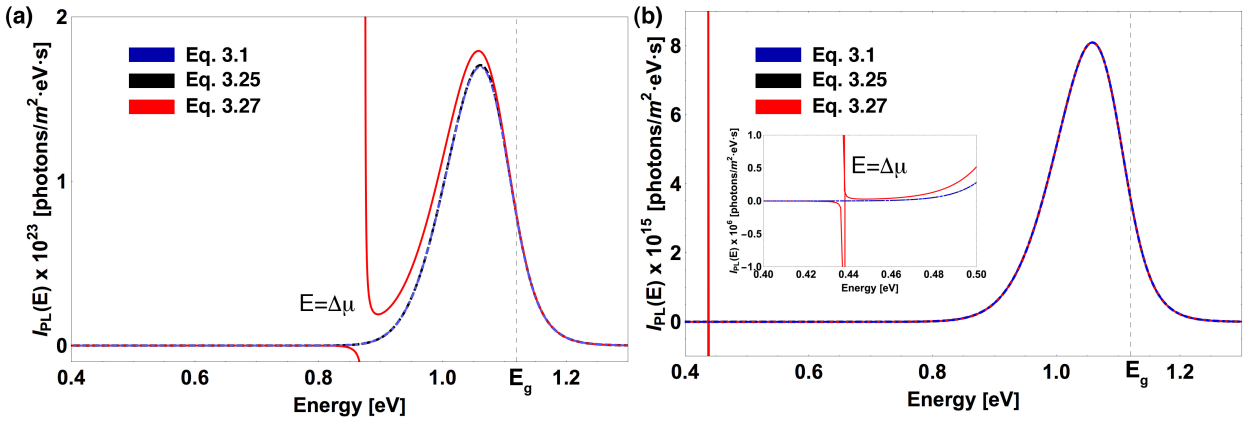

Figure 3.2. (a) Simulated PL curves for high Δμ the LSW equation (red), LSW modified with occupation correction—eq. 3.25 (black), and LSW with the Taylor expansion in eq. 3.27 (blue). (b) Simulated PL curves at low Δμ for the same cases as (a). Inset presents a magnification of the pole at E = Δμ. Note the good agreement for all models for energies near the peak of luminescence.

In the case of good material quality and high Δμ or high injection conditions, the equation ignoring the occupation dependence of the absorption coefficient leads to an unphysical peak with a pole at E = Δμ. The models accounting for occupation effects for an intrinsic material with symmetric quasi-Fermi level splitting remove this pole. There is a very slight deviation at the crown of the peak for the model using a Taylor expansion (eq. 3.27), but overall this simplification does not lead to significant issues. Figure 3.2b presents luminescence for the various models at low Δμ. All three models converge into a single curve at energies relevant for

PL observation. At these photon energies (far away from Δμ), all the models reduce to a Wien-like form with a non-occupation dependent absorptivity with good accuracy:

$$I_{PL}(E) = \frac{2\pi E^2}{h^3 c^2} a_{0K}(E) \exp\left(-\frac{E - \Delta\mu}{kT}\right) \tag{3.28}$$

The exp(-(E-Δμ) /kT) factor (which dominates the E^2 factor) grows rapidly as energy decreases and must be balanced by a stronger exponential decay of the absorptivity. The balancing of these competing processes makes the proper treatment of absorption, especially for energies below the bandgap, imperative.

In order to avoid the complexity of fitting the entire spectrum, previous studies have fit only the high-energy tail of photoluminescence spectra to extract Δμ.[68,69] For energies far enough above bandgap, the absorptivity is close to 1, which allows one to rearrange equation 3.28 to obtain an expression where Δμ is related to the y-intercept of the logarithm of the photoluminescence spectral flux in the high-energy tail. Using this procedure, the authors show a close match of the V_{OC} and Δμ for CIGSe devices. However, as we show below, there can be a significant dependence of the extracted Δμ on the choice of fitting region, even when above bandgap. In addition, it can be difficult to experimentally measure sufficient luminescence intensity above bandgap for materials with significant band tailing. For such materials, usage of the general model for sub-bandgap absorption developed here is necessary.

3.4.2 *Effect of Absorption Model on Photoluminescence*

The application of the proposed tail-state model for the absorptivity has profound implications on the PL spectra as defined by the LSW equation (eq. 3.1) and its simplifications (eq. 3.25 and eq. 3.27). The classical description of the absorption coefficient for parabolic bands would result

in an asymmetric peak above bandgap and an abrupt cessation of luminescence at all energies below bandgap. Real materials exhibit markedly different PL behavior, and the failure of the classical model is exemplified in Figure 3.3.

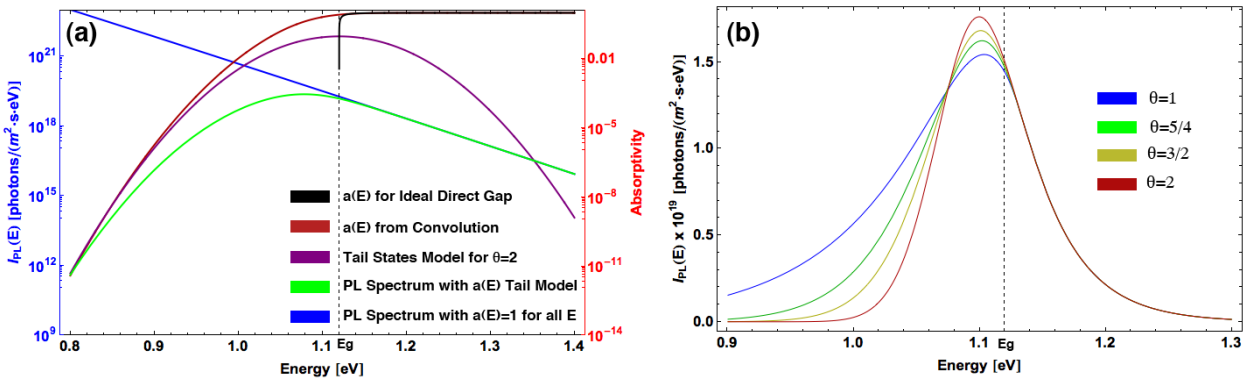

Figure 3.3. (a) PL and absorptivity curves for θ = 2 in the convolution model for tailing states. The low energy limit of the absorptivity (Gaussian tail states) and PL spectrum assuming an absorptivity of 1 for all energies are shown as well. (b) Simulated PL spectra generated for limiting cases of the exponent and T = 400 K, $\Delta\mu$ = 0.5 eV, and E_g = 1.12 eV. The γ parameter has been chosen such that $\bar{a}_{SB} = 2.30 \times 10^{-2}$ for all cases.

Figure 3.3a displays both the simulated PL as well as absorptivity on logarithmic scales. At energies far above bandgap, the absorptivity model reproduces the simple square-root behavior for direct-gap semiconductors. At energies far below the bandgap, the model matches the exponentially decaying DOS. Note how the convolution exhibits different behavior from the asymptotes at energies close to the bandgap, which is the range where many of the previous fitting procedures operate. The PL is dominated by the absorptivity at low energies (below bandgap) and by the Bose-Einstein term at high energies above the bandgap. Figure 3.3b presents PL spectra generated for limiting cases of θ for the tail states model. The curves exhibit different shapes as well as slight changes in peak position, a summary of which can be found in Table 3.1. The asymmetry factor is a reflection of the skew of the peak towards the high-energy side for values less than one and to the low energy side for values greater than one. It is defined

as the HWHM (half-width at half maximum) at high energy divided by the HWHM at low energy.

Table 3.1**.** Peak shape characteristics for the PL curves generated in Figure 3.3b.

θ	γ [meV]	FWHM [meV]	Asymmetry	Peak Shift from Bandgap [meV]
1	25.0	127	0.61	16.4
5/4	34.0	105	0.834	18.1
3/2	40.8	95.7	0.986	19.1
2	49.6	86.1	1.19	20.4
1	25.0	127	0.61	16.4

Note that the magnitude of the peak redshift from bandgap increases from $\theta = 1$ to 2 (at constant $\bar{a}_{SB}$). Furthermore, a larger γ is required to generate the same $\bar{a}_{SB}$ for larger exponents. This result makes sense intuitively because tail states governed by higher exponents decay more rapidly than those for exponents closer to one. From this exercise, it is clear that the power of the exponential decay of DOS below the bandgap has a significant effect on the shape of the PL. In addition, the proposed model is able to produce curves of diverse shapes without considering the convolution of multiple peaks; the shape is completely determined by the LSW equation and the general model for absorption coefficient with sub-bandgap states. However, this model is only appropriate when there is a single peak, which precludes the treatment of spectra with significant shoulders or multiple features.

3.5 Experimental Section

3.5.1 *Instrumentation*

Photoluminescence spectra were acquired using a modified Horiba LabRAM HR-800. A 785nm laser diode was used as the excitation source. An Olympus MPlan achromat 10x objective (NA=0.25, FN=22) was used to focus the excitation on the sample as well as collect

the emitted light. A 150 gr/mm Czerny-Turner monochromator blazed at 1200 nm was used to spectrally resolve the luminescence, after which the emitted light was passed to a liquid nitrogen-cooled InGaAs array detector. The system was continuously purged with dry air to remove H_2O absorption artifacts in the NIR range of the emission spectra.

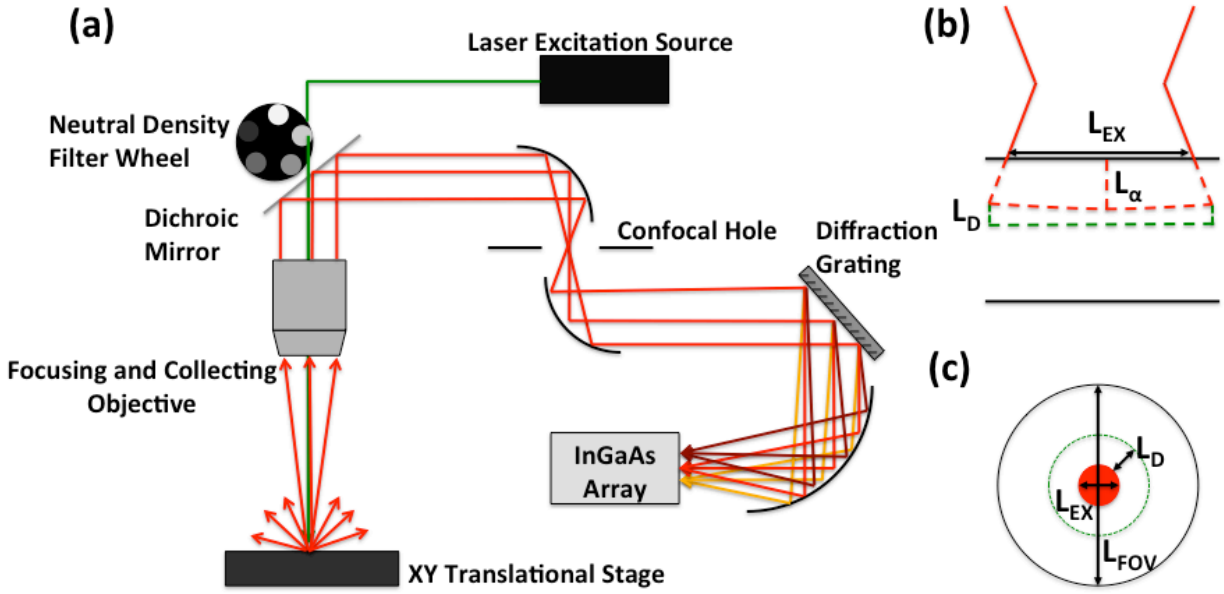

Figure 3.4. (a) Experimental apparatus for confocal micro-photoluminescence. (b) Cross section view of illuminated sample showing length scales of absorption and diffusion. (c) Top down view of the illuminated sample showing length scales of excitation, diffusion and collection.

As demonstrated in panels 4(b) and (c), the relative length scales of the width of excitation, depth of absorption, length of carrier diffusion, and range of photon collection (field-of-view) are of great importance in the proper treatment of PL data. Let us first examine the situation of poor minority carrier diffusion lengths compared to the excitation diameter ($L_{ex}>>L_D$). We use a Field of View (FOV) far larger than both the excitation and diffusion length scales ($L_{FOV}>>L_{ex}>>L_D$). In this case, the vast majority of photons emitted by the sample will be collected (accounting for the NA of the objective), and the local non-equilibrium carrier concentrations will be comparable

to those for uniform excitation because the carriers stay relatively localized to where they were generated.

Consider the opposite case where we have a diffusion length on the order of or larger than the width of excitation ($L_{FOV}>>L_D>>L_{ex}$). In this case, all the photons are once again collected, but the non-equilibrium carrier populations are lower than expected from the area of excitation (effectively, there is a lower injection level and a lower quasi-Fermi level splitting).

A third case is possible for materials of high quality and diffusion lengths on the order of or larger than the FOV ($L_D>>L_{FOV}>>L_{ex}$). For this case, some (and possibly a significant number) of the photons will not be collected because the carriers diffuse and recombine far away from the initial excitation area. In this worst-case scenario, the quasi-Fermi level splitting would be significantly underestimated. Thus, it is important to choose a setup with a large enough field of view to efficiently collect emitted photons accounting for the diffusion length or to use large area uniform excitation.

For the experimental setup used here, the width of excitation was approximately 40 μm, and the FOV was orders of magnitude larger at 2.2mm. Note that the diffusion lengths in kesterite and chalcopyrite materials are generally on the order of a few microns (or less), making this effect negligible relative to the excitation area. We note that it is possible to raster the laser spot over a wide sample area in order reduce local heating of the sample. If this is employed, it is important that the L_{FOV} be much larger than the raster area to avoid issues of photon collection at the edges of the raster area.

3.5.2 *Relative and Absolute Calibration*

Relative spectral corrections were used to account for imperfect transmission/reflection of optical path elements (objective lens, edge filter, mirrors, etc.), the efficiency of the

monochromator, and responsivity of the detector. A NIST-calibrated blackbody source (IR-301, Infrared Systems Development Corporation) was set to 1000 °C and placed below the objective lens. Radiation from the blackbody was then collected through the exact same optical path used for PL collection. A relative-intensity spectral correction file was created to match the signal from the detector to the theoretical shape of the blackbody at the set temperature. Alternatively, a calibrated quartz tungsten halogen lamp from Avantes (Avalight-HAL-CAL-mini) was used for spectral calibrations at shorter wavelengths.

Absolute intensity calibrations were accomplished using the same blackbody source but with a 10 μm aperture to precisely set the spectral flux of photon emission reaching the instrument. This rate of photon emission was compared to the count rate of detection from the InGaAs array to generate a conversion factor for counts to emitted photons.

An Oriel optical power meter was used to measure the illumination intensity incident upon the sample for various laser settings. A CCD camera was used to measure the width of excitation from the laser.

The absolute intensity PL data was analyzed using a nonlinear least squares fit to equations 3.19 and 3.27. Tables of the G(E) function, equation 3.19, for exponents of 0.5 to 2.0 were generated in 0.05 increments. These tables were then used to create an interpolation function for use in fitting to reduce the computation time. A Levenberg-Marquardt algorithm was used in the nonlinear fitting to extract $\Delta\mu$, T, E_g, γ, and θ. $\Delta\mu$ and T both appear in the exponential term in the denominator of the LSW equation. As a result, they are strongly coupled. E_g, γ, and θ are all involved in the convolution of the absorptivity. γ and θ are also strongly coupled.

The samples investigated using this method were a molecular precursor CZTSSe device,[70] a nanocrystal CIGSSe device,[71] and a Zn doped p-GaAs (N_a = 2.1 x $10^{17}cm^{-3}$) wafer provided by Professor R. Rafaelle at the Rochester Institute of Technology.

3.6 Results and Discussion

For materials like CIGSSe and CZTSSe that have large rates of non-radiative recombination, the d in the absorptivity is simply the sum of the absorption length at the wavelength of excitation and the minority carrier diffusion length. Using literature values for the absorption lengths (~1.5 μm) and diffusion length (6.7μm) of p-type GaAs, the α_0*d product is approximately 30 to 50.[72,73] For chalcopyrites, the diffusion lengths are generally lower, on the order of 1-2 μm. For kesterites, the diffusion lengths are typically below 1μm. Using absorption data calculated by Persson for CZTSe and CISe, we obtain α_0*d products on the order of 10-20 for both our kesterite and chalcopyrite samples.[74] Note that an overstimation of the α_0*d product forces the model to fit the data for emission from larger depths than the emission actually ocurred. This would lead to a small overestimation of the magnitude of tail states. For materials without pre-existing estimates for these lengthscales, one can leave α_0*d as an additional fitted parameter.

3.6.1 *Fitting of PL Spectra from GaAs, CZTSSe, and CIGSSe and Connection to Directly Measurable Parameters*

Having established that this model for sub-bandgap absorptivity may be used to generate PL curves more similar to those emitted from real materials, we turn our attention to fitting PL data to extract information on the material quality and tail states. As a proof of principle, we first

looked at the well-characterized system of p-GaAs.[75] Figure 3.5 presents PL data and fits for GaAs as well as the absorptivity extracted from PL.

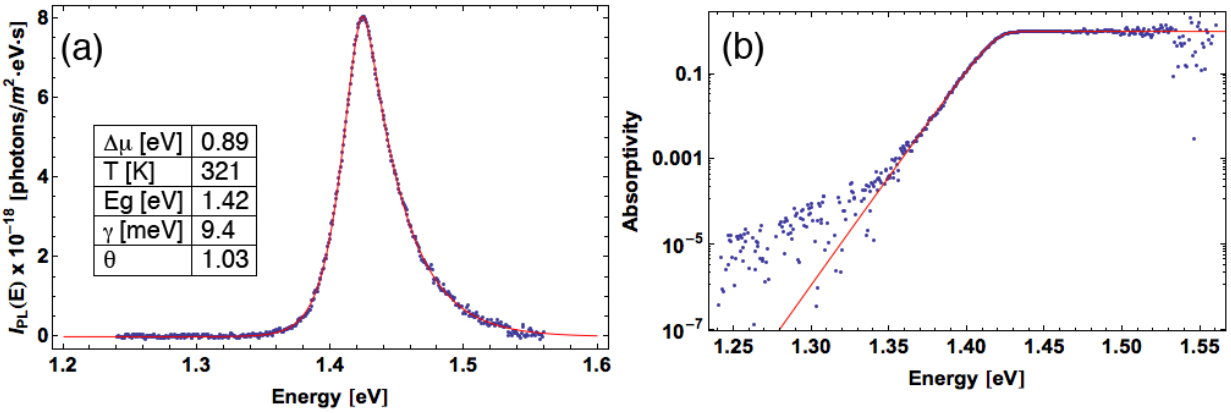

Figure 3.5. (a) PL (blue points) and full-spectrum fit (red curve) of p-GaAs. (b) Absorptivity extracted from the PL data by using the Δμ and T from the full-spectrum fit and solving for the absorptivity term (as defined by eq. 3.12 using eq. 3.9 and 3.11 with the correction from eq. 3.18) in eq. 3.27 (blue points). The absorptivity from the proposed model of tail states using the fitted θ, E_g, and γ is shown by the red curve. The average sub-bandgap absorptivity is 7.06 x 10^{-3}.

Data were collected at approximately 16 suns-equivalent excitation. Note the excellent match between the modeled PL and the data (R^2>0.999). The bandgap value of 1.42 eV is in good agreement with literature values for GaAs. The temperature indicates there is moderate local heating and is on the same order as the temperature extracted by Lee and coworkers in their fit of n-GaAs.[50] In addition, the exponent from the fit is close to 1, which is the limiting case for Urbach tails, identical to the behavior that others have found for III-V materials.[53] The γ of 9.4meV is in line with the Urbach energies that previous studies have observed for GaAs.[32] The match between the extracted parameters of the full-spectrum fit and literature values for GaAs validates the model's applicability to high quality direct-gap semiconductors. Note that there is deviation between the absorptivity extracted from the PL and that from the modeled tail states (Figure 3.5b). This discrepancy could be due to a second functional form of gap states not

accounted for by the model. Another possibility is that the slight discrepancy could simply be an artifact from background subtraction used for absolute intensity calibration of the detector.

Having demonstrated the utility of the proposed model of DOS and absorption for fitting GaAs data, we extend the analysis to the more complicated chalcopyrite and kesterite systems. Figure 3.6 presents the optoelectronic characterization of a CIGSSe nanocrystal and a CZTSSe molecular precursor solar cell.

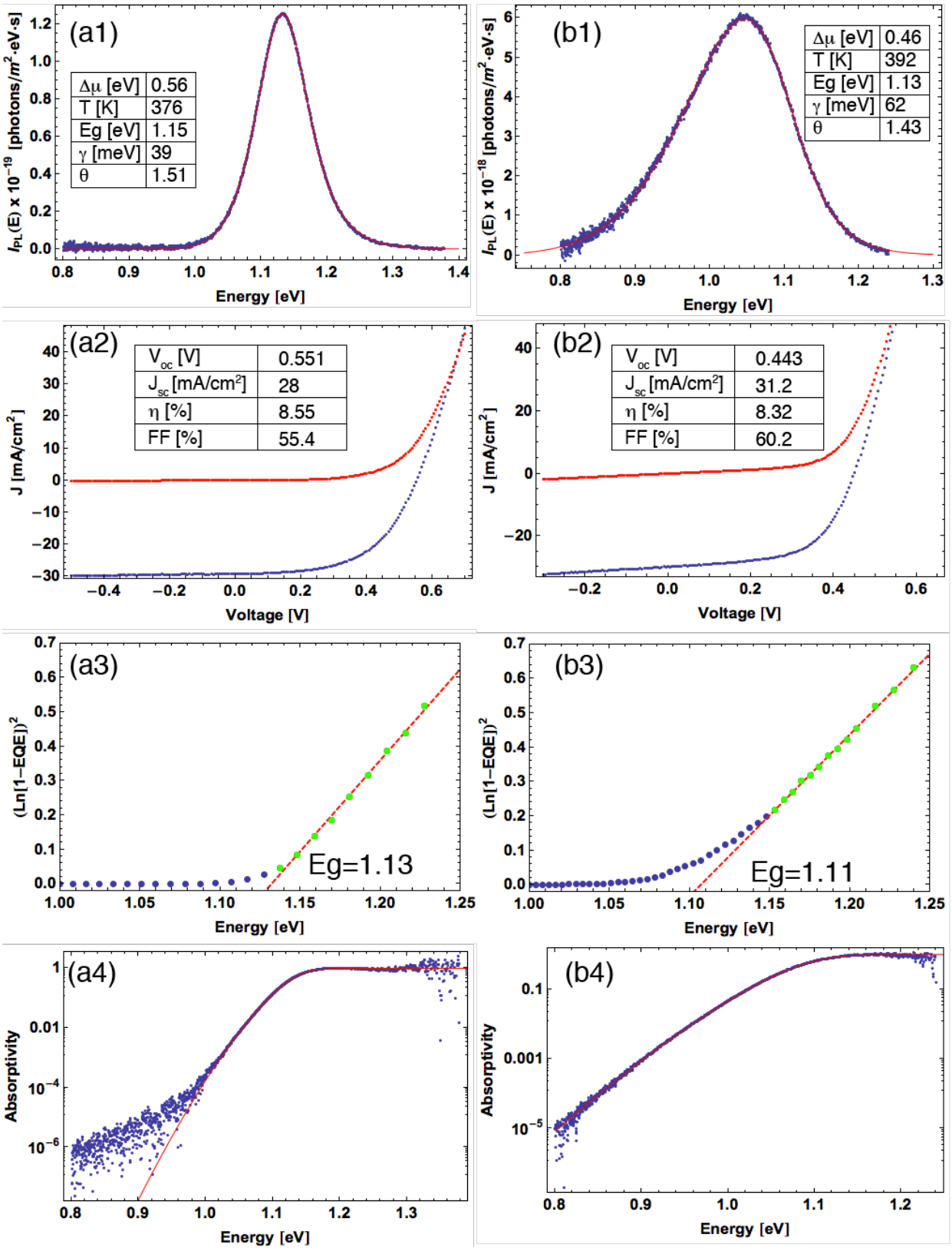

Figure 3.6. Comparison of optoelectronic characteristics of a CIGSSe nanocrystal device (panels a) and a CZTSSe molecular precursor device (panels b). Row 1 displays

the PL and full-spectrum fitting for the two devices. Blue points are the raw data (excitation ~7 suns-equivalent for CIGSSe and 18 suns-equivalent for CZTSSe) and the red curve is the fit. Row 2 contains the JV curves under dark (red curves) and AM1.5 illumination (blue curves). Row 3 is the linear extrapolation of the low energy EQE data to extract bandgap. The green points indicate the region over which the fitting occurs. Row 4 is the absorptivity extracted in the same manner as for GaAs in the previous figure. The average sub bandgap absorptivity is 1.89×10^{-2} for CIGSSe and 4.55×10^{-2} for CZTSSe

As was the case for GaAs, the model generates remarkably good fits to the experimental PL data for both the CIGSSe and CZTSSe devices. In addition, the quasi-Fermi level splitting values extracted from the fit track well with the open circuit voltages collected from J-V measurements (Figure 3.6a2 and b2). Note that the temperatures for CIGSSe and CZTSSe are slightly higher than that extracted for GaAs. This result may be due to the higher bandgap of GaAs and correspondingly lower fraction of excitation energy left for thermalization. Another explanation would be enhanced transport properties of the GaAs wafer compared to the CIGSSe and CZTSSe films, allowing for better thermal diffusion.

In addition to the parameters that were accessible through other fitting methods, the proposed model provides additional optical information on the materials. The bandgaps from the fit are commensurate with those extracted from EQE data. Note that the values from the PL fit are slightly higher than those from EQE (still within kT). There can be some ambiguity as to the E_g extracted from EQE based off the choice of fitting region. The exponents for these two samples are higher than that for GaAs and are close to the $\theta \sim 1.5$ limiting case, as opposed to the $\theta = 1$ and 2 models chosen by previous authors for these classes of materials. Additional CZTSSe samples studied in this manner have produced exponents close to 1.25 as well, which suggests that tunneling-enhanced recombination from potential fluctuations contributes to the sub-bandgap

absorption. Precise attribution of the mechanism behind such absorption behavior would require additional characterization.

The largest magnitude of tail-state absorption (reflected in the $\bar{a}_{SB}$) is found in CZTSSe, while the smallest is found in GaAs. This trend mirrors the increase in PL peak redshift from bandgap and the increasing peak FWHM from GaAs to CIGSSe to CZTSSe. Recent studies have used NMR and Raman spectroscopy to probe the Cu/Zn cation disorder in kesterite materials,[76,77] and it is possible that this disorder is responsible for the large $\bar{a}_{SB}$ in the CZTSSe sample examined here. These data demonstrate that tail states play an important role in the optical properties of kesterite materials and may be a reason why the V_{oc} deficit for CZTSSe devices is much larger than that for CIGSSe devices.[52]

3.6.2 *Comparison of Full-Spectrum Fitting to Fitting only the High-Energy Tail or Low-Energy Tail*

Fitting only the high-energy tail of AIPL data has been used by several authors to extract the local temperature and $\Delta\mu$.[68,69] However, our model combined with full-spectrum fitting is much more robust for materials with significant redshifting of the PL peak, as in the case of heavily doped or compensated materials with strong potential fluctuations. A comparison of the full-spectrum fit and the high–energy-tail-only fit of the CIGSSe sample is shown in Figure 3.7.

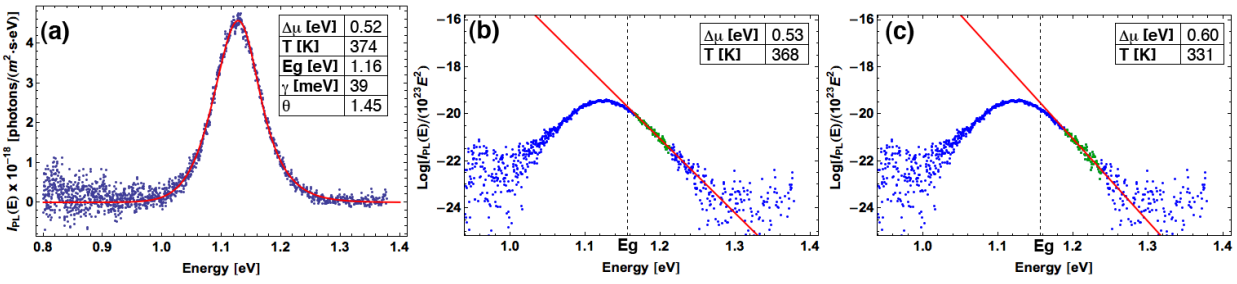

Figure 3.7. (a) Full-spectrum fitting of AIPL from CIGSe device using eq. 3.27. (b) High-energy tail only fitting (red line) over the region 1.17 to 1.21 eV (green points)

using eq. 3.28 and assuming that a=1 above bandgap. (c) High-energy tail only fitting (red line) over the region 1.19 to 1.24 eV (green points) using eq. 3.28 and assuming that a=1 above bandgap.

The full-spectrum fit provides a good match to the data, and the extracted Δμ is close to the V_{OC}. Panels (b) and (c) present the high-energy tail fit over two different regions offset by 20 meV. Note the limited region over which data may be fitted due to the scatter at very high energies and the requirement that the data be above bandgap. For the tail-only fit, there is a 10% deviation in the extracted Δμ based on the choice of the fitting region, which is unacceptable considering that V_{OC} is one of the main parameters limiting device performance in many current thin-film PV.

In addition, several authors have fit solely the low-energy tail of PL data to extract information about hypothesized potential fluctuations. However, there are similar ambiguities in fitting only the low-energy tail. In Figure 3.8, two different regions in the low energy tail of the PL from the CZTSSe device have been fit to the Gaussian potential fluctuations model.

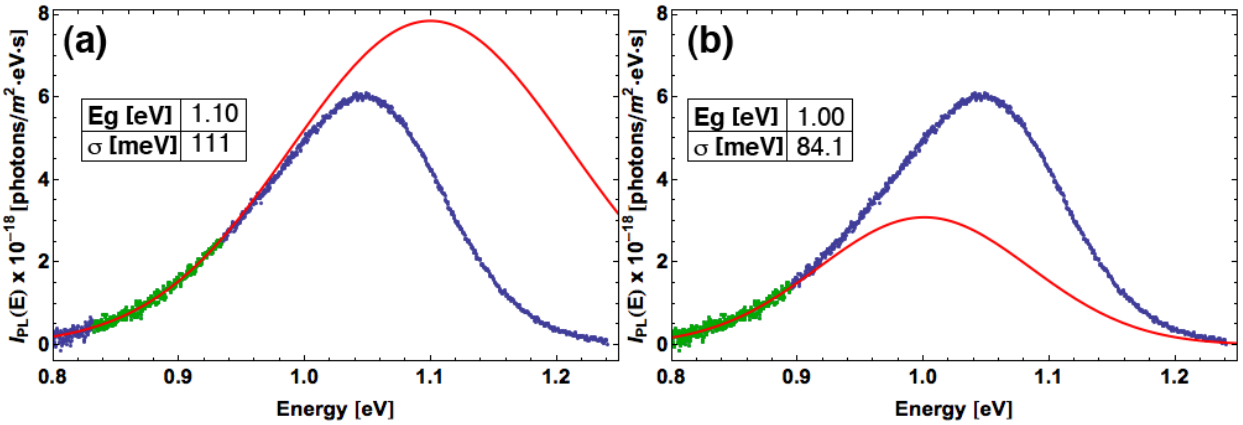

Figure 3.8. (a) Low-energy tail fitting (red curve) of CZTSSe PL over the region 0.83 to 0.93eV (green points). (b) Low-energy tail fitting (red curve) over the region 0.8 to 0.89eV (green points).

The same measured PL data are used for both fits, and both fitting regions consist of 400 data points spreading over ~ 0.1eV. As can be seen from Figure 3.8, both regions produce good fits to

the data. However, the fitted parameters vary considerably depending on the choice of the fitting range. This ambiguity in appropriate fitting region combined with the multitude of tail models available emphasizes the utility of the unified absorption model and the full-spectrum fitting presented in this chapter.

3.7 CONCLUSIONS

In conclusion, a unified model of sub-bandgap absorption has been developed and applied to the fitting of room temperature PL data from GaAs, CIGSSe, and CZTSSe. This full fit of the PL spectrum is a powerful technique that yields $\Delta\mu$, E_g, and functional form and magnitude of the sub-bandgap absorption. This fitting protocol overcomes limitations imposed by the severely redshifted peaks of highly disordered systems and the influence of fitting region that have plagued previous methods. It has been shown that GaAs experiences the least amount of band tailing while CZTSSe possesses the largest.

This technique has been used to great effect by Dr. Andrew Collord to probe the influence of stoichiometry on the optoelectronic quality of CZTSSe spray gradients.[78,79] He has analyzed tens of thousands of discrete compositions using this PL analysis in a fraction of the time that it would take to fabricate full devices and measure JV of all these formulations. The PL analysis is still computationally intensive, and fitting a single spectrum can take 30 s or longer depending on the processing power of the computer. This computation time adds up when analyzing thousands of spectra. A faster PL analysis technique to extract $\Delta\mu$ was developed as well and will be discussed in Chapter 5.

Now that we have established the power of our unified model for absorption, we will return to the detailed balance calculations and investigate the thermodynamic losses attributable to band tails.

Chapter 4. A DE*TAILED* BALANCE

4.1 INTRODUCTION

As noted in Chapter 2, the original SQ detailed balance calculations are predicated on a few key assumptions that tend to break down in real materials. One non-ideality that leads to losses in voltage and efficiency for disordered materials is sub-bandgap absorption and emission.[80] Kirchartz and coworkers accounted for the effect of non-step absorption on voltage through the use of reciprocity relations between electroluminescence and quantum efficiency experiments.[81] This approach has been used to evaluate the radiative-limited V_{OC} for silicon and CIGSSe as well as for organic solar cells and hybrid perovskites.[82]

Other groups have modeled the impact of band tails on device performance through calculations with simple exponential (Urbach) tails and Gaussian bandgap fluctuations. Tiedje showed that recombination between localized states in Urbach tails reduces the achievable V_{OC} in a-Si by 350 mV from the SQ limit.[83] Ding et al. applied a semi-analytical approach to device modeling.[84] They incorporated nonradiative recombination pathways, photon recycling, and sub-bandgap absorption and emission through Urbach tails. The magnitude of the tail width changed the effective bandgap of the absorber and resulted in improved photocurrents but diminished V_{OC} and efficiency. The band tailing made emission more likely, which increased dark current to the detriment of the V_{OC}.

Here we apply the general model of sub-bandgap absorption established in the previous chapter to a detailed balance on solar cell performance and highlight the fundamental voltage and efficiency losses caused by band tails. In addition, we demonstrate that not all tail states are created equal with regards to their detrimental impact on V_{OC} and efficiency, as tails that decay

more slowly into the gap (Urbach) result in greater losses than tails that decay rapidly for equivalent fractions of sub-bandgap absorption (Gaussian). Furthermore, we use experimentally obtained data for sub-bandgap absorption in CZTSSe devices to compare the tail-modified detailed balance with actual device performance. For the magnitude of sub-bandgap absorption found in these materials, tail states are found to drop the upper-limit efficiency by only a few percent absolute, which suggests that the main limitation for voltage and efficiency in many technologies remains the presence of non-radiative recombination centers.

4.2 Experimental Section

Here we will build off the original framework for the SQ limit that was established in Chapter 2. To account for the new losses due to sub-bandgap absorption and emission, we replaced the unit step absorptivity with our unified model of absorption that was presented in Chapter 3. We plugged the spectral absorptivity obtained using eq. 3.12 and the general tail model from eq. 3.10 into the expression for photocurrent (eq. 2.2) and reverse saturation current.

Current voltage curves were then generated for different values of bandgap, $\bar{a}_{SB}$, and exponent, and the device parameters V_{OC}, J_{ph}, FF, and PCE were extracted. All calculations used a temperature of 300 K and an $\alpha_0 d$ product of 20. Any increases in that product will result in larger $\bar{a}_{SB}$ for equivalent choices of γ and θ.

4.3 Results and Discussion

We demonstrated in the previous chapter that CZTSSe and CIGSSe exhibit absorption tails with intermediate exponents. Tails with $\theta = 1.5$ have not previously been investigated in great depth, so extensive calculations were carried out to elucidate their effect on PCE. Calculations

were done in 0.1 eV steps for bandgap and 0.001 eV for γ, the results of which are presented in Figure 4.1.

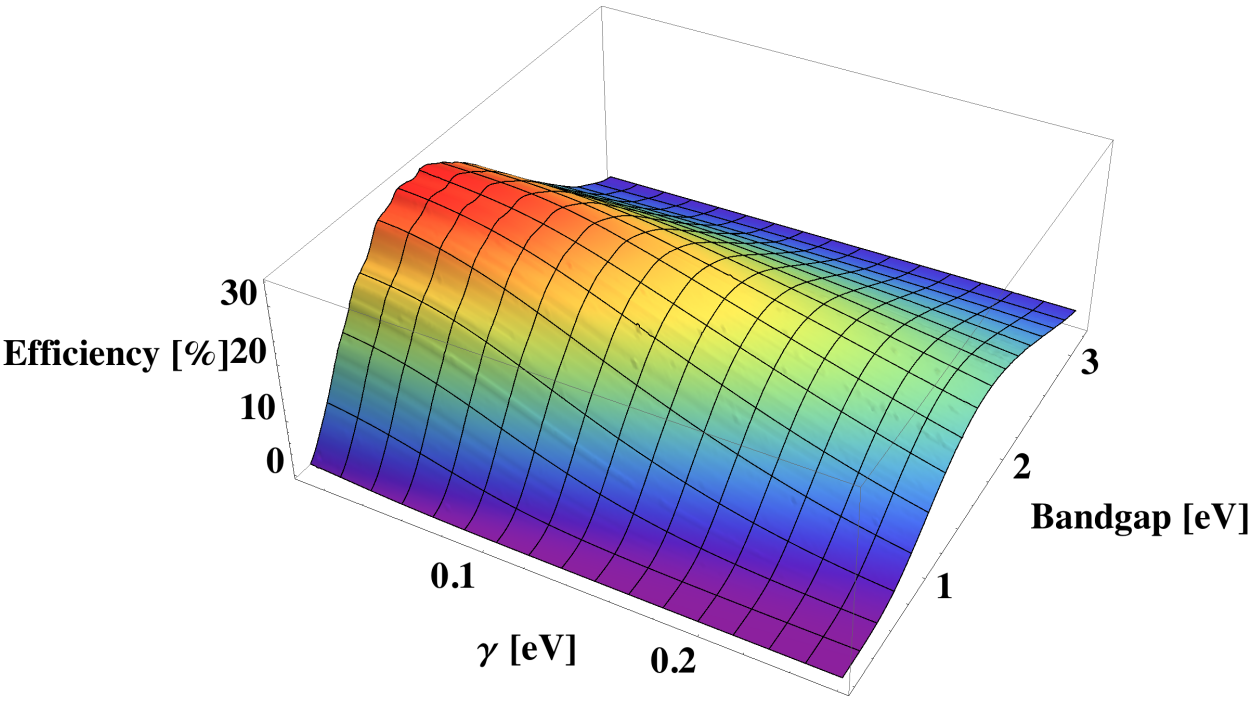

Figure 4.1. Detailed balance efficiency profile for varying bandgap and energy broadening parameter for θ = 1.5.

As expected, there is a monotonic decrease in efficiency with increasing sub-bandgap absorption for a given bandgap. Band tails also iron out the wrinkles in the efficiency vs. bandgap curves, which stem from features in the AM1.5GT spectrum. This smoothing out is accompanied by a blueshift in the optimal bandgap, and both effects are commensurate with previous studies that investigated the influence of bandgap fluctuations on efficiency.[26] For the range of γ values observed in many CZTSSe and CIGSSe devices (~30-50 meV), the radiative-limited efficiency remains close to 30% for bandgaps between 1.0 and 1.5 eV.

However, not all materials exhibit band tails with θ = 1.5. To evaluate the influence of tail functional form on the upper limits of device performance, the general model of absorption was used for detailed balance calculations for limiting cases of θ = 1.0, 1.25, 1.5, and 2.0. Values for

γ were chosen such that each exponent case had $\bar{a}_{SB} = 0.075$ at a bandgap of 1.12 eV. Efficiencies for a range of bandgaps and absorption cases are shown in Figure 4.2.

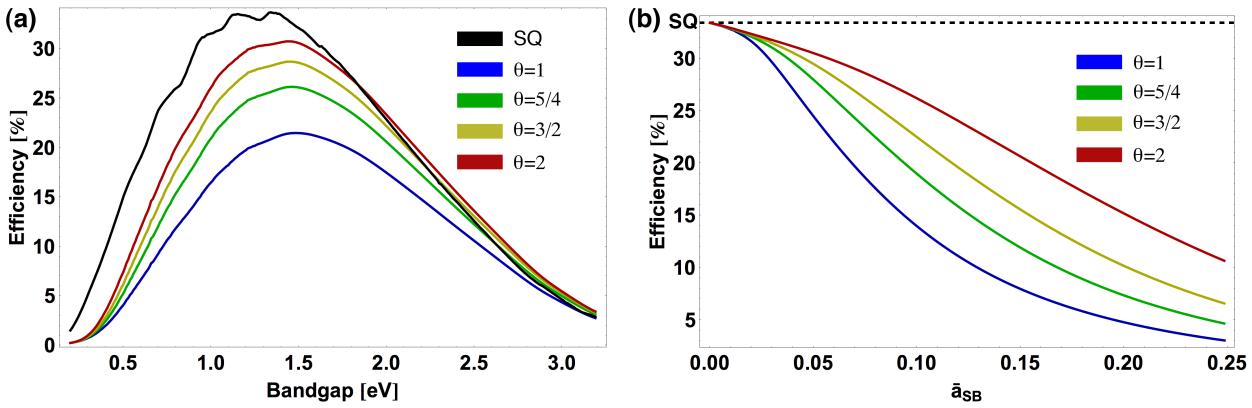

Figure 4.2**.** Effect of exponent (sub-bandgap absorption behavior) on the detailed balance limit to solar cell efficiency under AM1.5GT illumination at T = 300K. Panel (a) considers the case for equivalent average sub-bandgap absorptivity (0.075) for each exponent and demonstrates the effect of tail model on limiting efficiencies over a range of bandgaps. Panel (b) demonstrates the efficiency decrease associated for a fixed E_g = 1.12 eV with increasing levels of sub-bandgap absorption for the various tail models. The dashed line represents the SQ limit.

For fixed values of $\bar{a}_{SB}$, the absorption tail models with lower θ suffer more significant losses in overall efficiency. As the exponent approaches the Urbach case, the efficiency is lower for all bandgap values. In addition, the Urbach model experiences the most rapid decay in device efficiency with increasing sub-bandgap absorption. The exponent dictates the rate at which tailing states decay into the classically forbidden gap. Lower exponents decay more gradually and result in deeper tail states that limit efficiency. The smoothing and blue shift of the optimal bandgap occur for all absorption cases, but they are most significant for lower exponent cases. The maximum efficiency is 33.7% at E_g = 1.34 eV for the SQ case, and it drops to 30.7% at E_g = 1.43 eV for θ = 2.0 and to 21.5% at E_g = 1.48 eV for θ = 1.0. At high bandgap energies, the

efficiency from the tailing models actually improves over the original SQ limit, as the model assumes photons absorbed by states in the tail still contribute to overall photocurrent. This enhanced photocurrent overcomes the voltage penalties at larger bandgaps.

The lower efficiencies may be attributed in large part to the losses in voltage incurred by the band tails. Figure 4.3 displays the effect of band tails on V_{OC} as a function of bandgap and the magnitude of sub-bandgap absorption.

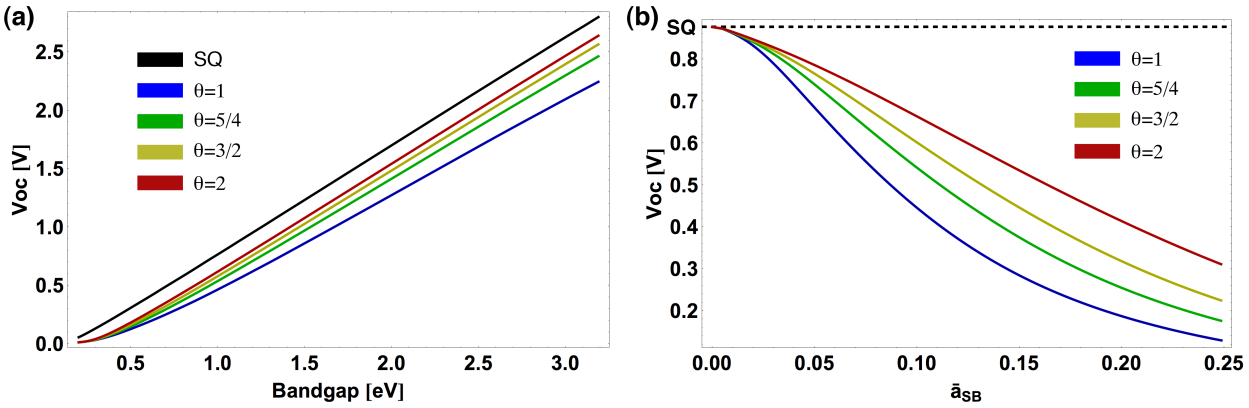

Figure 4.3. Theoretical limits for open circuit voltage for the limiting cases of sub-bandgap absorption shown in Figure 2. (a) Effect of sub-bandgap absorption model on V_{OC} for a range of bandgaps and fixed $\bar{a}_{SB} = 0.075$ and (b) for a range of $\bar{a}_{SB}$ and fixed $E_g = 1.12$ eV. The dashed line represents the V_{OC} for no tail absorption.

The V_{OC} increases with bandgap for each absorption case, but the slope of that increase drops in the presence of tails from 0.932 for the SQ model to 0.927 for $\theta = 2.0$ and 0.822 for $\theta = 1.0$. As with the efficiency degradation, voltage losses are most severe for the tails that decay more gradually into the bandgap.

Full device parameters were calculated for a device with bandgap of 1.12 eV and $\bar{a}_{SB} = 0.075$, and the results for the various tail models have been compiled in Table 4.1.

Table 4.1. Solar cell parameters calculated for limiting absorption cases and for E_g = 1.12 eV with $\bar{a}_{SB}$ = 0.075 and AM1.5GT excitation.

	γ [meV]	**η [%]**	**V_{OC} [V]**	**Jph [mA/cm^2]**	**FF [%]**
SQ	NA	33.4	0.877	438	87.0
θ=2.0	122	28.6	0.727	466	84.5
θ=1.5	100	26.2	0.685	465	82.1
θ=1.25	82.8	23.4	0.639	465	78.7
θ=1	60.3	18.6	0.556	465	71.9

The photocurrents are equivalent for all tail models because $\bar{a}_{SB}$ has been fixed (each case absorbs the same number of photons), and this photocurrent value is higher than for the SQ case. This photocurrent enhancement is overshadowed by sharp losses in V_{OC}, which in turn cause losses in FF.[85] This table highlights how deceptive it can be to use the energy broadening parameter to compare between tail models, as tails with θ = 2 require γ values double that of tails with θ = 1 to exhibit the same $\bar{a}_{SB}$.

The trend of increasing voltage penalties for decreasing exponent might at first seem counter-intuitive, as GaAs solar cells, with Urbach tails, are the best-performing single junction technology, both in terms of V_{OC} and efficiency. However, the band tails in the III-V materials are miniscule (Urbach Energies below 10 meV) and have little impact on device performance. Amorphous silicon on the other hand exhibits much larger band tails with θ = 1 character and has consequently suffered from more significant losses in voltage and efficiency.

To quantify the fundamental losses due to tails in real solar cells, we compare data from high efficiency CZTSSe devices (>11%) with current-voltage characteristics calculated for a solar cell of E_g = 1.04 eV with step absorptivity (SQ) and tailing absorptivity (de*tailed* balance, DB). The resulting curves are shown in Figure 4.4.

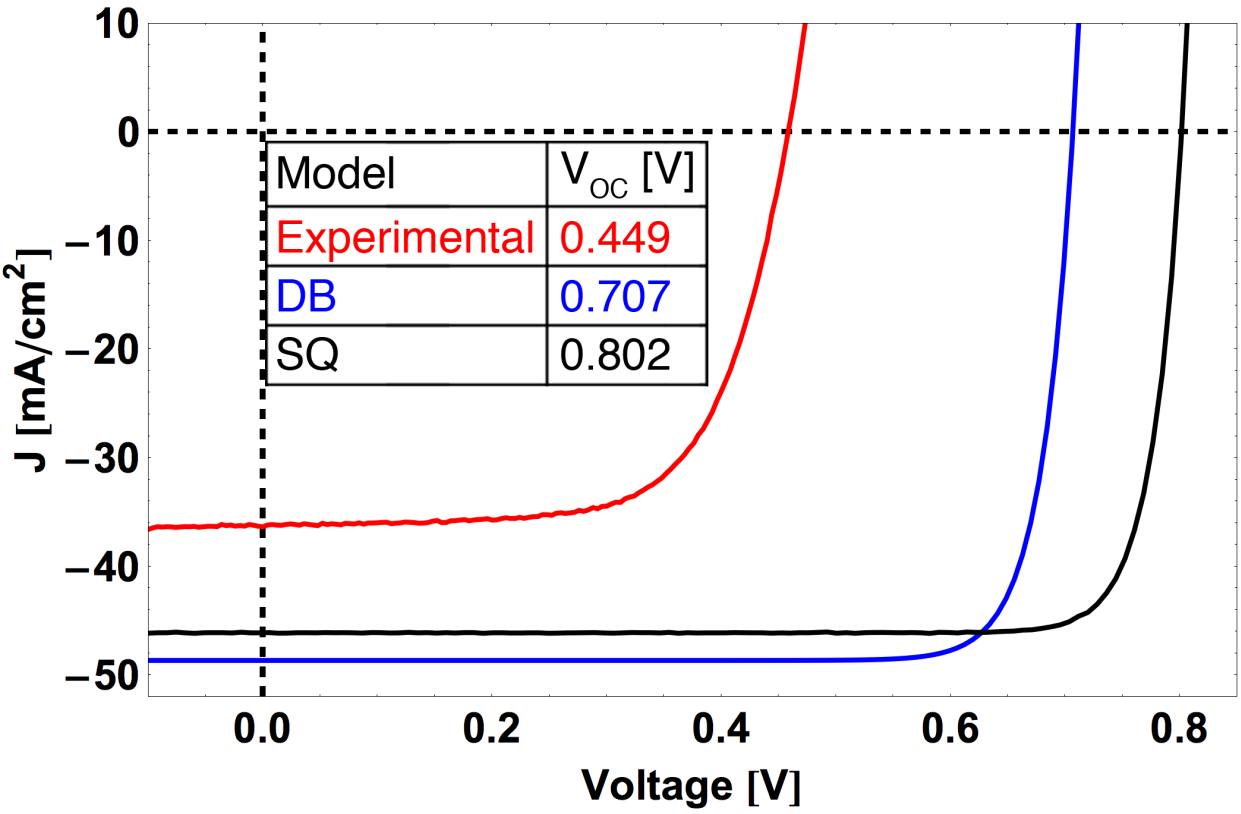

Figure 4.4. Comparison of experimental JV curve for CZTSSe device (red) with tailing de*tailed* balance (blue) and SQ limits (black).

The presence of a non-step absorptivity due to absorption tails results in a loss of 95 mV in V_{OC}, which corresponds to an efficiency drop from 31.8% to 28.9%. While the voltage loss is substantial, there are an additional 258 mV lost in the experimental V_{OC} that cannot be directly attributed to tail states. Accounting for these tail losses, the CZTSSe device still only achieves 63.5% of the de*tailed* balance V_{OC} and 40.8% of the possible PCE. This persistent deficit suggests that Shockley-Read-Hall recombination centers and/or sub-optimal device structure are the significant barriers to higher performing devices from disordered kesterites. It is also possible that tail states could enhance non-radiative recombination (much as they do for radiative recombination), which would not be accounted for in this detailed balance analysis.

4.4 CONCLUSIONS

Band tails leading to sub-bandgap absorption degrade V_{OC} and efficiency of solar cells as calculated through a detailed balance. The type of tail has a profound effect on the magnitude of losses, and tails that decay more slowly ($\theta = 1.0$) are much more detrimental to voltage than those that decay more rapidly ($\theta = 2.0$). Roughly 100mV of the V_{OC} deficit and 3% (absolute) of the efficiency loss in high performing (>11%) CZTSSe devices may be attributed to band tails. This suggests that thermal[77] and chemical processing that improves ordering in kesterites may enhance V_{OC} and PCE somewhat, but reduction of non-radiative recombination (enhancing PLQY) will be another important research thrust in CZTSSe.

Having highlighted the losses in voltage inherent to band tails, we now turn our attention to another non-ideality in real PV materials: non-radiative recombination.

Chapter 5. DETERMINATION OF MAXIMUM OPEN-CIRCUIT VOLTAGE FROM PHOTOLUMINESCENCE QUANTUM YIELD OF SEMICONDUCTORS

5.1 INTRODUCTION

As previously noted in Chapter 2, the open-circuit voltage of a solar cell is logarithmically related to the efficiency with which it emits light:

$$\frac{\Delta\mu^{max}}{q} = V_{OC}^{max} = V_{OC}^{Rad} + \frac{kT}{q}\ln(\eta_{ext}) \tag{2.6}$$

and

$$\frac{\Delta\mu}{q} = V_{OC} = V_{OC}^{SQ} + \frac{kT}{q}\ln(\eta_{ext}) \tag{2.7}$$

For the transition between eq. 2.6 and eq. 2.7, we made the simplifying assumption that V_{OC}^{Rad} could be approximated as the SQ V_{OC}. It is convenient to make this assumption for optically thick materials since V_{OC}^{SQ} is an easily calculable quantity that depends only on bandgap, ambient temperature, and the model of the solar spectrum. This type of analysis has been used to estimate the optoelectronic quality of novel Vapor-Liquid-Solid (VLS) grown InP[86] as well as mixed halide hybrid perovskites.[87] Further, the relation between V_{OC}^{SQ} and bandgap is well described by a linear relationship to bandgap over a large range (0.30 eV and 3.50 eV). By equating the flux of emitted photons to the flux of incident above bandgap photons and solving numerically for V_{OC}, the following relationship is an excellent approximation (linear with r-square > 0.99) for the case of AM1.5GT illumination with a perfect back reflector and a cell at 298.15 K:[88]

$$\frac{\Delta\mu^{SQ}}{q} = V_{OC}^{SQ} = 0.928\frac{E_g}{q} - 0.158 \tag{5.1}$$

If one does not use the simplification of eq. 2.6 to eq. 2.7, the only other option is to experimentally measure the absorption coefficient, including the range of energies below the bandgap, using a technique such as photothermal deflection spectroscopy (PDS)[89-92] or Fourier-transform photocurrent spectroscopy (FTPS),[93,94] or to extract it from absolute intensity spectrally resolved photoluminescence (PL) data[95,96] or electroluminescence (EL) data.[82,97] The downside of FTPS and EL is that they require an actual device, whereas PDS and PL may be collected from an isolated absorber layer. In addition, PDS instruments are not widespread, and thus PL becomes the most convenient tool for most to use. We also note that there is one report that suggests estimating the open-circuit voltage by starting with the bandgap (as opposed to a radiative limit) and subtracting an offset parameter (consisting of constants) and $n_l kT \ln(PLQY)$, where n_l is an empirical parameter.[98]

It is informative to consider the situations where the simplification to eq. 2.7 is inappropriate. The assumption of perfect absorption above bandgap is a justifiable approximation for the direct-gap semiconductors with high absorption coefficients that are of interest for solar cells. However, below bandgap, the absorptivity is not exactly zero. The potential trouble lies in sub-bandgap states that participate in absorption and, more importantly, emission. As discussed in Chapter 3, band tails are a ubiquitous presence in the absorption and luminescence spectra of semiconductors. Brown and coworkers noted that sub-bandgap absorption due to bandgap fluctuations would increase overall electroluminescence intensity from a device.[99] Conceptually, the effect of sub-bandgap states is easily understood by noting that (for a given $\Delta\mu$) the energy-dependent driving force for photoemission is proportional to exp(-E/kT) for luminescence at

energies E that are more than a few kT above Δμ (which is the exact range of energies for band-band PL from semiconductors). The exp(-E/kT) dependence arises from the Wien approximation form of the generalized Planck expression as shown in eq. 3.28. As a result, the lower energy sub-bandgap states preferentially emit and increase the PLQY, which leads to estimates of higher V_{OC} when one neglects the sub-bandgap states by using eq 2.7.

In this chapter, we elucidate the effect of disorder and non-ideal absorptivity on PLQY and their effects on estimation of the V_{OC}. Our results demonstrate that neither PLQY nor PL peak intensity alone are sufficient metrics for evaluating the potential of a given photovoltaic material. In addition, we present two improvements to eq. 2.7 that account for the fundamental loss due to sub-bandgap states but still allow use of V_{OC}^{SQ} and the PLQY to calculate $V_{OC.}$ These methods provide a quick and powerful contact-free tool to quantify the inherent optoelectronic quality of a material for use as a photovoltaic absorber layer. It should be noted that these techniques provide an upper-limit estimate on the attainable V_{OC} in a device, as sub-optimal device architecture (e.g. poor band alignment, Fermi-level pinning due to interface states, or enhanced non-radiative interfacial recombination) could lead to reduced voltage from the device. We also emphasize that Δμ and V_{OC} should be judged relative to the theoretical limit for the bandgap of the material rather than by their magnitude alone. A material with E_g = 1.5 eV and Δμ = 0.7 eV (57% of radiative limit) will typically be a worse photovoltaic absorber than one with E_g = 1.0 eV and Δμ = 0.6 eV (78% of radiative limit). In the latter, the losses in voltage are more than made up for by the gains in current due to the lower bandgap.

5.2 Experimental Section

In our analysis, we used the generalized model of sub-bandgap absorption from Chapter 3 to simulate luminescence spectra with varying degrees of band tailing.[96] In modeling PL spectra,

we assumed a tail character of θ = 1.5 (Franz-Keldysh model), a bandgap of 1.12 eV, a temperature of 298.15 K, and an $\alpha_0 d$ product of 20, values that are reasonable for CZTSSe molecular precursor films.[96] The energy broadening parameter, γ, was used to set the magnitude of band tails.

To test our proposed techniques, we studied the PL spectra from a III-V material with low band tailing, p-GaAs, and a polycrystalline material with large band tailing, CZTSSe.[100] Additional samples included molecular precursor CISSe and CIGSSe films as well as $CH_3NH_3PbI_3$. All measurements were done using the same experimental setup and calibration from Chapter 3.

5.3 Results and Discussion

5.3.1 *PLQY and PL Peak Intensity as Metrics for Optoelectronic Quality*

Two metrics that are commonly used to evaluate material quality are PL peak intensity and PLQY, with high values for both equating to better materials. However, these parameters can be misleading, as increasing non-ideal sub-bandgap absorption will result in increases in both absolute peak intensity and PLQY. This fact has been highlighted in Figure 5.1, where we have varied γ and Δμ to create equivalent peak intensity (a) and PLQY (b).

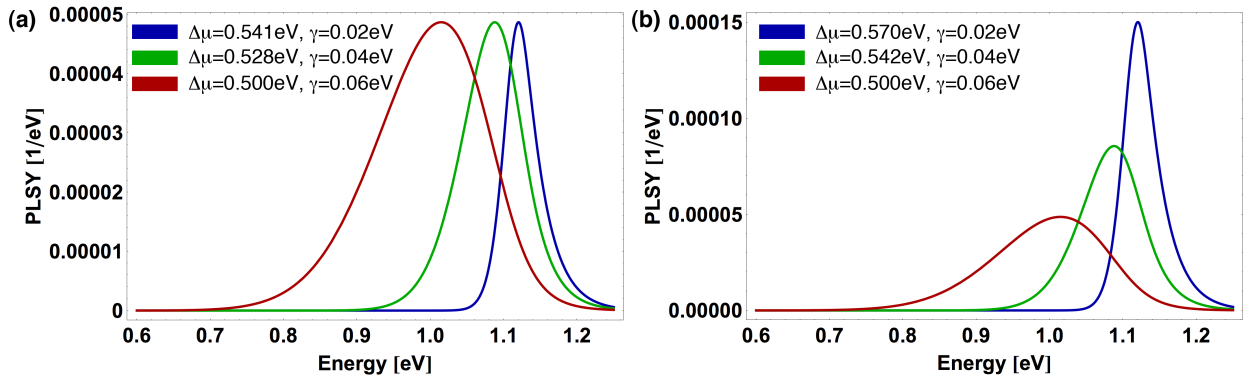

Figure 5.1. Simulated PL spectra for varying sub-bandgap absorption cases. Variation of $\Delta\mu$ values leads to either (a) common peak intensity of 4.87×10^{-5} eV^{-1} or (b) equivalent PLQY = 9.30×10^{-6}.

For the analysis, it is helpful to convert the PL spectral flux (PLSF), which has units of [photons/m^2·eV·s], to a PL spectral yield (PLSY) by dividing it by the absorbed excitation photon flux [photons/m^2·s]. PLSY has units of 1/eV, and integration of PLSY over energy yields a dimensionless number that is exactly equal to the PLQY. From Figure 5.1, it is clear that there are a multitude of $\Delta\mu$ values that are possible for a given PLQY or peak intensity (spanning tens of meV). This treatment has not even considered the potential for different tail models, which further complicates this picture. These simulations demonstrate that PLQY and peak intensity alone can be ambiguous metrics for material quality, and there is a need for deeper analysis.

One alternative is to use eq. 2.7 to extract V_{OC} from the PLQY to more reliably evaluate material quality. In order to evaluate this method, we simulated PLSY curves, calculated the PLQY, and estimated the V_{OC} under one-sun-equivalent excitation for two different cases of quasi-Fermi level splitting, each as a function of the magnitude of sub-bandgap absorption. Control over the magnitude of sub-bandgap absorption was achieved by varying the parameter γ in eq. 3.10, and PL was simulated as in Chapter 3 using $\Delta\mu$ = 0.5 eV (57% of qV_{OC}^{SQ} for E_g = 1.12 eV), parameters on the order of those for the best CZTSSe devices.[101,102] The results for these simulations are given in panels a-c of Figure 5.2. With increasing magnitude of tail states, the PL peak redshifts, broadens, and increases in intensity. The PLQY increases with larger amounts of tailing. Thus, even though the optoelectronic quality ($\Delta\mu$) is fixed, as the magnitude of tail states increases, PLQY and peak intensity vary greatly. We note that the enhancement in PLQY occurs only for materials where PLQY is less than 100%.

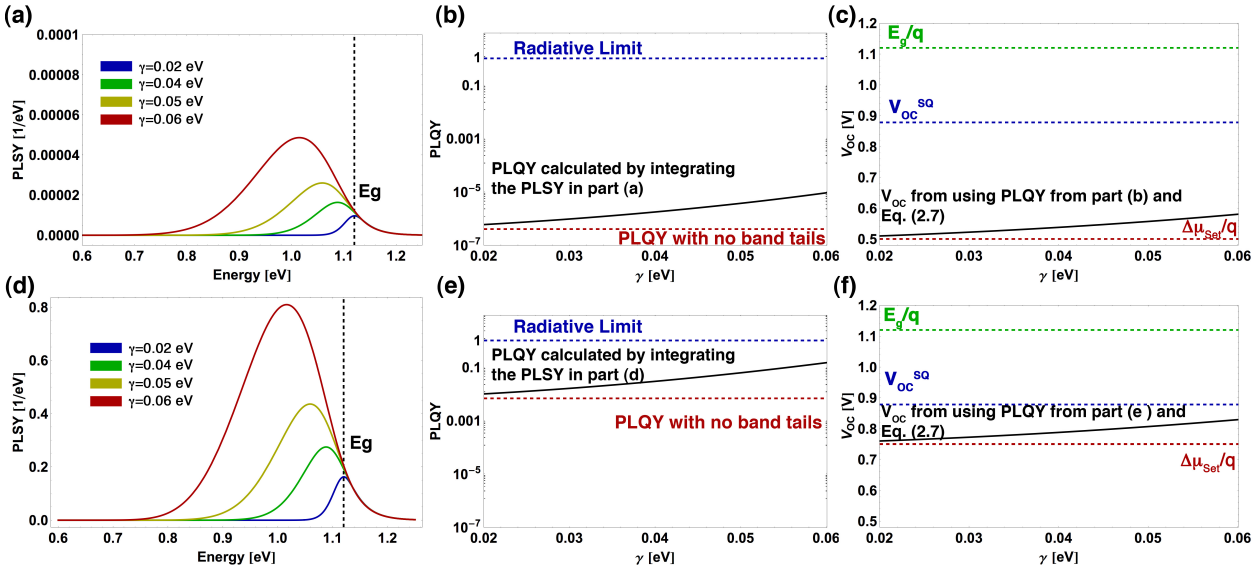

Figure 5.2. Effect of sub-bandgap absorption on (a) PL spectral yield, (b) the total PLQY, and (c) V_{OC} calculated from eq. 2.7 under the assumption of SQ absorptivity for V_{OC}^{Rad}. The PLSY curves in part (a) were simulated with $\Delta\mu = 0.5$ eV (57% of qV_{OC}^{SQ}). The PLQY in part (b) is calculated by integrating the PLSY curves in part (a). The difference between the solid black and dashed red lines in (c) reveals the error incurred by using the SQ V_{OC} simplification. Panels (d), (d), and (f) present similar calculations but for $\Delta\mu = 0.75$ eV (85% of qV_{OC}^{SQ}).

Since many new materials being screened for potential application in solar cells do not have well-known spectral absorptivity data, it is much easier to use V_{OC}^{SQ} and eq. 2.7 as opposed to V_{OC}^{Rad} and eq. 2.6. However, if experimentally measured PLQY is used with V_{OC}^{SQ} and eq. 2.7, the maximum possible open-circuit voltage can be significantly overestimated, which is shown in Figure 5.2(c). This overestimation occurs because of deviations between V_{OC}^{SQ} and V_{OC}^{Rad}, which are due to absorption (and emission) by the sub-bandgap states. Thus, it is imperative that one consider the sub-bandgap absorption when using PLQY to estimate the maximum possible V_{OC}. These trends in PLQY inflation and V_{OC} overestimation with increasing band tails are true for situations with higher optoelectronic quality (but still below the radiative limit). Simulations for $\Delta\mu = 0.75$ eV (85% of SQ limit), representative of high quality CIGSSe,[103] are included in panels (d) through (f) of Figure 5.2 to demonstrate this fact.

The absorption behavior corresponding to the PL spectra simulated in Figure 5.2a and Figure 5.2d are provided in Figure 5.3. While the band tails extend well below the bandgap, as indicated by the spectral absorptivity curves in part (a), the bandgap that would be estimated by extrapolating the linear region of a plot of either the absorbance squared, or the absorption coefficient squared (see Figure 5.3b) all yield approximately the same bandgap (depending on the region selected for extrapolation). This kind of extrapolation analysis (applied nearly ubiquitously to experimental absorbance data from direct bandgap semiconductors) relies on the fact that the joint density-of-states just above the bandgap has a square root dependence with energy for direct-transitions.

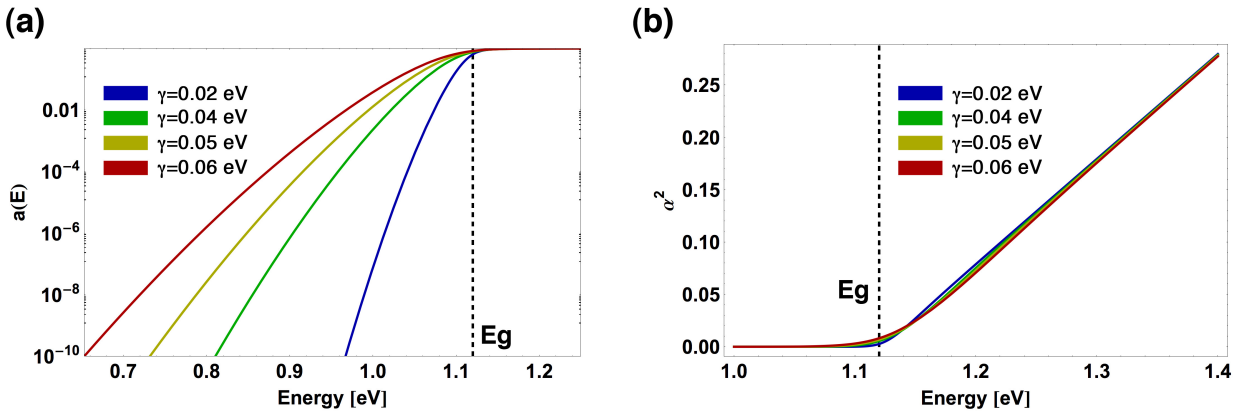

Figure 5.3. Absorptivity and absorption coefficient squared for the cases used to simulate PL spectra in Figure 5.2(a) and (d). The spectral absorptivity is presented on a semi-logarithmic plot (a), and the absorption coefficient squared is simulated for bandgap estimation in (b).

It is possible to avoid the error induced by tail states. For example, one may take advantage of the reciprocity between electroluminescence and EQE measurements.[97] By using the EQE to extract absorption information, it is possible to calculate the V_{OC} from QE_{LED}, the quantum efficiency of a solar cell operating in forward bias (as a light emitting diode). This method has been applied to CIGSSe, organic photovoltaics, and hybrid perovskite solar cells.[81,82,104,105]

However, such measurements can only be carried out on full devices, and it is desirable to have a technique that can reveal the inherent optoelectronic quality of a material without requiring the design and fabrication of a photovoltaic device (or LED). As such there is a need for an analysis method that utilizes measured PLQY from real materials and V_{OC}^{SQ} (which eliminates the need to measure the absorption coefficient significantly below bandgap) to accurately yield an upper estimate of the possible V_{OC} from a material if it were used in a solar cell. Here, we develop two methods and compare their accuracy to the known quasi-Fermi level splitting of simulated PL and to actual measured open-circuit voltages of devices fabricated from the materials. The first method uses only the above-bandgap emission to determine PLQY (excluding the sub-bandgap emission). The second method includes all the emission to calculate the PLQY but, instead of using the actual bandgap to calculate V_{OC}^{SQ}, uses the energy of the PL peak position as an effective bandgap to calculate V_{OC}^{SQ}.

5.3.2 *Above-Bandgap QY Method*

The energy dependence of the high-energy tail of a band-band photoluminescence peak is dominated by the Bose-Einstein term in eq. 3.27, and the intensity is set by $\Delta\mu$ (for a fixed T). In direct-gap semiconductors of interest for photovoltaics, the absorption coefficient increases rapidly above bandgap, and for material thicknesses on the order of a micron, nearly all photons with energy greater than the bandgap are absorbed. Thus, above bandgap the absorptivity approaches one quickly with increasing energy. If the absorptivity above bandgap is near unity, then to good approximation, the photoluminescence that occurs only above the bandgap will be equal to the photoluminescence for the ideal SQ case, which assumes the absorptivity is a step function equaling 1 above bandgap. Thus, by discarding the below-bandgap photoluminescence from the PLQY, one may obtain a much better estimate of the V_{OC}:

$$V_{OC}^{Eg+} = V_{OC}^{SQ} + \frac{kT}{q}\ln\left(\eta_{ext,E>E_G}\right) \tag{5.2}$$

where

$$\eta_{ext,E>Eg} = \frac{\int_{Eg}^{\infty} I_{PL}(E)dE}{\text{Absorbed Photon Flux}} \tag{5.3}$$

This approximation will result in a slight underestimation of V_{OC} due to imperfect absorption above bandgap, but it amounts to errors of only a few mV in the majority of cases. Most experimental setups do not measure the above-bandgap PLQY; rather they measure the QY over the entire spectrum. We make use of logarithm rules to express the V_{OC} in terms of the measureable full-spectrum PLQY and a correction term for the fraction of above-bandgap luminescence, ϕ:

$$\frac{\Delta\mu}{q} = V_{OC} = V_{OC}^{SQ,Eg} + \frac{kT}{q}\ln\eta_{ext} + \frac{kT}{q}\ln\phi \tag{5.4}$$

ϕ may be estimated graphically from the measured PL spectrum or may be calculated precisely by:

$$\phi = \frac{\int_{E_g}^{\infty} I_{PL}(E)dE}{\int_{0}^{\infty} I_{PL}(E)dE} \tag{5.5}$$

5.3.3 *Effective Bandgap Method*

In many situations, one may not even know the bandgap, or not know the bandgap at one-sun excitation conditions. For instance, in many high-bandgap perovskites, light alters the structure of the material, and the bandgap may experimentally change with time and light intensity.[106,107] As seen above, the presence of tail states shifts the PL peak position to lower energy and sacrifices quasi-Fermi level splitting. This can be accounted for by using the PL peak position as an effective bandgap for calculating the SQ V_{OC}:

$$\frac{\Delta\mu}{q} = V_{OC} = V_{OC}^{SQ,Epk} + \frac{kT}{q}\ln \eta_{ext} \tag{5.6}$$

In order to test both of these methods in comparison to eq. 2.7, we simulated PL spectra while setting $\Delta\mu$ = 0.5 eV and used eq. 5.4 and eq. 5.6 to estimate V_{OC} from PLQY using our two methods. Table 5.1 compiles the results from using these equations to calculate the $\Delta\mu$ from the simulated spectra.

Table 5.1. Comparison of the standard method and our two new methods to determine quasi-Fermi level splitting from simulated PL. The last three columns are the calculated quasi-Fermi level splitting ($\Delta\mu$) using eq. 2.7, using eq. 5.4, and using eq. 5.6, respectively, on PL spectra simulated using a given and known $\Delta\mu$ (shown in the second column) for several different tail state models (shown in the first column). The simulations used E_g = 1.0 eV, T = 298.15 K, and one-Sun illumination. Note that for a 1.0 eV bandgap semiconductor, one-Sun is an incident flux of above bandgap photons of about 3 x 10^{21} photons/(s·m^2)

Sub-bandgap absorption parameters	$\Delta\mu$ Input [eV]	$\Delta\mu$ from PLQY and $V_{OC}^{SQ,Eg}$ (Eq. 2.7)	$\Delta\mu$ from above-E_g PLQY and $V_{OC}^{SQ,Eg}$ (Eq. 5.4)	$\Delta\mu$ from PLQY and $V_{OC}^{SQ,Epk}$ (Eq. 5.6)
θ=1.0; γ=10meV	0.5	0.507	0.497	0.511
θ=1.0; γ=20meV	0.5	0.536	0.497	0.522
θ=1.5; γ=20meV	0.5	0.510	0.497	0.511
θ=1.5; γ=60meV	0.5	0.580	0.498	0.484
θ=2.0; γ=40meV	0.5	0.525	0.497	0.508

θ=2.0; γ=120meV	0.5	0.649	0.499	0.441

For all cases, the best agreement between the input Δμ and the Δμ calculated from PLQY occurred for the above-bandgap PLQY method, for which deviations from the input value were less than 1%. The E_{PK} method generally improves agreement compared to eq. 2.7, but may underestimate V_{OC} for materials with very large sub-bandgap tails, which exhibit the largest redshift of E_{PK} from E_g. However, the additional benefit of the E_{PK} method is that one does need to separately measure the bandgap (which can be difficult for materials that change under illumination, like some hybrid perovskites). To generalize the range of validity of these methods, we compare the V_{OC} extracted from these methods at varying levels of disorder, as indicated by the full-width-at-half maximum (FWHM) of the PL peaks. The results for the limiting case of Urbach and Thomas-Fermi tails are summarized in Figure 5.4.

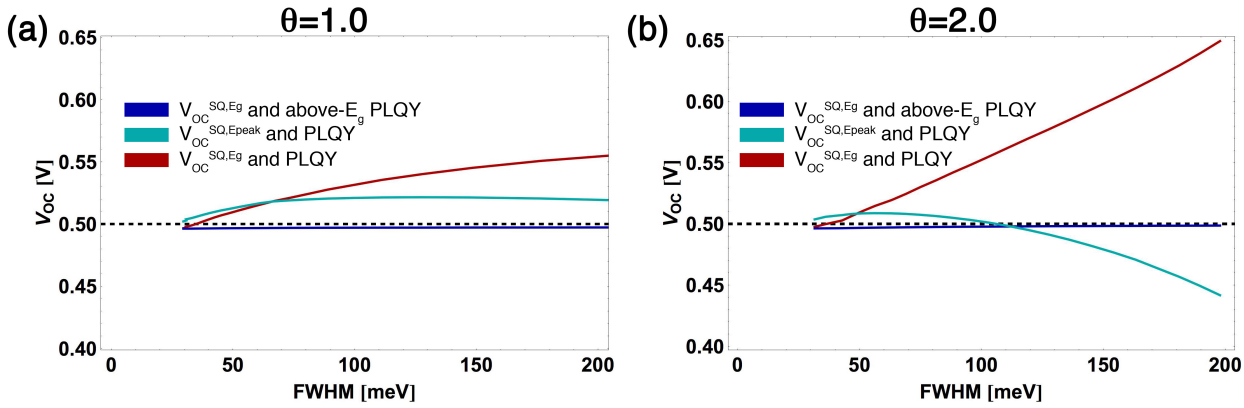

Figure 5.4. Comparison of V_{OC} estimation techniques for band tails with simple exponential (a) and Gaussian (b) character. Dashed line represents the input $\Delta\mu_{Set}/q$ used in peak simulations. Note the outstanding agreement between the above-bandgap QY method (blue curve) and the input Δμ.

The above-bandgap QY method works very well for all levels of disorder and tail cases. The E_{PK} method slightly overestimates the V_{OC} for cases with minor sub-bandgap tails, but the error is reduced from the value calculated through eq. 2.7. For large tails, the E_{PK} method underestimates the V_{OC} due to the severe redshift of the PL with strong band tails. The utility of

Figure 5.4 is that one can easily determine the appropriate method (i.e., evaluate if eq. 5.6 is applicable) by examining the FWHM of the experimental PL peak. Since most good PV materials have FWHM less than 150 meV, eq. 5.6 works well for a large range of materials.

5.3.4 *Application to PL from PV Absorber Layers*

We examined how these models worked for experimentally measured PL data from real materials and how the estimated V_{OC} compared with actual V_{OC} measured from current-voltage (JV) measurements on finished devices or the $\Delta\mu$ from a full-spectrum PL fit.[96] We studied the PL spectra from a III-V material with low band tailing, p-GaAs, as well as solution-processed polycrystalline materials with larger band tailing like CZTSSe,[100] CIGSSe,[108] and $CH_3NH_3PbI_3$.[109,110]

Using a fit of the spectrally resolved PL, we extracted absorptivities from the experimental photoluminescence curves. Sample photoluminescence curves are shown in Figure 5.5 (left-hand axis) for GaAs and CZTSSe. We also extracted the spectral absorptivity from the PL data and compare it with the SQ absorptivity model (Figure 5.5 right-hand axis) for GaAs and CZTSSe.

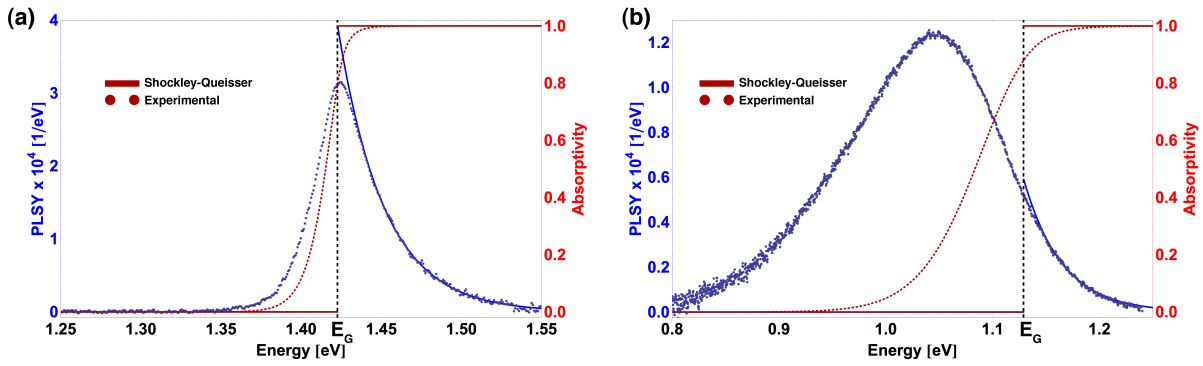

Figure 5.5. Comparison of experimental and ideal SQ-modeled luminescence (blue) and absorptivity (red) for (a) GaAs and (b) CZTSSe. Solid lines represent the ideal step absorptivity and PL assumed in the SQ model, while the dotted curves are for the experimental PL and tail-model derived absorption.

It is clear that even in the case of a near ideal semiconductor (GaAs), there is sub-bandgap emission that slightly increases the PLQY compared to the step absorptivity case. For the disordered kesterite CZTSSe, more than 90% of the PL is emitted below bandgap and results in significant deviations from the step absorptivity used in SQ calculations. The PL and JV curves for the CISSe, CIGSSe, and $CH_3NH_3PbI_3$ samples are provided in Figure 5.6.

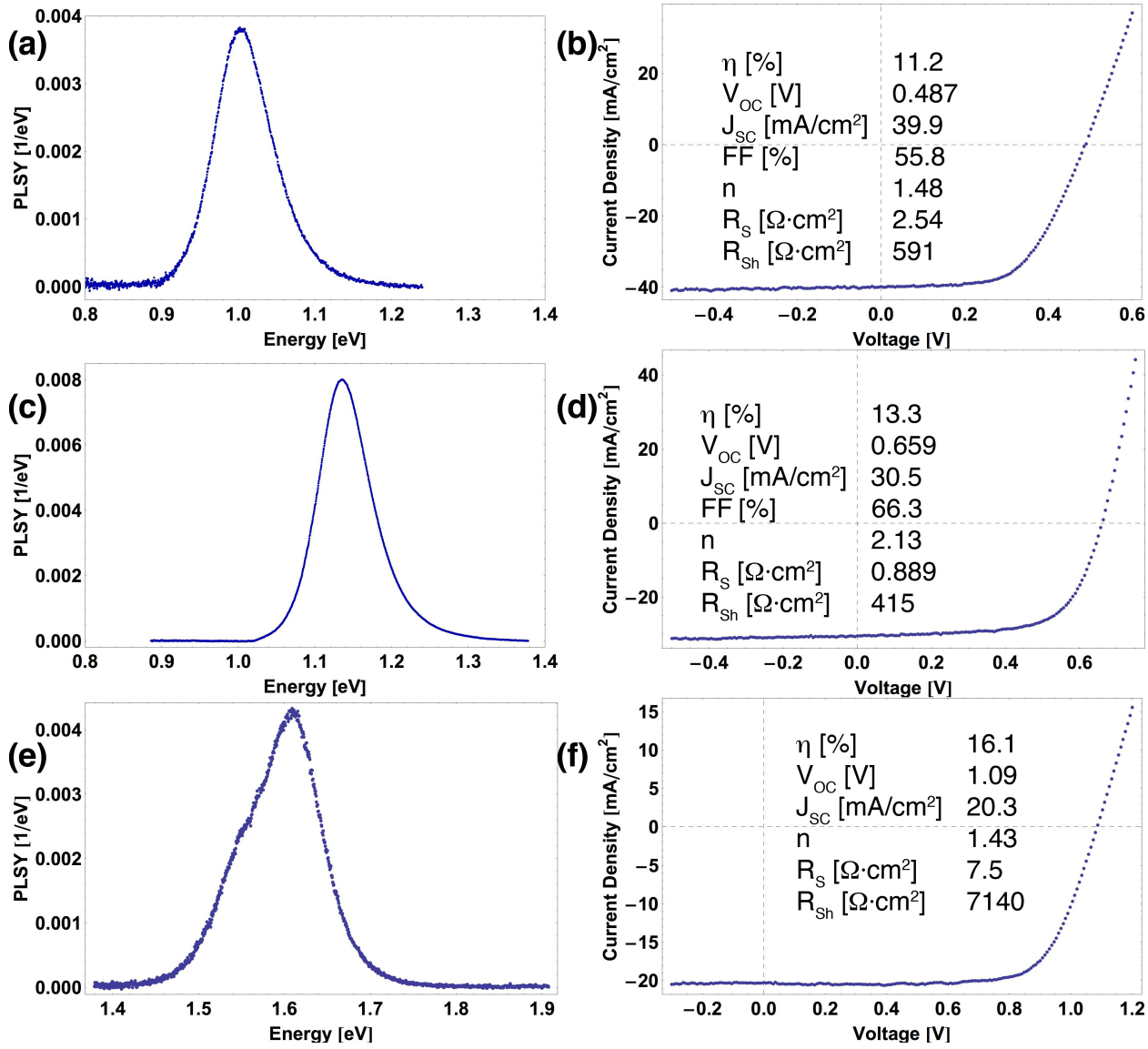

Figure 5.6. PLSY spectra for CISSe (a), CIGSSe (c), and $CH_3NH_3PbI_3$ (e). JV curves for CISSe (b), CIGSSe (d), and $CH_3NH_3PbI_3$ (f).

The estimates of Δμ from the different PLQY methods as well as the V_{OC} from JV measurements for the various materials are presented in Table 5.2.

Table 5.2. PLQY and estimated Δμ under different absorption assumptions for GaAs, CZTSSe, CISSe, CIGSSe, and $CH_3NH_3PbI_3$.

	Δμ from PL fit [eV]	**Measured PLQY**	**ϕ**	**Δμ from eq. 2.7 [eV]**	**Δμ from eq. 5.4 [eV]**	**Δμ from eq. 5.6 [eV]**	**V_{OC} [V]**	**PCE [%]**
GaAs	0.893	1.70×10^{-5}	0.643	0.903	0.890	0.897	—	—
CZTSSe	0.458	2.34×10^{-5}	0.0867	0.538	0.455	0.463	0.443	8.32
CISSe	0.487	3.78×10^{-4}	0.380	0.517	0.484	0.500	0.487	11.2
CIGSSe	0.664	7.36×10^{-4}	0.540	0.676	0.657	0.675	0.659	13.3
$CH_3NH_3PbI_3$	1.12[c]	4.88×10^{-4}	0.481	1.12	1.10	1.10	1.09	16.1

In all samples studied here, the measured PLQY is higher than that for the comparable SQ case. The qV_{OC} calculated from eq. 2.7 (assuming SQ absorptivity) and the qV_{OC} from eq. 5.4 (considering only above-bandgap QY) are compared to the V_{OC} from JV measurements under simulated AM1.5GT conditions. Note that the temperatures used in eq. 2.7 and 5.4 were above room temperature to account for sample heating during excitation. As noted above, the assumption of the SQ-limited radiative V_{OC} results in overestimation of the potential in all materials. This overestimation is only 10 meV in GaAs; however, in CZTSSe the overestimation reaches 80meV. Errors of this magnitude are problematic, as the voltage deficit is of particular concern in many solar cell technologies. After application of eq. 5.4, the accuracy of the qV_{OC} estimation is much improved, and we predict voltages within 1% of actual Δμ values. The E_{PK} method only slightly overestimates V_{OC} in each case (since the tails are not as large as the cases examined in Table 1), and is an improvement over eq. 2.7. Both methods work remarkably well for this diverse set of technologies. This proves that the approaches we present are robust to changes in band tail magnitude and shape, and even the presence of shoulders or non-ideal

[c] Note that the quasi-Fermi level splitting for the $CH_3NH_3PbI_3$ sample was estimated from a linear fit to the high-energy tail of the PL. There was a PL shoulder at low energies, precluding a full-spectrum fi.

emission peak shapes (the particular perovskite sample used in this study has a strong low-energy shoulder, as shown in Figure 5.6e).

For some samples, PL was collected with higher than one sun injection for signal-to-noise reasons. The increase in voltage due to higher injection conditions can be well modeled with an additional term with logarithmic dependence on the concentration factor, CF (Figure 5.7):

$$\Delta V_{OC} = \frac{kT}{q} \ln(CF) \tag{5.7}$$

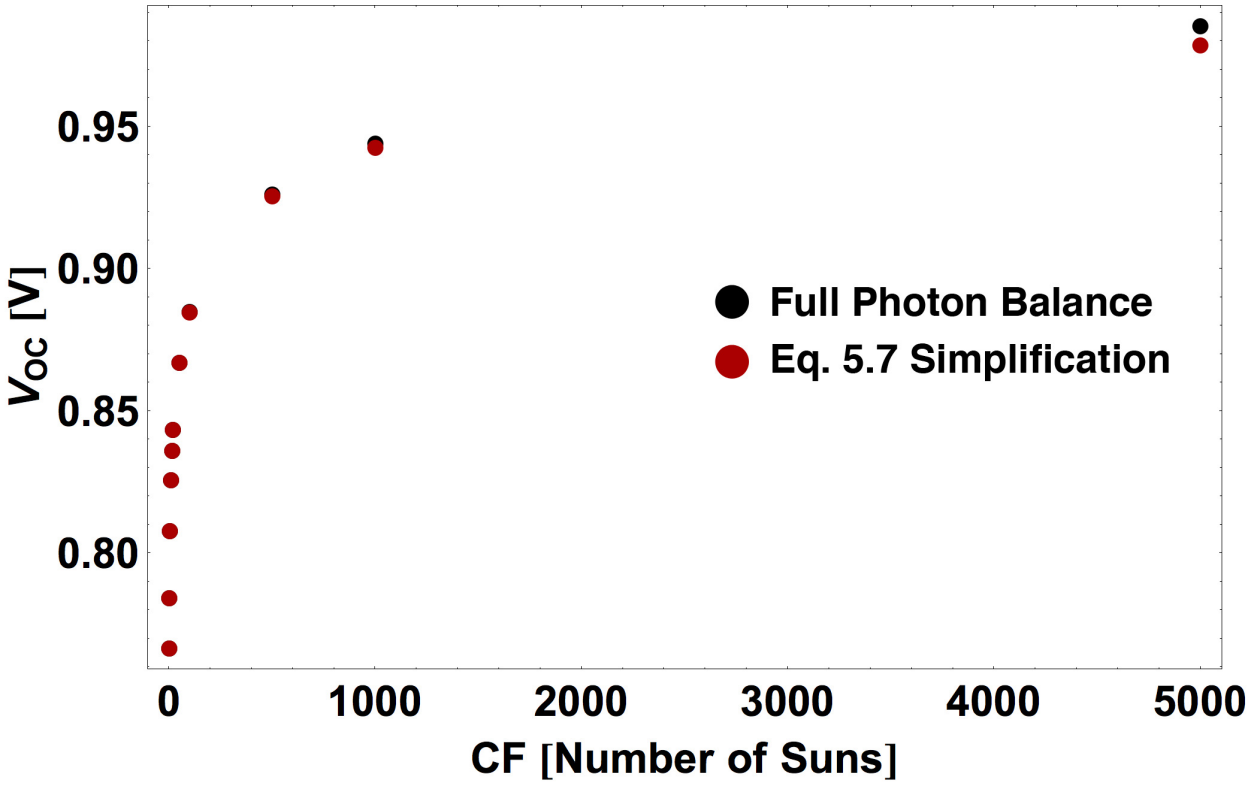

Figure 5.7. Effect of higher injection conditions on the SQ limit. The black points are calculations from the full photon balance, and the red points are from the simplification in eq. 5.7.

Higher injection conditions may result in increased temperature, and the effect of temperature on the detailed balance limits of V_{OC} are presented in Figure 5.8 and Figure 5.9.

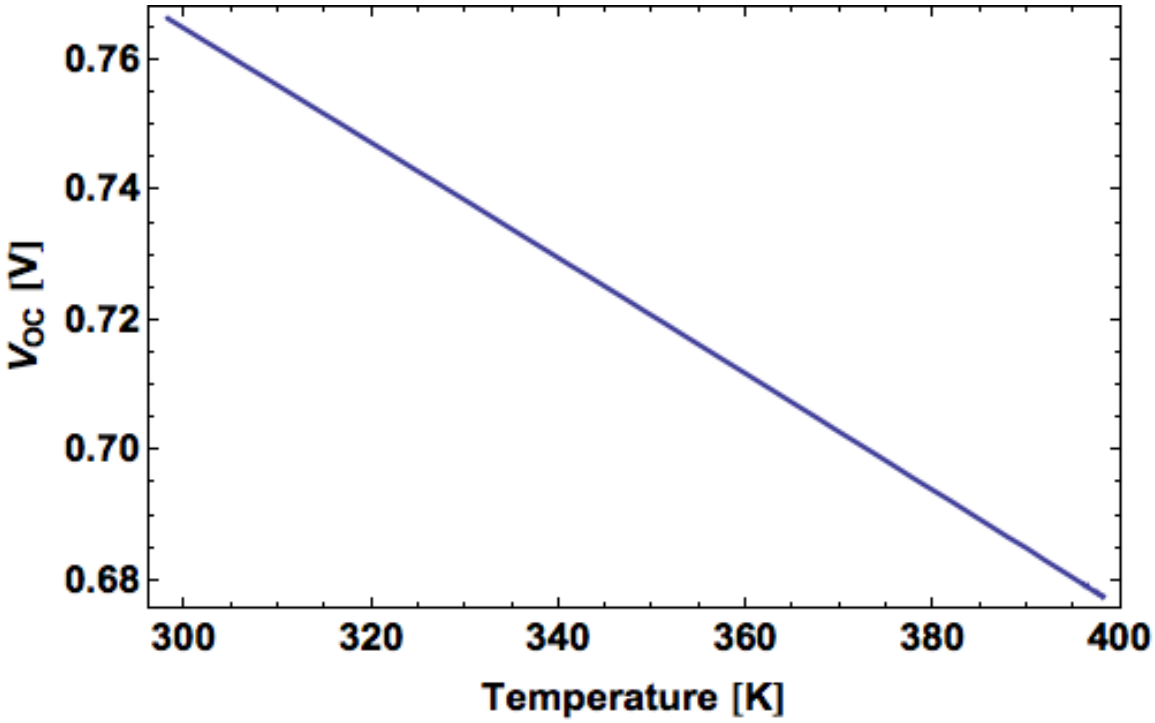

Figure 5.8. Effect of temperature on V_{OC} in the SQ limit for E_g = 1.0 eV and AM1.5GT excitation conditions.

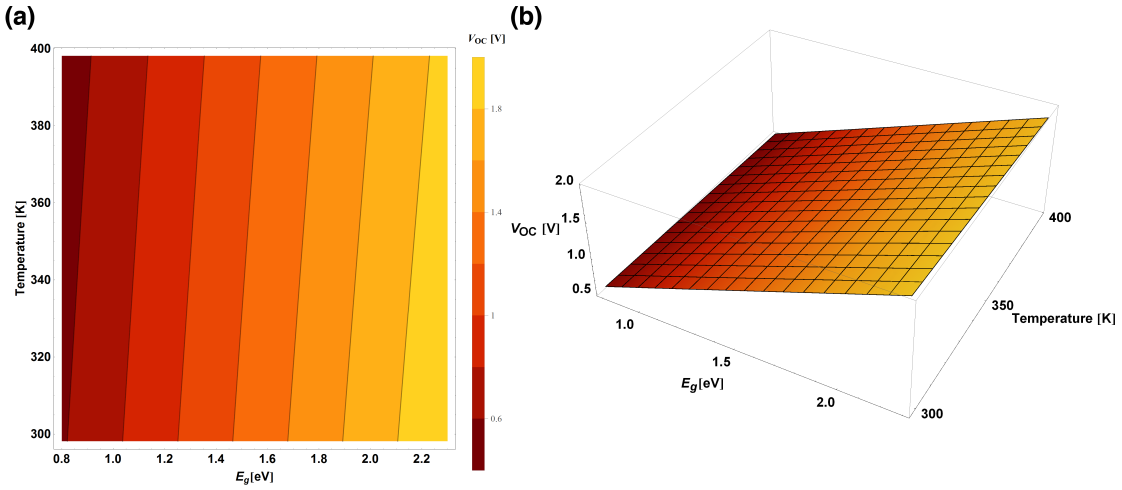

Figure 5.9. Detailed balance calculations of the SQ V_{OC} as a function of bandgap and temperature presented in (a) contour plot and (b) 3D plot.

A fit to the data in Figure 5.9 results in the following regression ($R^2 > 0.99999$):

$$V_{OC}=0.1496+0.9235\frac{E_g}{q}-0.0010T \quad (5.8)$$

A summary of the injection conditions and temperatures extracted from a fit to the PL spectra are given in Table 5.3. We note that it is possible to cool samples and reduce the effect of radiative heating through the use of a temperature-cooled stage or forced convection over the top of the sample. Substrate cooling would then allow the use of ambient temperature in all calculations.

Table 5.3. Sample temperature from PL fit and corresponding injection level conditions

	Injection Level [# of Suns]	**Temperature from PL Fit [K]**
GaAs	12.8	321
CZTSSe	18.0	392
CISSe	11.8	394
CIGSSe	13.1	373
$CH_3NH_3PbI_3$	1.0	305

5.4 CONCLUSIONS

In conclusion, we reported the enhancement of photoluminescence quantum yield by sub-bandgap absorption and emission. This enhanced emission leads to the potential for overestimation in solar cell V_{OC} when pairing PLQY with the SQ-limited radiative V_{OC}. We have demonstrated the utility of a simple calculation for V_{OC} from PLQY in the presence of tail states by either considering the fraction of luminescence that is emitted above bandgap or using the PL peak position as an effective bandgap. Such calculations may be done on absorbers rather than full devices and are amenable to rapid screening of inherent material quality and potential. We have demonstrated that most of the voltage losses in solution-processed thin-film absorbers from both the chalcogenides and hybrid perovskites can be attributed to significant non-radiative recombination. This powerful technique is important for the accurate appraisal of materials with non-ideal absorption and will facilitate material optimization in a wide range of solar cell

absorber technologies. The technique is complementary to the full-spectrum fit presented in Chapter 3. The analysis of PLQY is extremely fast (on the order of seconds) compared to the full-spectrum fit, but the analysis is less information rich. One can implement an initial screening using PLQY to identify materials/processing conditions of interest and then follow up with more extensive analysis using the full-spectrum fit on select samples.

The heretofore-developed models for gauging optoelectronic quality of PV absorber materials allow us to tackle a diverse set of problems holding back PV technologies from realizing their potential. The next chapter will describe one such study that utilizes PL imaging techniques to better understand the limitations of the hybrid perovskite family of solar cell absorbers.

Chapter 6. BIAS-DRIVEN DEGRADATION IN HYBRID PEROVSKITES

6.1 INTRODUCTION

The preceding chapters have highlighted a few potential loss mechanisms in solar cells that can significantly limit device voltage, a concern that is especially relevant in kesterite solar cells. These factors also provide a framework to identify attractive properties in prospective solar cell absorber layers. We would like a material with limited sub-bandgap absorption but a sharp onset of strong absorption at the bandgap. It should also have high radiative efficiency. In essence, we want analogs to GaAs or others in the III-V family. Adding in financial concerns, we would like a technology that is solution-processable or otherwise inexpensive to manufacture at large scale.

The hybrid perovskite family of materials (HP) checks off all these boxes. These materials have a general chemical formula of AMX_3, where A is a small organic cation (though Cs^+ and Rb^+ have been used for inorganic perovskites), M is a metal in the 2+ oxidation state (often Pb or Sn), and X is a halide anion. They form 3D structures in which the A cation is surrounded by MX_6^{4-}octahedra. First investigated in the 1990s for use in LEDs[111,112] and thin-film transistors,[113-115] the hybrid perovskites burst onto the thin-film PV scene in 2009 as sensitizers for dye cells.[116] Though modest in efficiency (PCE = 3.8%), these initial devices based on methylammonium lead triiodide ($CH_3NH_3PbI_3$ or $MAPbI_3$) have given rise to more complex mixed cation and mixed halide perovskites that have achieved efficiencies in excess of 20%.[117] The rapid rise of hybrid perovskites can be attributed to their superlative optoelectronic properties. Photothermal deflection spectroscopy on $MAPbI_3$ has revealed a steep onset to the absorption at the bandgap and small band tailing (Urbach Energy = 15 meV).[91] In addition,

$MAPbI_3$ has exhibited photon recycling[118] as well as external PLQY in excess of 30%[119] and internal PLQY over 70%.[120] These outstanding properties have been observed in solution-processed films, and high-efficiency devices have been deposited through spincoating (the standard method), doctor blading,[121] and spraycoating.[122]

The excellent optoelectronic quality and mild solution processing (annealing temperatures below 200°C) make the hybrid perovskites attractive as the top cell in solution-processed multijunction solar cells. The bandgap of the perovskites can be readily tuned through choice of A cation[123], M cation,[124,125] and halide,[107,126] allowing for low-bandgap options around 1.25 eV for $MASnI_3$ and high bandgap options up to 2.3 eV for $MAPbBr_3$. The tunability of the bandgap allows for facile matching of the device current with crystalline Si (E_g = 1.11 eV) and CISe (E_g = 0.95 eV) bottom cells in a tandem architecture. Indeed, high efficiency tandems using a perovskite top cell have achieved efficiencies approaching or in excess of 20% on Si,[127,128] CIGS,[129-131] and even other perovskites.[132]

The rub lies in the long-term (in)stability of the hybrid perovskites.[133] The hybrid perovskites, especially $MAPbI_3$, have exhibited sensitivity to elevated temperatures,[134,135] humidity,[136,137] oxygen,[138-140] light,[141] electrical bias,[142,143] as well as concerted effects of these factors. Some high-efficiency devices have even suffered major performance losses after a week in an inert atmosphere.[144] Such instability issues draw into question the viability of the hybrid perovskites as solar cell absorber layers, as modules need to reliably produce electricity over decades with limited degradation in order to reach grid parity with traditional power sources. Recent calculations have suggested that modules with lower stability (degradation rate of 2% per year) and short lifetime (10 years) would need to have an initial efficiency of 26% and be priced at *$0* (literally giving them away!) in order to reach the DOE SunShot goal of $0.06/kWh (accounting

for installation, body-of-systems, and overhead costs).[145] For hybrid perovskites to make an impact on the PV market, significant resources must be devoted to better understanding the degradation mechanisms and improving stability.

6.2 Current Understanding of Hybrid Perovskite Degradation

6.2.1 *Mobile Ions*

Oxygen ion conduction has been observed for many years in oxide perovskites.[146,147] Similarly, ion migration plays an important role in the hybrid perovskites and their performance in optoelectronic devices. I^-, $CH_3NH_3^+$, and H^+ have all been proposed to be mobile species in $CH_3NH_3PbI_3$.[148-150] The ease of transport within the hybrid perovskites has been manifested most clearly in the hysteresis of JV measurements on completed solar cells. The JV characterization of perovskite solar cells is notoriously dependent upon scan direction, voltage scanning rate, and voltage/light soaks.[151] This hysteresis is likely due to ion migration, though the ferroelectric behavior of the methylammonium cation (MA^+)[152] and charge carrier trapping/de-trapping have also been proposed.[153] The Jinsong Huang group at the University of Nebraska has observed MA^+ migration in the presence of an electric field, which leads to the formation of a local p-i-n structure opposing the applied field.[149] Recent work from their group has also identified the migration as well as oxidation of iodide anions at the gold anode during bias application at slightly elevated temperature (330 K).[143]

Additional work by Annamaria Petrozza's group has demonstrated that the drift of mobile ions in the presence of an applied bias facilitates degradation of perovskite absorbers through a water-mediated process.[142] In their scheme, MA^+ moves in response to the applied bias (as observed in Auger electron spectroscopy), leaving behind PbI_2. Such degradation was noted through the presence of PbI_2 signatures in the PL and Raman spectra. The ability of the MA^+ to move with

an applied bias was facilitated through the hydrogen bonding of ambient water molecules to the PbI_6^{4-} octahedra, which weakened the interactions with MA^+. Presumably, their full mechanism includes the following redox reactions at the current-injecting contacts:

$$CH_3NH_3PbI_3 \rightarrow PbI_2 + CH_3NH_3^+ + I^-$$
$$2CH_3NH_3^+ + 2e^- \rightarrow 2CH_3NH_2 + H_2$$
$$2I^- \rightarrow I_2 + 2e^- \quad (6.1)$$

These applied fields also lead to changes in the recombination of charge carriers, as demonstrated through TRPL.[154]

It has also been seen that ions within the perovskites move easily under photoexcitation. Eric Hoke and coworkers in the McGehee group noted that certain alloys of $CH_3NH_3Pb(I_xBr_{(1-x)})_3$ would exhibit segregation into Br-rich and I-rich domains upon illumination.[106] Work by Dane deQuilettes in the Ginger group at UW showed that iodide was mobile under illumination even in pure $CH_3NH_3PbI_3$.[141] Furthermore, the transport of ions during the application of an external bias on perovskites has been shown to be enhanced under illumination.[155]

The ease with which ions move within the hybrid perovskites makes the materials especially susceptible to irreversible degradation under various atmospheric conditions.

6.2.2 *Degradation in Oxygen*

There has been recent work from the Haque group detailing the role of oxygen in degradation of $MAPbI_3$ through the formation of superoxide radicals.[139,140] In their proposed mechanism, photoexcited $MAPbI_3$ transfers an electron to adsorbed O_2 to form the superoxide radical. The superoxide then degrades the perovskite into methylamine and iodine gases as well as water, which can then facilitate further degradation:

$$CH_3NH_3PbI_3 \xrightarrow{h\nu} CH_3NH_3PbI_3^*$$

$$O_2 \xrightarrow{CH_3NH_3PbI_3^*} O_2^*$$

$$CH_3NH_3PbI_3 + O_2^* \rightarrow CH_3NH_2 + PbI_2 + \frac{1}{2}I_2 + H_2O$$

(6.2)

In this mechanism, the presence of light and oxygen facilitates the deprotonation of methylammonium cations and the oxidation of iodide anions. Such a pathway is particularly problematic, as encapsulation treatments to protect materials form O_2 are much more difficult than those to protect materials from water. The authors noted that the rate of degradation could be decreased through the use of mesoporous TiO_2, which acts to shuttle electrons away from the perovskite before they can be transferred to the adsorbed oxygen.

6.2.3 *Degradation in Humidity*

Water is the most studied degradation enabler of the hybrid perovskites. $CH_3NH_3PbI_3$ films that are left exposed to ambient for extended amounts of time will gradually discolor from deep brown films ($CH_3NH_3PbI_3$ E_g = 1.61 eV) to bright yellow films of PbI_2 (E_g = 2.30 eV). Researchers have proposed that water can catalytically deprotonate $CH_3NH_3^+$ in an acid-base reaction to release CH_3NH_2, HI, and PbI_2:[136]

$$n(CH_3NH_3PbI_3) + H_2O \rightarrow CH_3NH_2\uparrow + (CH_3NH_3)_{n-1}n(PbI_3)\ (H_3O)$$
$$(CH_3NH_3)_{n-1}n(PbI_3)\ (H_3O) \rightarrow (n\text{-}1)CH_3NH_3PbI_3 + HI\uparrow + PbI_2 + H_2O$$

(6.3)

Others have suggested that the formation of hydrated phases can facilitate degradation. It has been shown that in high humidity conditions, the $CH_3NH_3PbI_3$ can form both mono- and dihydrate phases:[156,157]

$$4(CH_3NH_3PbI_3)+4H_2O\leftrightarrow 4[CH_3NH_3PbI_3\cdot H_2O]\leftrightarrow (CH_3NH_3)_4PbI_6\cdot 2H_2O+3PbI_2+2H_2O$$
$$(CH_3NH_3)_4PbI_6\cdot 2H_2O_{(s)} \xrightarrow{H_2O_{(l)}} 4CH_3NH_3I_{(aq)}+PbI_{2_{(s)}}+2H_2O_{(l)} \quad (6.4)$$

Identification of the monohydrate and dihydrate species was accomplished through *in situ* XRD and spectral ellipsometry. Müller and coworkers noted that hydration took 30 minutes for the monohydrate and 120 minutes for the dihydrate for films exposed to atmospheres with relative humidity (RH) of 80%.[157] In addition, the dehydration reaction was faster than hydration, and hydrated films would readily revert to the neat perovskite under "dry" conditions (RH = 35%).

Huang and coworkers have proposed that, in ambient, the transition between the mono- and di-hydrate phases may be accompanied by production of lead hydroxide rather than lead iodide:[158]

$$4CH_3NH_3PbI_3+8H_2O\rightarrow (CH_3NH_3)_4PbI_6\cdot 2H_2O+6HI\uparrow+3Pb(OH)_2 \quad (6.5)$$

The authors left $CH_3NH_3PbI_3$ films exposed to ambient atmosphere (RH = 24%) and illumination from fluorescent lights for three weeks. These films degraded and exhibited signs of carbonates, oxides, and hydroxides in X-ray photoelectron spectroscopy (XPS) data. They proposed that, upon dehydration of the dihydrate, an under-coordinated Pb intermediate would be formed:

$$(CH_3NH_3)_4PbI_6\cdot 2H_2O\rightarrow (CH_3NH_3)_xPbI_{2+x}+(4\text{-}x)CH_3NH_2\uparrow+(4\text{-}x)HI\uparrow+2H_2O \quad (0\leq x<1) \quad (6.6)$$

This same intermediate phase was observed previously in XRD.[159] The intermediate reacts with gases in the ambient (CO_2, H_2O, and O_2) to create lead carbonates, hydroxides, and oxides:

$$2(CH_3NH_3)PbI_{2+x}+2CO_2+O_2\rightarrow 2PbCO_3+2I_2\uparrow+2xCH_3NH_2\uparrow+2xHI\uparrow$$
$$(CH_3NH_3)_xPbI_{2+x}+H_2O+\frac{1}{2}O_2\rightarrow Pb(OH)_2+I_2\uparrow+xHI\uparrow+xCH_3NH_2\uparrow$$
$$Pb(OH)_2\rightarrow PbO+H_2O \quad (6.7)$$

It is not clear how the dihydrate could form at the mild humidity levels in this study. Other authors suggested that the degradation in ambient was accomplished through cooperative effects of humidity and oxygen, as films exposed to humid nitrogen degraded only into PbI_2.[160]

Müller and coworkers observed water features in the FTIR of $CH_3NH_3PbI_3$ films exposed to humidity levels as low as 10%.[161] However, the amount of water absorbed in the films did not change until humidity levels surpassed 50%, and they estimated the perovskites could house one water molecule per two unit cells (not to be confused with the formation of a full hydrate). In addition, they observed that the photoconductivity of their films increased upon exposure to oxygen or water (the greatest conductivity being observed in the presence of both).

6.2.4 *Degradation Mechanisms Involving Bias, Light, and Ambient Atmosphere*

Though there has been extensive research into different degradation mechanisms of $CH_3NH_3PbI_3$, there remains a need for a comprehensive study connecting the concerted effects of bias, light, and atmosphere on stability. In addition, the studies to date have predominately focused on pure $CH_3NH_3PbI_3$. The best power conversion efficiencies have been observed from absorbers with mixed organic and halide groups.[14,162] Furthermore, alternative perovskite stoichiometries will be required to tune the bandgap to optimize its integration into a tandem device with Si or CISe. In addition, recent work from the Grätzel group suggests that judicious selection of the group I cation can allow for improved stability and reduced hysteresis.[163]

In the following experiments, we elucidate the behavior of $CH_3NH_3PbI_3$ under the application of bias, photoexcitation, and different atmospheres. We also briefly explore the influence of composition on the degradation of higher bandgap perovskites.

6.3 Experimental Section

6.3.1 *Materials*

CsI and PbI_2 were purchased from Sigma-Aldrich (99.999% purity), while CH_3NH_3I (MAI) was synthesized through previously established protocol.[164] Briefly, methylamine (40% in H_2O) was reacted with hydroiodic acid (57 wt% in H_2O) in a round bottom flask while cooled to 0°C for 2 hours under continuous stirring. The solvent was driven off by heating to 50°C in a thermal jacket, and the resulting MAI crystals were re-dissolved in anhydrous ethanol and washed with diethyl ether. This washing process was repeated three times, and the isolated white powder was dried in a vacuum oven at 60°C for one day. CH_3NH_3Br was synthesized in an analogous procedure from hydrobromic acid. Formamidinium iodide ($CH(NH_2)_2I$ or FAI) was purchased from Dyesol.

6.3.2 *Lateral Device Microfabrication*

Lateral devices with back contact architecture were fabricated at the Washington Nanotechnology Facility (WNF) using photolithography and liftoff. Contact designs were prepared in Layout Editor (Juspertor) and used to pattern a Cr mask on a Heidelberg Direct Write μPG101 Laser Mask Writer. The pattern consisted of seven one inch-by-one inch substrates with two distinct designs. One design has ten isolated electrode pairs, and the individual electrode pairs have a small (10 μm, 50 μm, or 100 μm) channel between the electrodes, as shown in Figure 6.1a. An alternative architecture features two back contacts with interdigitated fingers along the length of the substrate, as shown in Figure 6.1b. The channel width between the interdigitated fingers was chosen to be 20 μm or 50 μm. The interdigitated devices were utilized to degrade large areas for easier characterization.

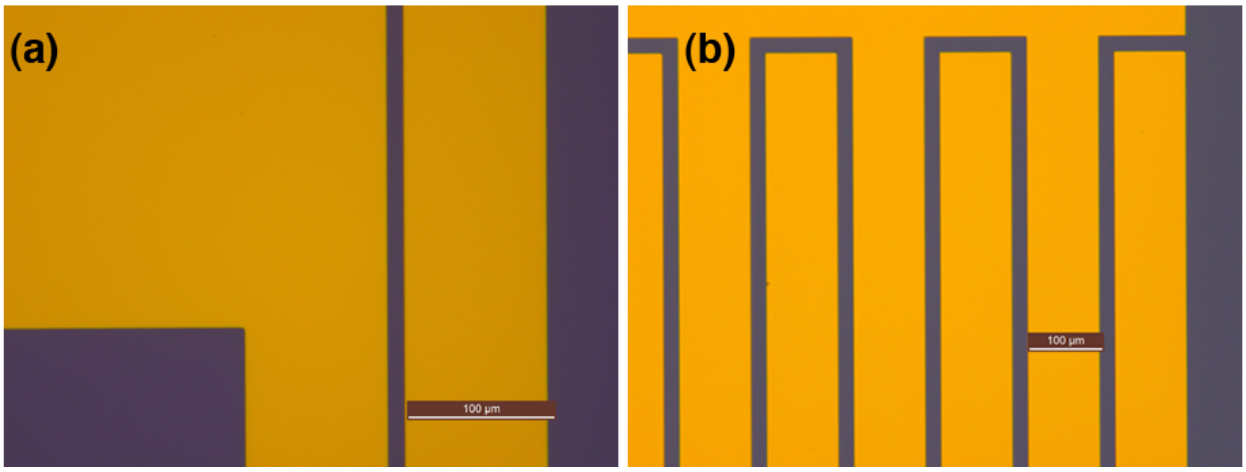

Figure 6.1. Lateral device architectures. (a) Isolated channel configuration and (b) Interdigitated finger configuration.

100mm Si wafers (purchased from the WNF) were coated with a thin layer NR9 negative photoresist (3000py) through spincoating followed by a post-bake at 150°C for one minute. The photoresist was exposed for 40 s under UV excitation in an ABM contact aligner. The resist was then baked for an additional 40 s at 110°C before being developed with AD10 (3:1 mixture with water) for 40 s. The wafers were then coated either with 10 nm Ti (adhesion layer) and 150 nm of Au through e-beam evaporation or with 150 nm of ITO through RF sputtering. The devices were finished by exposing the wafer to an acetone bath, which lifted off unwanted material and left the electrodes in place. The wafers were cleaved to yield one-inch by one-inch substrates for deposition of perovskite absorbers. These substrates were then sonicated for 10 minutes in the following sequence of solvents: detergent, deionized water, acetone, and isopropanol. They were then dried and cleaned in an O_2 plasma for 10 minutes. Finally, the devices had the contact pads covered with Kapton tape before perovskite deposition to allow for easy electrical contact in subsequent experiments.

6.3.3 *Perovskite Thin-film Deposition*

The single-step, solvent engineering technique was used to deposit thin films of $MAPbI_3$ on the substrates.[165] A 1M solution of PbI_2 and MAI (1:1 molar ratio) was prepared in a 7:3 (volume ratio) γ-butyrolactone : DMSO mixture. Inks were spincoated using a 3-step profile in an inert-atmosphere glovebox. 150μL of ink was added to the substrate, after which the samples were spun at 500RPM for 5s. This was followed by a longer step at 1000RPM for 60 s. Finally, a 5000RPM step for 45 s was used to finish films. During the last 20s of the final step, 2.2 mL of anhydrous toluene was dispensed over the spinning substrate to replace the high boiling point solvent with the more volatile toluene. Substrates were then annealed at 100°C on a hotplate for 10 minutes.

6.3.4 *Bias Application to Lateral Devices*

Samples were transferred from the glovebox to a Linkam temperature controlled probe stage (LTSE420-P), and the micromanipulators were contacted to one of the lateral devices. The stage was then purged with dry N_2 from a liquid N_2 dewar for 30 minutes. For devices tested under inert atmosphere, no further gas treatment was needed. For devices tested under ambient conditions, the top of the stage was opened such that the device was exposed to ambient atmosphere for one hour. For devices tested under O_2 atmosphere, the Linkam stage was connected to an O_2 cylinder and purged for one hour with pure O_2. For all gas treatments, the perovskite devices were kept in the dark to avoid unintentional degradation before testing.

Once the devices were pre-treated with the desired atmosphere, the Linkam stage was connected to a Keithley 2240 source-measure unit, which could apply voltages up to 60 V. Devices were exposed to applied biases on the order to those felt in perovskite solar cells (1 V over 300 nm thick absorber would correspond to a field of roughly 3V/μm). For the majority of

devices tested in these experiments, a field of 1V/μm was used (50V for the 50 μm channels). The biases were applied for durations ranging from 50 s to 10 minutes for the longer exposure studies.

6.3.5 *Widefield PL Characterization*

A custom Olympus widefield microscope was used to document changes in morphology and optoelectronic quality during bias application. Illumination was provided by a Lumencor Spectra light engine that drives a set of five LEDs (violet, blue, green, red and NIR). All devices except for $CH_3NH_3PbBr_3$ were excited using the red LED. The high bandgap of the pure bromide device (E_g = 2.3 eV) necessitated use of the violet LED. One-sun equivalent illumination was focused through Mitutoyo Plan Apo NIR infinity-corrected objectives (5x, 10x, and 100x magnification), and the emitted light was collected in an epi configuration. The brightfield and PL images were recorded on a Hamamatsu CMOS camera (QE-enhanced ORCA-Flash4.0 V2). Brightfield and PL images were collected before and after bias application for each device at both the 10x and 100x magnification. PL videos were recorded during bias application at 500 ms increments over 50 s or 100 s total bias application. For longer degradation studies, PL images were collected every 10 s over the course of 10 minutes. All degradation movies of individual devices were collected on the 100x objective. Degradation of interdigitated devices was carried out using the 10x objective to expose a larger region of perovskite to light and bias.

6.3.6 *XPS Characterization for Compositional Analysis*

XPS spectra were collected using the Kratos AXIS Ultra DLD instrument in the NESAC/BIO surface analysis facility at UW. The Kratos instrument has a hemispherical analyzer and a monochromatic Al Kα x-ray gun. The XPS Pb 4*f*, I 3*d*, O 1*s*, N 1*s*, and C 1*s* peaks were

collected at high resolution and fit using the CasaXPS software (Gaussian-Lorentzian peak shape with 80% Gaussian character). Spectra were calibrated to the adventitious carbon peak at a binding energy of 285 eV.

6.4 Results and Discussion

6.4.1 *Bias Application in Ambient Atmosphere*

Under applied bias in the presence of humidity and oxygen, $CH_3NH_3PbI_3$ lateral devices exhibited degradation when exposed to one-sun illumination (Figure 6.2).

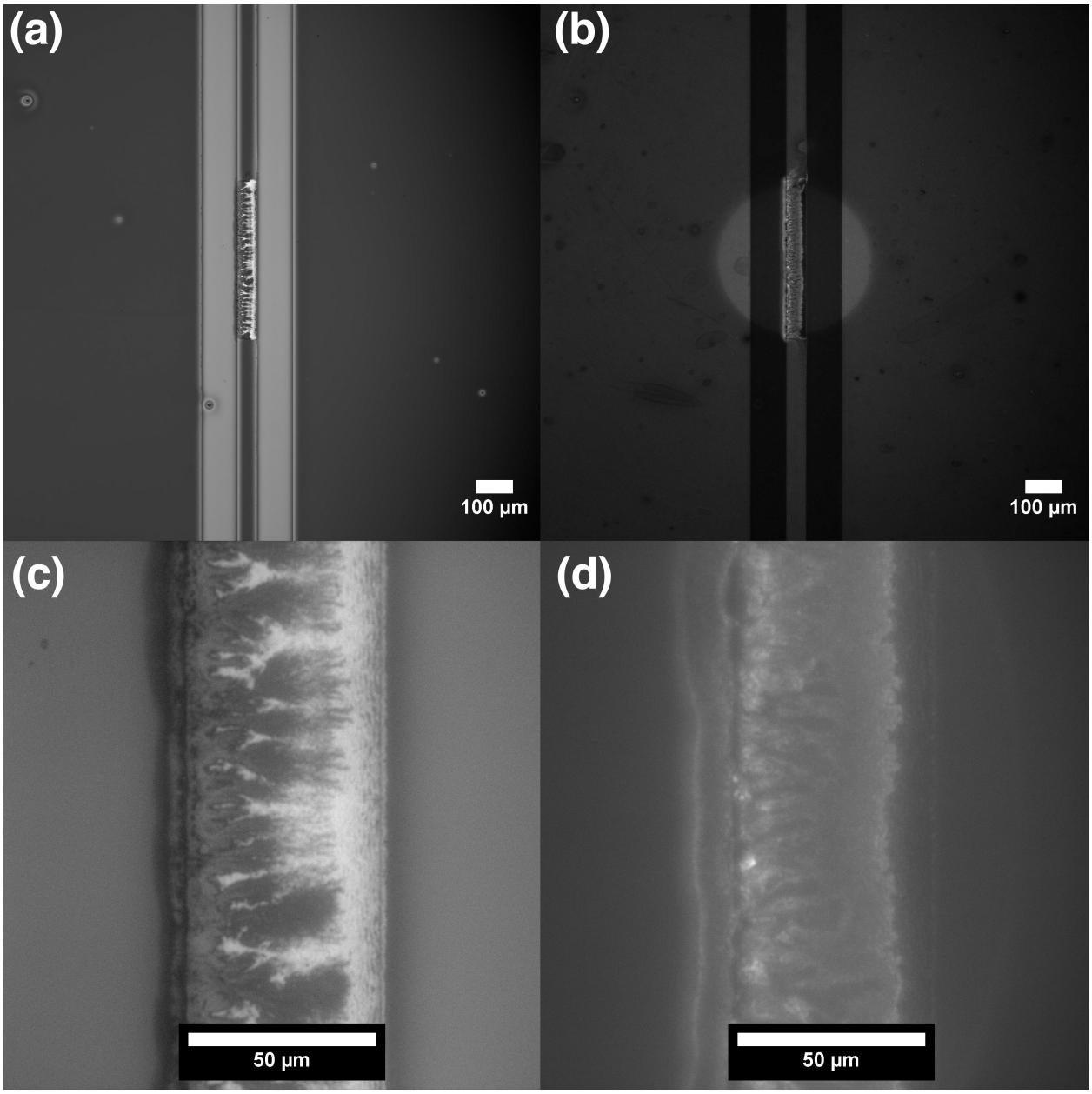

Figure 6.2. $CH_3NH_3PbI_3$ degradation in ambient. (a) Brightfield and (b) PL images of lateral device after 100 s bias application (1 V/µm) in ambient conditions at 10x magnification. 100x magnification images for (c) brightfield and (d) PL.

The degradation is localized to the area where the applied bias and photoexcitation overlapped. This detail is readily apparent in Figure 6.2b, where a circle of photobrightening is bisected by the degradation within the channel. This photobrightening is due to the excitation at 100x magnification (Figure 6.2c and d), and has been attributed by other authors to light-induced

healing of defects.[166-168] Additional experiments applying a sustained bias for 10 minutes in the dark did not result in degradation within the channel, further supporting the requirement of light and bias for degradation to occur. It has previously been shown that ion migration in the hybrid perovskites is enhanced during illumination.[155] Thus, the localization of degradation to regions experiencing both applied bias and photoexcitation may indicate that facile movement of ions across the channel is an important step in the decomposition reaction. To further investigate the potential role of ion migration in the observed decomposition, the temporal evolution of the PL intensity was recorded during bias application.

Degradation is not immediate upon bias application. Rather, it takes over 30 s from the beginning of bias application for significant changes in the PL intensity and film morphology to manifest within the channel (Figure 6.3).

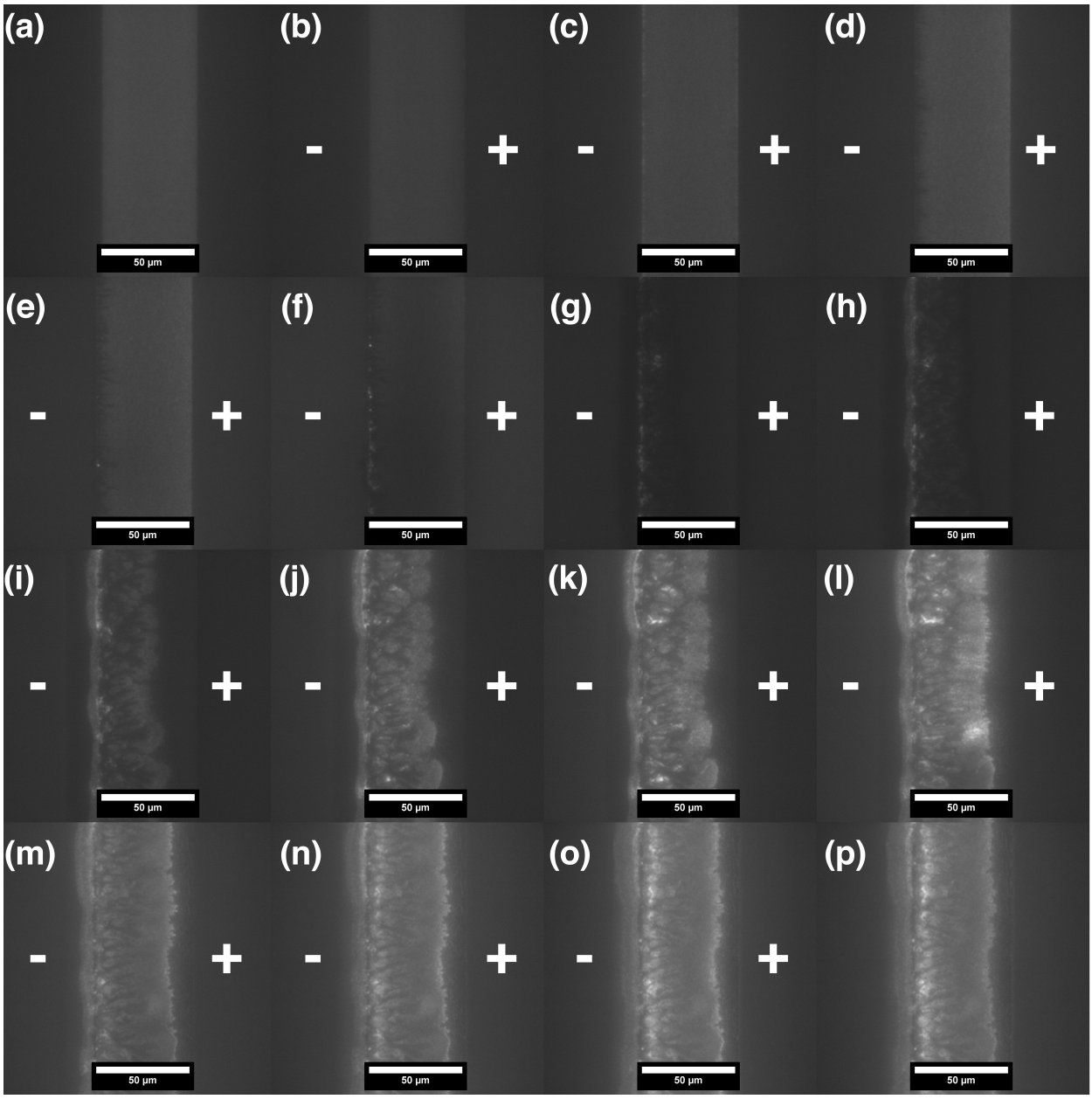

Figure 6.3. PL Time lapse of $CH_3NH_3PbI_3$ degradation in ambient. PL images for the device (a) initially and (b) upon bias application. The remaining PL images correspond to various times after the bias is turned on: (c) 1.5s, (d) 21.5s, (e) 31.5s, (f) 34.5s, (g) 36.5s, (h) 38s, (i) 44s, (j) 47.5s, (k) 50s, (l) 55s, (m) 62s, (n) 70s, (o) 100s, (p) bias off.

When the bias is turned on, there is an immediate drop of the PL intensity within the channel (Figure 6.3b). After a few seconds, the PL intensity at the negative electrode interface with the channel increases and is followed by the formation of darkened PL stripes extending from the

negative electrode into the channel. After 35 s of applied bias, hot spots in the PL appear at the negative electrode interface. These bright spots in the PL expand across the negative electrode interface before exploding into dendrites of degradation that branch through the channel. These dendrites first appear roughly 36.5s after the bias is applied, and they grow from the negative electrode to the positive electrode over the course of an additional 35s.

It is interesting to note that the degradation of the hybrid perovskite upon bias application is *not* accompanied by a sharp loss in PL intensity across the channel. While there are some areas with diminished PL, these areas are interspersed with regions that have enhanced PL as a result of the change in morphology/degradation. This observation may at first seem counterintuitive, but the result makes more sense if one decouples carrier transport from recombination. We begin by picturing regions of the perovskite where carrier transport has been cut off between grains (through degradation products forming at grain boundaries, etc.). The excited carriers cannot diffuse throughout the film and are instead localized to regions where the non-equilibrium carrier concentration can exceed that for pristine films. This carrier localization leads to enhanced PL from the isolated regions of the remaining perovskite.

6.4.2 *Effect of Atmosphere on $CH_3NH_3PbI_3$ Response to Applied Bias*

As noted previously in this chapter, the hybrid perovskites can undergo degradation mechanisms mediated by water, oxygen, and the two combined. To identify the role of the atmosphere in the degradation observed in ambient, we repeated the experiments in N_2 and O_2. The results after 100 s of bias application and one-sun illumination can be found in Figure 6.4.

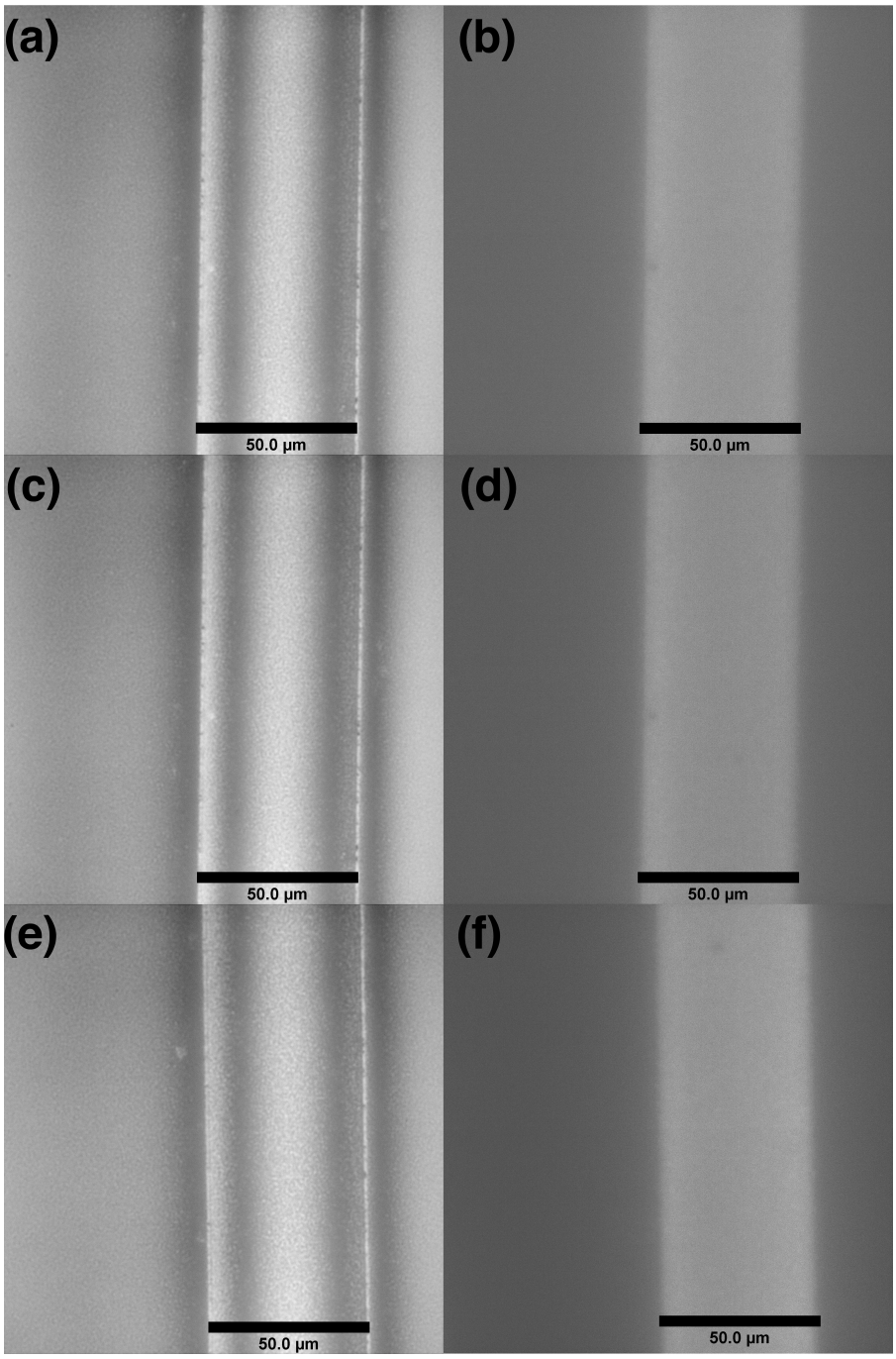

Figure 6.4. Effect of surrounding atmosphere on $CH_3NH_3PbI_3$ degradation under applied bias and photoexcitation. Representative images for the initial (a) brightfield and (b) PL for devices before bias application. (c) Brightfield and (d) PL mages after 100s bias application in N_2 atmosphere. (e) Brightfield and (f) PL images after 100s bias application in O_2 atmosphere.

The first row presents the initial brightfield and PL images of $CH_3NH_3PbI_3$ lateral devices before bias application, while the second and third row display the brightfield and PL images after 100 s of bias application in N_2 and O_2 atmospheres, respectively. There are no discernible differences between the initial images and those after bias application and photoexcitation in these two atmospheres. There was still no change in morphology/PL after an additional 10 minutes of bias and illumination. The absence of decomposition in the O_2 environment suggests that the superoxide degradation route observed by the Haque group is not operative in our experiments (at least on the relatively short timescales we are probing here).[139,140] As such, it is clear that water plays an integral role in the bias and light induced degradation observed here. This could be through an active role in the decomposition process or as a facilitator of ionic transport through its disruption of hydrogen bonding between $CH_3NH_3^+$ cations and the PbI_6^{4-} superlattice.

Note that the relative humidity levels for ambient can vary wildly from day-to-day and experiment-to-experiment. However, similar degradation in ambient was observed for devices tested on a dry winter day (RH = 10%) as well as a rainy Seattle day (RH = 50%).

To gain further insight into the degradation mechanism in our studies, we characterized the decomposition products left behind in the channel.

6.4.3 *Compositional Characterization of Degradation Products through XPS*

We attempted confocal Raman spectroscopy on degraded devices in the hopes of identifying crystalline decomposition products. However, the Raman spectra exhibited no peaks corresponding to Pb species, suggesting that the devices degraded into amorphous products. To bypass this issue, we deposited $CH_3NH_3PbI_3$ films on an interdigitated device and degraded a large area for characterization with XPS (Figure 6.5a and b).

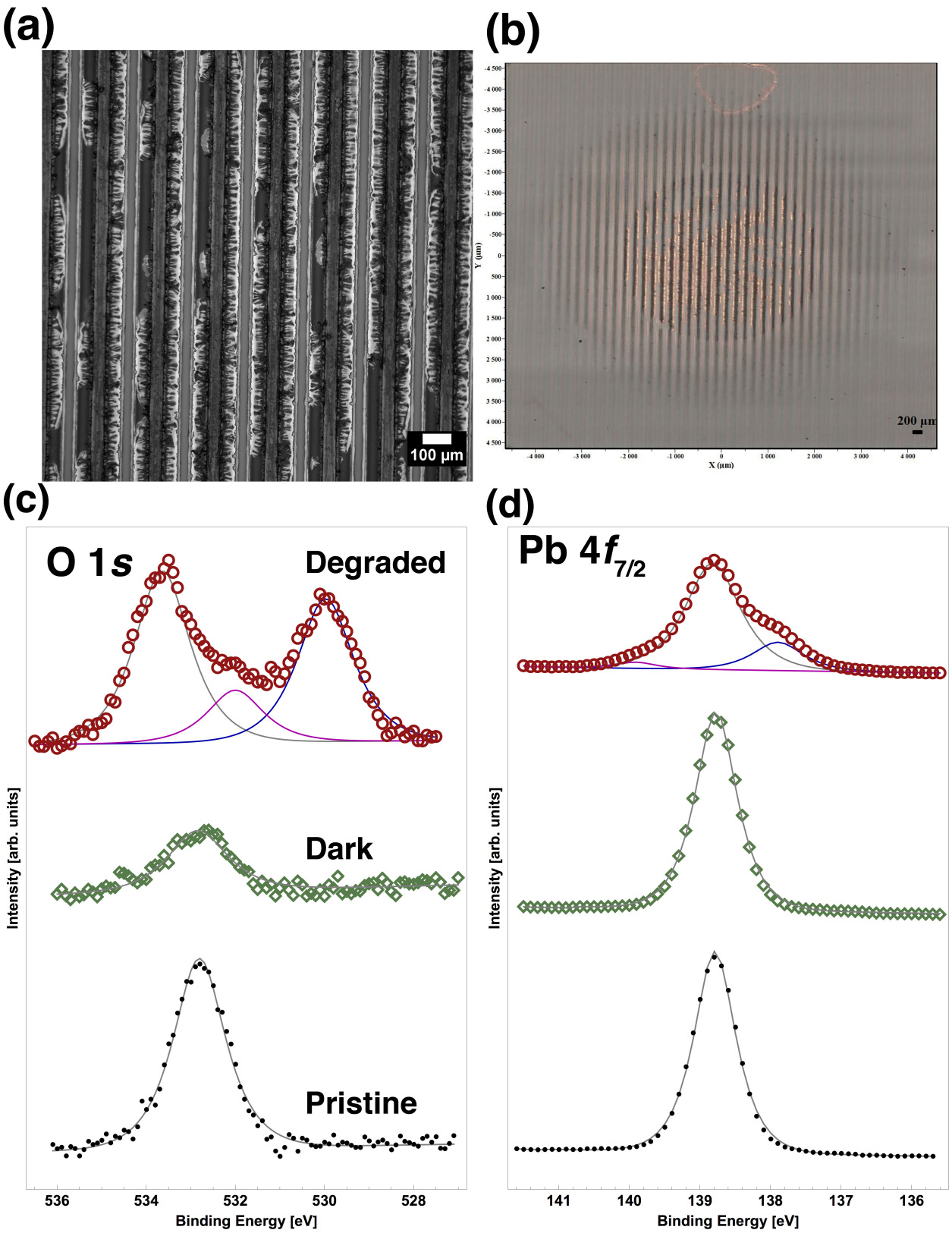

Figure 6.5. Compositional analysis of degraded $CH_3NH_3PbI_3$ devices. (a) Brightfield image of degraded interdigitated device and (b) stitched confocal image highlighting

extent of degradation. (c) XPS peaks for O 1*s* and (d) Pb $4f_{7/2}$. Spectra for the pristine devices (black filled circles), devices biased in the dark (green diamonds), and devices degraded in the light (red open circles) are offset for clarity. Fit curves are included as solid thin lines.

We collected XPS spectra off three samples: a pristine $CH_3NH_3PbI_3$ film, a region of a device that had experienced light and bias (degraded), and a region of a device that had experienced bias in the dark. All three samples exhibit the same major transition in the Pb $4f_{7/2}$ spectra at a binding energy of 138.8 eV, which can be attributed to a Pb-I bond. In addition, the sample biased in the dark and the pristine sample are largely indistinguishable. In the degraded film, this peak could correspond to PbI_2 or remaining perovskite. The degraded film has additional features at binding energies of 137.9 eV, and 139.9 eV. The lower binding energy transition has been attributed to Pb-O.[169] The higher energy shoulder has been previously attributed to $PbCO_3$, though our C 1*s* spectra do not support the presence of a carbonate.[158]

To confirm the results from the Pb spectra, we compared the O 1*s* peaks for the three samples. Even the pristine film has a strong O 1*s* peak at 532.8 eV, despite the fact that it should have experienced minimal oxidation. This could be due to adventitious contamination of the surface or pinholes in the film that allow for contributions from the SiO_2 in the substrate. The degraded film exhibits three peaks. It is likely that the transition with a binding energy of 530 eV corresponds to PbO, while the transition at a binding energy of 532 eV may be attributed to $Pb(OH)_2$.[170] The higher energy transition at a binding energy of 533.6 eV may correspond to adventitious oxygen.

These composition data suggest that decomposition of $CH_3NH_3PbI_3$ under applied bias and illumination proceeds through the generation of $Pb(OH)_2$, PbO, and PbI_2.

6.4.4 *Proposed Mechanism for Degradation under Applied Bias, Photoexcitation, and Ambient Atmosphere*

Compiling all the data collected thus far, we can build a picture of what happens to $CH_3NH_3PbI_3$ under applied bias and illumination in ambient conditions. Changes in morphology are not immediate, but rather take time to develop. These changes in morphology and PL begin at the negative electrode before extending through the channel. Decomposition requires the presence of humidity and does not occur in pure O_2 environments. Degraded films contain evidence that suggests the presence of PbI_2, $Pb(OH)_2$, and PbO.

One potential explanation of these observations is a degradation mechanism based on a local under-coordination of Pb at the negative electrode due to ion drift in the applied bias. During bias application and illumination, I^- will gradually drift towards the positive electrode, leaving behind V_{I^-} at the negative electrode (similarly we could have drift of MA^+ towards the negative electrode). The local deficiency in I^- at the negative electrode could lead to under-coordination of Pb and stimulate the formation of the PbI_{2+x}^{x-} ($0 \leq x < 1$) intermediate that Huang proposed for the dihydrate decomposition.[158] Once the under-coordinated Pb intermediate has reached a critical value of x, the degradation can proceed through the reactions in eq. 6.7.

$$\begin{gathered}(CH_3NH_3)_xPbI_{2+x}+H_2O+\frac{1}{2}O_2\rightarrow Pb(OH)_2+I_2\uparrow+xHI\uparrow+xCH_3NH_2\uparrow \\ Pb(OH)_2\rightarrow PbO+H_2O\end{gathered} \tag{6.7}$$

The decomposition is at first localized to the negative electrode interface where we have the local I^- deficiency, but it propagates through the channel as additional I^- is lost from the film as I_2 or HI.

This potential degradation pathway has major implications to optoelectronic devices based off the hybrid perovskites. During operation as solar cell absorbers, hybrid perovskites will be

exposed to light and bias. In order for devices to have long-term stability against degradation mechanisms like the one claimed here, it will be necessary to optimize encapsulation techniques (to minimize exposure of the perovskites to water and oxygen and to minimize the loss of gaseous degradation products to reduce the extent of reaction) and to develop more robust recipes for hybrid perovskites.

6.4.5 *Effect of Hybrid Perovskite Composition on Degradation under Applied Bias and Illumination*

A preliminary study has been carried out to test the effect of changing the halide or the A-site cation on the stability of hybrid perovskites to applied bias and illumination. A pure $CH_3NH_3PbBr_3$ device was fabricated on Au electrodes and excited by a violet LED. After 50s of bias and illumination in ambient conditions, the material within the channel had degraded in a manner similar to the neat iodide devices measured previously (Figure 6.6(a) and (b)).

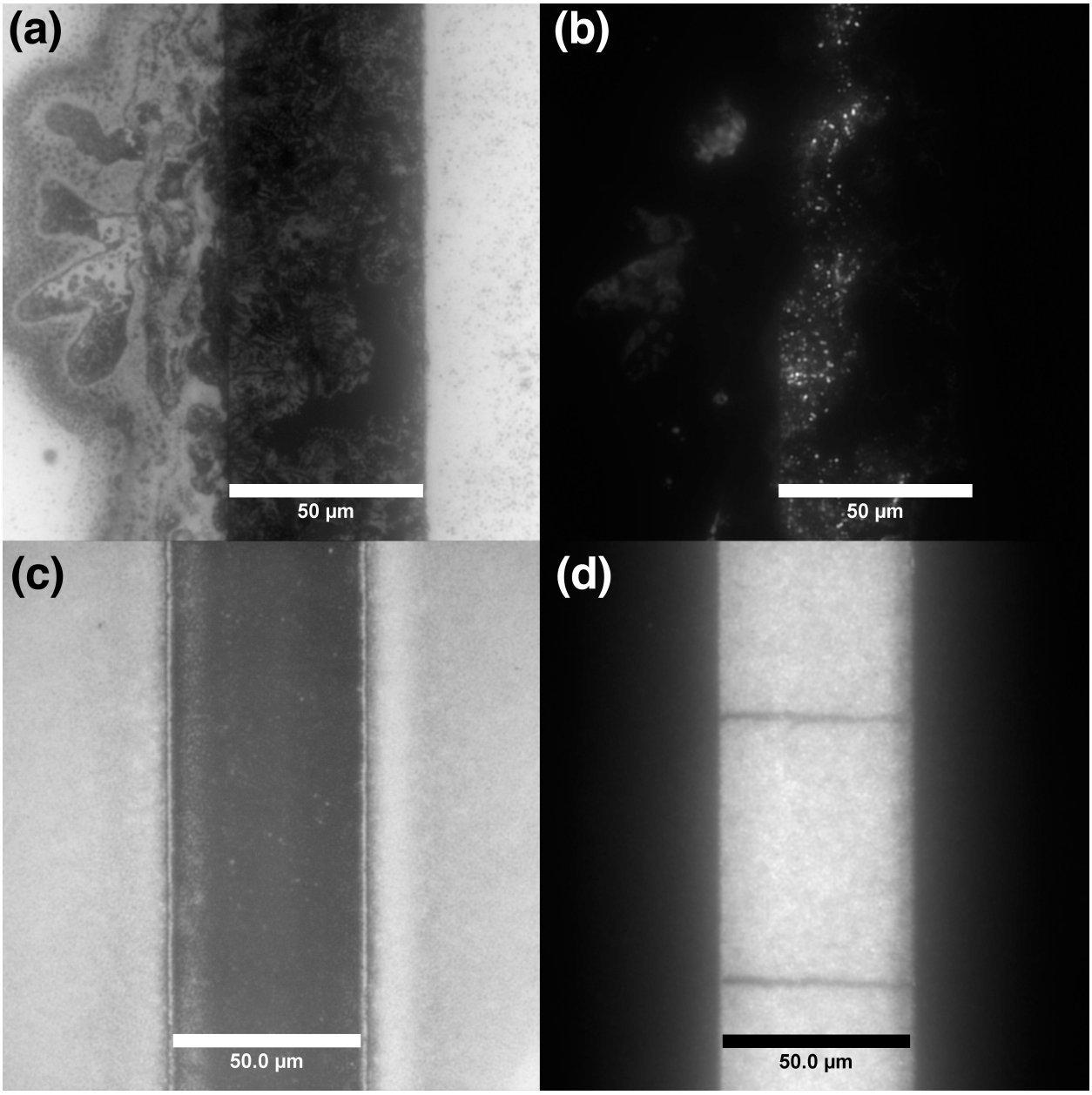

Figure 6.6. Composition dependence of perovskite degradation under applied bias and illumination in ambient conditions. (a) Brightfield and (b) PL images of a $CH_3NH_3PbBr_3$ device after 50s of bias application. (c) Brightfield and (d) PL images of $(Cs_{0.17},FA_{0.83})Pb(I_{0.6},Br_{0.4})_3$ after 10 minutes of bias and illumination in ambient.

The substitution of Br for I does not improve the stability of the lateral devices under applied bias and illumination in ambient atmosphere. The Cs-FA double cation, mixed halide device, on

the other hand, did exhibit improved stability. After 10 minutes of bias and illumination, the device exhibited no change in morphology within the channel. There were slight changes in the PL image with the extended bias (a few lines of diminished PL grew from the positive electrode to the negative electrode during the 10 minutes), but the devices did not display any irreversible decomposition. This more robust behavior may be due to reduced ion migration in these materials. It could also be due to a larger barrier for decomposition of FA^+ compared to MA^+. Additional studies must be carried out to further investigate the stability of these high-bandgap mixed cation perovskites.

6.5 CONCLUSIONS

We have highlighted the irreversible degradation of $CH_3NH_3PbI_3$ lateral devices under applied bias and illumination in ambient atmosphere. This degradation was attributed to the formation of an under-coordinated Pb intermediate due to the drift of I^- and $CH_3NH_3^+$ under applied bias. This resulted in the decomposition of the perovskite films into PbI_2, $Pb(OH)_2$, and PbO. Preliminary work showed the high-bandgap, double cation perovskites to be more resilient to such treatment, suggesting their viability as a stable top cell in a perovskite-CISe or perovskite-Si tandem solar cell.

Chapter 7. CONCLUDING REMARKS AND FUTURE DIRECTIONS

Understanding the source of losses in solar cells is essential for continued improvement in PV efficiency and affordability. During the past six years, we have developed a suite of optical characterization techniques based off of photoluminescence. A full-spectrum fit of the absolute intensity photoluminescence spectra has been used to extract the maximum attainable V_{OC} and band tail character in semiconductor thin films. In addition, two methods based on the photoluminescence quantum yield give us immediate feedback on the potential of solar cell materials without significant computation time. These PL techniques allow us to evaluate a material's optoelectronic quality without the need to fabricate a full device. As such, we now have the capability to rapidly screen the potential of new solar cell materials and processing treatments. Such techniques have become the bedrock of the Hillhouse group and have been used by others in the group to systematically investigate the effects of stoichiometry and dopants in CZTSSe[78,79] and the hybrid perovskites.[107] PL imaging has also been proven a useful tool to investigate bias-induced degradation in the hybrid perovskites. The studies described in this text merely scratch the surface of what is possible to learn from PL spectra and PLQY images, and there are many exciting opportunities to extend this work even further.

7.1 Controlling Disorder in Semiconductors

The general model of absorption presented in Chapter 3 is agnostic to the mechanism behind the band tails. However, one can gain insight into potential band tail mechanisms for specific material systems by pairing PL analysis with chemical and thermal treatments designed to intentionally change the magnitude and length scales of disorder in materials. For example, one could easily investigate changes of the exponent and energy broadening parameter at cryogenic

temperatures for the chalcogenides and perovskites. This would provide information on the tail character as we begin to freeze out sources of dynamic disorder. These experiments would also reveal trends in the quasi-Fermi level splitting as a function of temperature, which could be compared to the temperature-dependent V_{OC} from JV measurements. Adding in injection level dependence to these studies would help shed further light on factors limiting V_{OC} in these materials.[171]

In addition, the kesterites could prove to be a model system for controlling the level of disorder. Due to the similar size of Cu and Zn, there is significant antisite disorder for these two elements in CZTS. Through careful thermal treatments, it is possible to tune the level of disorder within the lattice, as evidenced by shifts in the PL peak and absorption edge.[77,172] If these thermal treatments change the length scale of disorder in CZTSSe, we may see interesting changes in the tail character of their PL. Another possibility would be to partially substitute Ag for Cu. Recent work out of IBM has demonstrated the utility of Ag alloying in narrowing the PL peak and reducing the Stokes shift.[173,174] Ag is more dissimilar in size from Zn and will not as readily switch spots in the lattice. An investigation into the tail character of these films would provide insight into disorder-induced band tails, and could highlight paths towards improving kesterite devices.

7.2 Efficacy of Encapsulation Techniques to Inhibit Perovskite Degradation

The lateral devices provide a convenient system to study the accelerated degradation of hybrid perovskites in ambient conditions. We can test the efficacy of various chemical treatments and/or encapsulation methods to inhibit or prevent degradation. It has been shown that degradation can be suppressed if the gaseous decomposition products cannot readily leave.[175] One could begin by

testing the degradation behavior after encapsulation with polymethyl methacrylate (PMMA) before moving on to more exotic encapsulants. In addition, it has been demonstrated that Lewis bases like pyridine and trioctylphosphine oxide (TOPO) can passivate the surfaces of $CH_3NH_3PbI_3$ and increase PL intensity.[119,176] By exposing perovskite films on the lateral devices to Lewis bases, it may be possible to passivate under-coordinated Pb sites and reduce ion migration. This could in turn slow down the degradation of the perovskites and increase the likelihood that they can play a role in creating a PV-powered future.

BIBLIOGRAPHY

1 Nozik, A. J. Exciton multiplication and relaxation dynamics in quantum dots: Applications to ultrahigh-efficiency solar photon conversion. *Inorganic Chemistry* **44**, 6893-6899, doi:10.1021/ic0508425 (2005).

2 *International Energy Statistics*, <http://www.eia.gov/cfapps/ipdbproject/IEDIndex3.cfm?tid=2&pid=2&aid=2> (2012).

3 Darling, S. B., You, F. Q., Veselka, T. & Velosa, A. Assumptions and the levelized cost of energy for photovoltaics. *Energy & Environmental Science* **4**, 3133-3139, doi:10.1039/c0ee00698j (2011).

4 SunShot Fact Sheet. (US Department of Energy, 2016).

5 Lazard. Levelized Cost of Energy Analysis 10.0. (2016).

6 Chung, D., Horowitz, K. & Kurup, P. (ed National Renewable Energy Laboratory) (Golden, CO, 2016).

7 Powell, D. M. *et al.* The capital intensity of photovoltaics manufacturing: barrier to scale and opportunity for innovation. *Energy & Environmental Science*, doi:10.1039/C5EE01509J (2015).

8 Carnot, N.-L.-S. *Reflections on the Motive Power of Heat*. 2nd edn, (John Wiley & Sons, 1897).

9 Rappaport, P. The Photovoltaic Effect and its Utilization. *RCA Review* **20**, 373-397 (1959).

10 Wolf, M. Limitations and Possibilities for Improvement of Photovoltaic Solar Energy Converters 1. Considerations for Earth's Surface Operation. *Proceedings of the Institute of Radio Engineers* **48**, 1246-1263, doi:10.1109/jrproc.1960.287647 (1960).

11 Shockley, W. & Queisser, H. J. Detailed balance limit of efficiency of p-n junction solar cells. *Journal of Applied Physics* **32**, 510-519, doi:10.1063/1.1736034 (1961).

12 International, A. in *Standard Tables for Reference Solar Spectral Irradiances: Direct Normal and Hemispherical on 37° Tilted Surface* (West Conshohocken, PA, 2012).

13 Green, M. A. *et al.* Solar cell efficiency tables (version 49). *Progress in Photovoltaics* **25**, 3-13, doi:10.1002/pip.2855 (2017).

14 Bi, D. *et al.* Efficient luminescent solar cells based on tailored mixed-cation perovskites. *Science Advances*, doi:10.1126/sciadv.1501170 (2016).

15 Todorov, T. K. *et al.* Beyond 11% Efficiency: Characteristics of State-of-the-Art Cu2ZnSn(S,Se)4 Solar Cells. *Advanced Energy Materials* **3**, 34-38, doi:10.1002/aenm.201200348 (2013).

16 Rau, U., Paetzold, U. W. & Kirchartz, T. Thermodynamics of light management in photovoltaic devices. *Physical Review B* **90**, doi:10.1103/PhysRevB.90.035211 (2014).

17 Ross, R. T. Some Thermodynamics of Photochemical Systems. *Journal of Chemical Physics* **46**, 4590-&, doi:10.1063/1.1840606 (1967).

18 Smestad, G. & Ries, H. Luminescence and current voltage characteristics of solar-cells and optoelectronic devices. *Solar Energy Materials and Solar Cells* **25**, 51-71, doi:10.1016/0927-0248(92)90016-i (1992).

19 Polman, A. & Atwater, H. A. Photonic design principles for ultrahigh-efficiency photovoltaics. *Nature Materials* **11**, 174-177, doi:10.1038/nmat3263 (2012).

20 Rau, U. & Kirchartz, T. On the thermodynamics of light trapping in solar cells. *Nature Materials* **13**, 103-104, doi:10.1038/nmat3837 (2014).

21 Markvart, T. The thermodynamics of optical etendue. *Journal of Optics a-Pure and Applied Optics* **10**, doi:10.1088/1464-4258/10/01/015008 (2008).

22 Yablonovitch, E., Miller, O. D. & Kurtz, S. R. in *Photovoltaic Specialists Conference (PVSC), 2012 38th IEEE* 001556-001559 (IEEE, Austin, TX, 2012).

23 Van Roosbroeck, W. & Shockley, W. Photon-Radiative Recombination of Electrons and Holes in Germanium. *Physical Review* **94**, 1558-1560, doi:10.1103/PhysRev.94.1558 (1954).

24 Lasher, G. & Stern, F. Spontaneous and Stimulated Recombination Radiation in Semiconductors. *Physical Review a-General Physics* **133**, A553-&, doi:10.1103/PhysRev.133.A553 (1964).

25 Wurfel, P. The Chemical Potential of Radiation. *Journal of Physics C-Solid State Physics* **15**, 3967-3985, doi:10.1088/0022-3719/15/18/012 (1982).

26 Rau, U. & Werner, J. H. Radiative efficiency limits of solar cells with lateral band-gap fluctuations. *Applied Physics Letters* **84**, 3735-3737 (2004).

27 Werner, J. H., Mattheis, J. & Rau, U. Efficiency limitations of polycrystalline thin film solar cells: case of Cu(In,Ga)Se2. *Thin Solid Films* **480–481**, 399-409, doi:10.1016/j.tsf.2004.11.052 (2005).

28 Mattheis, J., Rau, U. & Werner, J. H. Light absorption and emission in semiconductors with band gap fluctuations - A study on Cu(In,Ga)Se-2 thin films. *Journal of Applied Physics* **101**, doi:10.1063/1.2721768 (2007).

29 Würfel, P. *Physics of Solar Cells: From Principles to New Concepts*. 80 (Wiley-VCH, 2005).

30 Bhattacharya, R., Pal, B. & Bansal, B. On conversion of luminescence into absorption and the van Roosbroeck-Shockley relation. *Applied Physics Letters* **100**, doi:10.1063/1.4721495 (2012).

31 Urbach, F. The Long-Wavelength Edge of Photographic Sensitivity and of the Electronic Absorption of Solids. *Physical Review* **92**, 1324-1324, doi:10.1103/PhysRev.92.1324 (1953).

32 Greeff, C. W. & Glyde, H. R. Anomalous Urbach tail in GaAs. *Physical Review B* **51**, 1778-1783, doi:10.1103/PhysRevB.51.1778 (1995).

33 Sa-yakanit, V. & Glyde, H. R. Urbach Tails and Disorder. *Comments in Condensed Matter Physics* **13**, 35-48 (1987).

34 Shklovskii, B. I. & Efros, A. L. (Springer, Berlin, 1984).

35 Levanyuk, A. P. & Osipov, V. V. Edge luminescence of direct-gap semiconductors. *Uspekhi Fizicheskikh Nauk* **133**, 427-477, doi:10.3367/UFNr.0133.198103b.0427 (1981).

36 Van Mieghem, P. Theory of band tails in heavily doped semiconductors. *Reviews of Modern Physics* **64**, 755-793, doi:10.1103/RevModPhys.64.755 (1992).

37 Bonch-Bruevich, V. L. in *International Conference on the Physics of Semiconductors.* (ed A.C. Stickland) 216-219 (The Institute of Physics and the Physical Society, 1962).

38 Keldysh, L. V. in *International Conference on the Physics of Semiconductors* (The Institute of Physics and the Physical Society, Exeter, England, July 1962).

39 Kane, E. O. in *International Conference on the Physics of Semiconductors.* (ed A.C. Stickland) 252-258 (The Institute of Physics and the Physical Society).

40 Kane, E. O. Thomas-Fermi Approach to Impure Semiconductor Band Structure. *Physical Review* **131**, 79-88;, doi:10.1103/PhysRev.131.79 (1963).

41 Shklovskii, B. I. & Efros, A. L. Interband Absorption of Light in Strongly Doped Semiconductors. *Soviet Physics Jetp-Ussr* **32**, 733; (1971).

42 Dirnstorfer, I. *et al.* Characterization of CuIn(Ga)Se2 Thin Films III. In-Rich Layers. *Physica Status Solidi A* **168**, 163-175 (1998).

43 Keldysh, L. V. The Effect of a Strong Electric Field on the Optical Properties of Insulating Crystals. *Soviet Physics Jetp-Ussr* **7**, 788-790 (1958).

44 Franz, W. *Einfluß eines elektrischen Feldes auf eine optische Absorptionskante*. *Z. Naturforschung* **13a**, 484-489 (1958).

45 Tharmalingam, K. Optical Absorption in the Presence of a Uniform Field. *Physical Review* **130**, 2204;, doi:10.1103/PhysRev.130.2204 (1963).

46 Duke, C. B. & Alferief, M. E. Solvable Model of a Hydrogenic System in a Strong Electric Field: Application to Optical Absorption in Semiconductors. *Physical Review* **145**, 583, doi:10.1103/PhysRev.145.583 (1966).

47 Fox, M. *Optical Properties of Solids*. (Oxford University Press, 2001).

48 Dow, J. D., Smith, D. L. & Lederman, F. L. Acceptor-to-Band Transitions in Semiconductors: Photoluminescence, Exponential Absorption Edges, and Final-State Interactions. *Physical Review B* **8**, 4612-4626, doi:10.1103/PhysRevB.8.4612 (1973).

49 Halperin, B. I. & Lax, M. Impurity-Band Tails in the High-Density Limit. I. Minimum Counting Methods. *Physical Review* **148**, 722;, doi:10.1103/PhysRev.148.722 (1966).

50 Lee, N. Y. *et al.* Determination of conduction band tail and Fermi energy of heavily Si-doped GaAs by room-temperature photoluminescence. *Journal of Applied Physics* **78**, 3367-3370, doi:10.1063/1.359963 (1995).

51 Siebentritt, S., Papathanasiou, N. & Lux-Steiner, M. C. Potential fluctuations in compensated chalcopyrites. *Physica B: Condensed Matter* **376–377**, 831-833, doi:10.1016/j.physb.2005.12.208 (2006).

52 Gokmen, T., Gunawan, O., Todorov, T. K. & Mitzi, D. B. Band tailing and efficiency limitation in kesterite solar cells. *Applied Physics Letters* **103**, 103506 (2013).

53 Pankove, J. I. *Optical Processes in Semiconductors*. (Dover, 1971).

54 Cody, G. D., Tiedje, T., Abeles, B., Brooks, B. & Goldstein, Y. Disorder and the Optical-Absorption Edge of Hydrogenated Amorphous Silicon. *Physical Review Letters* **47**, 1480-1483, doi:10.1103/PhysRevLett.47.1480 (1981).

55 Krustok, J., Collan, H., Yakushev, M. & Hjelt, K. The role of spatial potential fluctuations in the shape of the PL bands of multinary semiconductor compounds. *Physica Scripta* **T79**, 179-182, doi:10.1238/Physica.Topical.079a00179 (1999).

56 Leitão, J. P. *et al.* Photoluminescence and electrical study of fluctuating potentials in Cu_2ZnSnS_4-based thin films. *Physical Review B* **84**, 024120 (2011).

57 Halliday, D. P. *et al.* Luminescence of Cu2ZnSnS4 polycrystals described by the fluctuating potential model. *Journal of Applied Physics* **113**, doi:10.1063/1.4810846 (2013).

58 Kane, E. O. Thomas-Fermi Approach to Impure Semiconductor Band Structure. *Physical Review* **131**, 79, doi:10.1103/PhysRev.131.79 (1963).

59 Bekker, J., Alberts, V. & Witcomb, M. J. Influence of selenization techniques on the reaction kinetics of chalcopyrite thin films. *Thin Solid Films* **387**, 40-43, doi:10.1016/s0040-6090(01)00797-0 (2001).

60 Kirchhoff, G. Ueber das Verhältniss zwischen dem Emissionsvermögen und dem Absorptionsvermögen der Körper für Wärme and Licht. *Annalen der Physik und Chemie* **109**, 275-301 (1860).

61 Einstein, A. Quantum theory of radiation. *Physikalische Zeitschrift* **18**, 121-128 (1917).

62 Kasap, S. O. *Optoelectronics and Photonics: Principles and Practices*. 162-164 (Prentice-Hall, Inc., 2001).

63 Kennard, E. H. On the thermodynamics of fluorescence. *Physical Review* **11**, 29-38, doi:10.1103/PhysRev.11.29 (1918).

64 Kennard, E. H. On the interaction of radiation with matter and on fluorescent exciting power. *Physical Review* **28**, 0672-0683, doi:10.1103/PhysRev.28.672 (1926).

65 Bebb, H. B. & Williams, E. W. in *Transport and Optical Phenomena Semiconductors and Semimetals* (eds R.K. Willardson & Albert C. Beer) 181-320 (Academic Press, 1972).

66 Drude, P. *The Theory of Optics*. 502-505 (Longmans, Green, and Co, 1902).

67 Unold, T. & Gutay, L. in *Advanced Characterization Techniques for Thin Film Solar Cells* (eds Daniel Abou-Ras, Thomas Kirchartz, & Uwe Rau) (Wiley-VCH, 2011).

68 Rau, U., Abou-Ras, D. & Kirchartz, T. *Advanced characterization techniques for thin film solar cells*. (Wiley-VCH, 2011).

69 Bauer, G. H., Bruggemann, R., Tardon, S., Vignoli, S. & Kniese, R. Quasi-Fermi level splitting and identification of recombination losses from room temperature luminescence in Cu(In(1-x)Ga(x))Se(2) thin films versus optical band gap. *Thin Solid Films* **480**, 410-414, doi:10.1016/j.tsf.2004.11.061 (2005).

70 Xin, H., Katahara, J. K., Braly, I. L. & Hillhouse, H. W. 8% Efficient Cu2ZnSn(S,Se)4 Solar Cells from Redox Equilibrated Simple Precursors in DMSO. *Advanced Energy Materials*, doi:10.1002/aenm.201301823 (2014).

71 Guo, Q., Ford, G. M., Agrawal, R. & Hillhouse, H. W. Ink formulation and low-temperature incorporation of sodium to yield 12% efficient Cu(In,Ga)(S,Se)2 solar cells from sulfide nanocrystal inks. *Progress in Photovoltaics: Research and Applications* **21**, 64-71, doi:10.1002/pip.2200 (2013).

72 Casey, H. C., Sell, D. D. & Wecht, K. W. Concentration dependence of the absorption coefficient for n- and p-type GaAs between 1.3 and 1.6 eV. *Journal of Applied Physics* **46**, 250-257, doi:10.1063/1.321330 (1975).

73 Shen, C. C., Pande, K. P. & Pearson, G. L. Electron diffusion lengths in liquid-phase epitaxial p-GaAs:Ge layers determined by electron-beam-induced current method. *Journal of Applied Physics* **53**, 1236-1237, doi:10.1063/1.330536 (1982).

74 Persson, C. Electronic and optical properties of Cu2ZnSnS4 and Cu2ZnSnSe4. *Journal of Applied Physics* **107**, doi:10.1063/1.3318468 (2010).

75 Williams, E. W. & Bebb, H. B. in *Transport and Optical Phenomena Semiconductors and Semimetals* (eds R.K. Willardson & Albert C. Beer) 321-392 (Academic Press, 1972).

76 Choubrac, L. *et al.* Multinuclear (Zn-67, Sn-119 and Cu-65) NMR spectroscopy - an ideal technique to probe the cationic ordering in Cu2ZnSnS4 photovoltaic materials. *Physical Chemistry Chemical Physics* **15**, 10722-10725, doi:10.1039/c3cp51320c (2013).

77 Scragg, J. J. S., Choubrac, L., Lafond, A., Ericson, T. & Platzer-Bjorkman, C. A low-temperature order-disorder transition in Cu2ZnSnS4 thin films. *Applied Physics Letters* **104**, doi:10.1063/1.4863685 (2014).

78 Collord, A. D., Xin, H. & Hillhouse, H. W. Combinatorial Exploration of the Effects of Intrinsic and Extrinsic Defects in $Cu_2ZnSn(S,Se)_4$. *IEEE Journal of Photovoltaics* **5**, 288-298, doi:10.1109/jphotov.2014.2361053 (2015).

79 Collord, A. D. & Hillhouse, H. W. Germanium Alloyed Kesterite Solar Cells with Low Voltage Deficits. *Chemistry of Materials* **28**, 2067-2073, doi:10.1021/acs.chemmater.5b04806 (2016).

80 Nayak, P. K., Garcia-Belmonte, G., Kahn, A., Bisquert, J. & Cahen, D. Photovoltaic efficiency limits and material disorder. *Energy & Environmental Science* **5**, 6022-6039, doi:10.1039/c2ee03178g (2012).

81 Kirchartz, T., Rau, U., Kurth, M., Mattheis, J. & Werner, J. H. Comparative study of electroluminescence from Cu(In,Ga)Se-2 and Si solar cells. *Thin Solid Films* **515**, 6238-6242, doi:10.1016/j.tsf.2006.12.105 (2007).

82 Yao, J. Z. *et al.* Quantifying Losses in Open-Circuit Voltage in Solution-Processable Solar Cells. *Physical Review Applied* **4**, doi:10.1103/PhysRevApplied.4.014020 (2015).

83 Tiedje, T. Band tail recombination limit to the output voltage of amorphouse-silicon solar-cells. *Applied Physics Letters* **40**, 627-629, doi:10.1063/1.93168 (1982).

84 Ding, D., Johnson, S. R., Yu, S. Q., Wu, S. N. & Zhang, Y. H. A semi-analytical model for semiconductor solar cells. *Journal of Applied Physics* **110**, doi:10.1063/1.3671061 (2011).

85 Green, M. A. *Solar Cells: Operating Principles, Technology, and System Applications*. (Prentice Hall, 1981).

86 Kapadia, R. *et al.* A direct thin-film path towards low-cost large-area III-V photovoltaics. *Scientific Reports* **3**, doi:10.1038/srep02275 (2013).

87 Sutter-Fella, C. M. *et al.* High Photoluminescence Quantum Yield in Band Gap Tunable Bromide Containing Mixed Halide Perovskites. *Nano Letters* **16**, 800-806, doi:10.1021/acs.nanolett.5b04884 (2016).

88 McCarthy, R. *The Fabrication and Characterization of Double Gyroid and Thin Film Photovoltaics* Doctor of Philosophy thesis, Purdue University, (2012).

89 Jackson, W. B., Amer, N. M., Boccara, A. C. & Fournier, D. Photothermal deflection spectroscopy and detection. *Applied Optics* **20**, 1333-1344, doi:10.1364/ao.20.001333 (1981).

90 Jackson, W. B. & Amer, N. M. Direct measurement of gap-state absorption in hydrogenated amorphous silicon by photothermal deflection spectroscopy. *Physical Review B* **25**, 5559-5562, doi:10.1103/PhysRevB.25.5559 (1982).

91 De Wolf, S. *et al.* Organometallic Halide Perovskites: Sharp Optical Absorption Edge and Its Relation to Photovoltaic Performance. *Journal of Physical Chemistry Letters* **5**, 1035-1039, doi:10.1021/jz500279b (2014).

92 Abdi-Jalebi, M. *et al.* Impact of Monovalent Cation Halide Additives on the Structural and Optoelectronic Properties of $CH_3NH_3PbI_3$ Perovskite. *Advanced Energy Materials*, doi:10.1002/aenm.201502472 (2016).

93 Vanecek, M. & Poruba, A. Fourier-transform photocurrent spectroscopy of microcrystalline silicon for solar cells. *Applied Physics Letters* **80**, 719-721, doi:10.1063/1.1446207 (2002).

94 Main, C., Bruggemann, R., Webb, D. P. & Reynolds, S. Determination of gap-state distributions in amorphouse-semiconductors from transient photocurrents using a Fourier-transform technique. *Solid State Communications* **83**, 401-405, doi:10.1016/0038-1098(92)90076-l (1992).

95 Unold, T., Berkhahn, D., Dimmler, B. & Bauer, G. H. in *16th European Photovoltaic Solar Energy Conference.* 736-739.

96 Katahara, J. K. & Hillhouse, H. W. Quasi-Fermi Level Splitting and Sub-Bandgap Absorptivity from Semiconductor Photoluminescence. *Journal of Applied Physics* **116**, 173504, doi:10.1063/1.4898346 (2014).

97 Rau, U. Reciprocity relation between photovoltaic quantum efficiency and electroluminescent emission of solar cells. *Physical Review B* **76**, doi:10.1103/PhysRevB.76.085303 (2007).

98 Oliva, F. *et al.* Optical methodology for process monitoring of chalcopyrite photovoltaic technologies: Application to low cost Cu(In,Ga)(S,Se)2 electrodeposition based processes. *Solar Energy Materials and Solar Cells*, doi:http://dx.doi.org/10.1016/j.solmat.2015.12.036 (2016).

99 Brown, G. *et al.* Quantitative imaging of electronic nonuniformities in Cu(In, Ga)Se-2 solar cells. *Journal of Applied Physics* **108**, doi:10.1063/1.3485814 (2010).

100 Xin, H., Katahara, J. K., Braly, I. L. & Hillhouse, H. W. 8% Efficient Cu2ZnSn(S,Se)(4) Solar Cells from Redox Equilibrated Simple Precursors in DMSO. *Advanced Energy Materials* **4**, doi:10.1002/aenm.201301823 (2014).

101 Wang, W. *et al.* Device Characteristics of CZTSSe Thin-Film Solar Cells with 12.6% Efficiency. *Advanced Energy Materials* (2013).

102 Xin, H. *et al.* Lithium-doping inverts the nanoscale electric field at the grain boundaries in Cu2ZnSn(S,Se)(4) and increases photovoltaic efficiency. *Physical Chemistry Chemical Physics* **17**, 23859-23866, doi:10.1039/c5cp04707b (2015).

103 Green, M. A., Emery, K., Hishikawa, Y., Warta, W. & Dunlop, E. D. Solar cell efficiency tables (version 47). *Progress in Photovoltaics* **24**, 3-11, doi:10.1002/pip.2728 (2016).

104 Tress, W. *et al.* Predicting the Open-Circuit Voltage of CH3NH3PbI3 Perovskite Solar Cells Using Electroluminescence and Photovoltaic Quantum Efficiency Spectra: the Role of Radiative and Non-Radiative Recombination. *Advanced Energy Materials*, n/a-n/a, doi:10.1002/aenm.201400812 (2014).

105 Vandewal, K., Tvingstedt, K., Gadisa, A., Inganas, O. & Manca, J. V. On the origin of the open-circuit voltage of polymer-fullerene solar cells. *Nature Materials* **8**, 904-909, doi:10.1038/nmat2548 (2009).

106 Hoke, E. T. *et al.* Reversible photo-induced trap formation in mixed-halide hybrid perovskites for photovoltaics. *Chemical Science*, doi:10.1039/C4SC03141E (2014).

107 Braly, I. L. & Hillhouse, H. W. Optoelectronic Quality and Stability of Hybrid Perovskites from MAPbI3 to MAPbI2Br Using Composition Spread Libraries. *Journal of Physical Chemistry C*, doi:10.1021/acs.jpcc.5b10728 (2015).

108 Uhl, A. R., Katahara, J. K. & Hillhouse, H. W. Molecular-ink route to 13.0% efficient low-bandgap CuIn(S, Se)(2) and 14.7% efficient Cu(In, Ga)(S, Se)(2) solar cells. *Energy & Environmental Science* **9**, 130-134, doi:10.1039/c5ee02870a (2016).

109 Zuo, F. *et al.* Binary-Metal Perovskites Toward High-Performance Planar-Heterojunction Hybrid Solar Cells. *Advanced Materials*, n/a-n/a, doi:10.1002/adma.201401641 (2014).

110 Yang, Z. *et al.* Effects of formamidinium and bromide ion substitution in methylammonium lead triiodide toward high-performance perovskite solar cells. *Nano Energy* **22**, 328-337, doi:doi:10.1016/j.nanoen.2016.02.033 (2016).

111 Era, M., Morimoto, S., Tsutsui, T. & Saito, S. Organic-Inorganic Heterostructure Electroluminescent Device Using a Layered Perovskite Semiconductor $(C_6H_5C_2H_4NH_3)_2PbI_4$. *Applied Physics Letters* **65**, 676-678, doi:10.1063/1.112265 (1994).

112 Hattori, T., Taira, T., Era, M., Tsutsui, T. & Saito, S. Highly efficient electroluminescence from a heterostructure device combined with emissive layered-perovskite and an electron-transporting organic compound. *Chemical Physics Letters* **254**, 103-108, doi:10.1016/0009-2614(96)00310-7 (1996).

113 Mitzi, D. B. in *Functional Hybrid Materials* (eds Pedro Gomez-Romero & Clement Sanchez) Ch. 10, 347-386 (WILEY-VCH, 2005).

114 Kagan, C. R., Mitzi, D. B. & Dimitrakopoulos, C. D. Organic-inorganic hybrid materials as semiconducting channels in thin-film field-effect transistors. *Science* **286**, 945-947, doi:10.1126/science.286.5441.945 (1999).

115 Mitzi, D. B., Dimitrakopoulos, C. D. & Kosbar, L. L. Structurally tailored organic-inorganic perovskites: Optical properties and solution-processed channel materials for thin-film transistors. *Chemistry of Materials* **13**, 3728-3740, doi:10.1021/cm010105g (2001).

116 Kojima, A., Teshima, K., Shirai, Y. & Miyasaka, T. Organometal halide perovskites as visible-light sensitizers for photovoltaic cells. *Journal of the American Chemical Society* **131**, 6050-6051, doi:10.1021/ja809598r (2009).

117 Saliba, M. *et al.* Incorporation of rubidium cations into perovskite solar cells improves photovoltaic performance. *Science* **354**, 206-209, doi:10.1126/science.aah5557 (2016).

118 Pazos-Outon, L. M. *et al.* Photon recycling in lead iodide perovskite solar cells. *Science* **351**, 1430-1433, doi:10.1126/science.aaf1168 (2016).

119 deQuilettes, D. W. *et al.* Photoluminescence Lifetimes Exceeding 8 mu s and Quantum Yields Exceeding 30% in Hybrid Perovskite Thin Films by Ligand Passivation. *Acs Energy Letters* **1**, 438-444, doi:10.1021/acsenergylett.6b00236 (2016).

120 Richter, J. M. *et al.* Enhancing photoluminescence yields in lead halide perovskites by photon recycling and light out-coupling. *Nature Communications* **7**, doi:10.1038/ncomms13941 (2016).

121 Deng, Y. H., Dong, Q. F., Bi, C., Yuan, Y. B. & Huang, J. S. Air-Stable, Efficient Mixed-Cation Perovskite Solar Cells with Cu Electrode by Scalable Fabrication of Active Layer. *Advanced Energy Materials* **6**, doi:10.1002/aenm.201600372 (2016).

122 Ishihara, H. *et al.* Nature inspiring processing route toward high throughput production of perovskite photovoltaics. *Journal of Materials Chemistry A* **4**, 6989-6997, doi:10.1039/c5ta09992g (2016).

123 McMeekin, D. P. *et al.* A mixed-cation lead mixed-halide perovskite absorber for tandem solar cells. *Science* **351**, 151-155, doi:10.1126/science.aad5845 (2016).

124 Stoumpos, C. C., Malliakas, C. D. & Kanatzidis, M. G. Semiconducting tin and lead iodide perovskites with organic cations: Phase transitions, high mobilities, and near-infrared photoluminescent properties. *Inorganic Chemistry* **52**, 9019-9038, doi:10.1021/ic401215x (2013).

125 Yang, Z. B. *et al.* Stabilized Wide Bandgap Perovskite Solar Cells by Tin Substitution. *Nano Letters* **16**, 7739-7747, doi:10.1021/acs.nanolett.6b03857 (2016).

126 Noh, J. H., Im, S. H., Heo, J. H., Mandal, T. N. & Seok, S. I. Chemical management for colorful, efficient, and stable inorganic-organic hybrid nanostructured solar cells. *Nano Letters* **13**, 1764-1769, doi:10.1021/nl400349b (2013).

127 Albrecht, S. *et al.* Monolithic perovskite/silicon-heterojunction tandem solar cells processed at low temperature. *Energy & Environmental Science* **9**, 81-88, doi:10.1039/c5ee02965a (2016).

128 Werner, J. *et al.* Efficient Monolithic Perovskite/Silicon Tandem Solar Cell with Cell Area > 1 cm(2). *Journal of Physical Chemistry Letters* **7**, 161-166, doi:10.1021/acs.jpclett.5b02686 (2016).

129 Fu, F. *et al.* Low-temperature-processed efficient semi-transparent planar perovskite solar cells for bifacial and tandem applications. *Nature Communications* **6**, doi:10.1038/ncomms9932 (2015).

130 Fu, F. *et al.* High-efficiency inverted semi-transparent planar perovskite solar cells in substrate configuration. *Nature Energy* **2**, 16190, doi:doi:10.1038/nenergy.2016.190 (2016).

131 Uhl, A., R., Yang, Z., Jen, A. K.-Y. & Hillhouse, H. W. Solution-processed chalcopyrite-perovskite tandem solar cells in bandgap-matched two- and four-terminal architectures. *Journal of Materials Chemistry A* **5**, 3214-3220, doi:**DOI:** 10.1039/C7TA00562H (2017).

132 Eperon, G. E. *et al.* Perovskite-perovskite tandem photovoltaics with optimized band gaps. *Science* **354**, 861-865, doi:10.1126/science.aaf9717 (2016).

133 Yang, J. L. & Kelly, T. L. Decomposition and Cell Failure Mechanisms in Lead Halide Perovskite Solar Cells. *Inorganic Chemistry* **56**, 92-101, doi:10.1021/acs.inorgchem.6b01307 (2017).

134 Conings, B. *et al.* Intrinsic Thermal Instability of Methylammonium Lead Trihalide Perovskite. *Advanced Energy Materials* **5**, doi:10.1002/aenm.201500477 (2015).

135 Divitini, G. *et al. In situ* observation of heat-induced degradation of perovskite solar cells. *Nature Energy* **1**, 15012, doi:doi:10.1038/nenergy.2015.12 (2016).

136 Frost, J. M. *et al.* Atomistic Origins of High-Performance in Hybrid Halide Perovskite Solar Cells. *Nano Letters* **14**, 2584-2590, doi:10.1021/nl500390f (2014).

137 Niu, G. D. *et al.* Study on the stability of CH3NH3PbI3 films and the effect of post-modification by aluminum oxide in all-solid-state hybrid solar cells. *Journal of Materials Chemistry A* **2**, 705-710, doi:10.1039/c3ta13606j (2014).

138 O'Mahony, F. T. F. *et al.* Improved environmental stability of organic lead trihalide perovskite-based photoactive-layers in the presence of mesoporous TiO2. *Journal of Materials Chemistry A* **3**, 7219-7223, doi:10.1039/c5ta01221j (2015).

139 Aristidou, N. *et al.* The Role of Oxygen in the Degradation of Methylammonium Lead Trihalide Perovskite Photoactive Layers. *Angewandte Chemie-International Edition* **54**, 8208-8212, doi:10.1002/anie.201503153 (2015).

140 Bryant, D. *et al.* Light and oxygen induced degradation limits the operational stability of methylammonium lead triiodide perovskite solar cells. *Energy & Environmental Science* **9**, 1655-1660, doi:10.1039/c6ee00409a (2016).

141 Dequilettes, D. W. *et al.* Photo-induced halide redistribution in organic-inorganic perovskite films. *Nature Communications* **7**, doi:10.1038/ncomms11683 (2016).

142 Leijtens, T. *et al.* Mapping Electric Field-Induced Switchable Poling and Structural Degradation in Hybrid Lead Halide Perovskite Thin Films. *Advanced Energy Materials* **5**, doi:10.1002/aenm.201500962 (2015).

143 Yuan, Y. *et al.* Electric-Field-Driven Reversible Conversion Between Methylammonium Lead Triiodide Perovskites and Lead Iodide at Elevated Temperatures. *Advanced Energy Materials* (2015).

144 Zhou, H. *et al.* Interface engineering of highly efficient perovskite solar cells. *Science* **345**, 542-546, doi:10.1126/science.1254050 (2014).

145 Jones-Albertus, R., Feldman, D., Fu, R., Horowitz, K. & Woodhouse, M. (ed Department of Energy) (2015).

146 Teraoka, Y., Zhang, H. M., Furukawa, S. & Yamazoe, N. Oxygen Permeation Through Perovskite-Type Oxides. *Chemistry Letters*, 1743-1746, doi:10.1246/cl.1985.1743 (1985).

147 Skinner, S. J. & Kilner, J. A. Oxygen ion conductors. *Materials Today* **6**, 30-37, doi:http://dx.doi.org/10.1016/S1369-7021(03)00332-8 (2003).

148 Eames, C. *et al.* Ionic transport in hybrid lead iodide perovskite solar cells. *Nature Communications* **6**, doi:10.1038/ncomms8497 (2015).

149 Yuan, Y. *et al.* Photovoltaic Switching Mechanism in Lateral Structure Hybrid Perovskite Solar Cells. *Advanced Energy Materials* **5**, doi:10.1002/aenm.201500615 (2015).

150 Egger, D. A., Kronik, L. & Rappe, A. M. Theory of Hydrogen Migration in Organic-Inorganic Halide Perovskites. *Angewandte Chemie-International Edition* **54**, 12437-12441, doi:10.1002/anie.201502544 (2015).

151 Unger, E. L. *et al.* Hysteresis and transient behavior in current-voltage measurements of hybrid-perovskite absorber solar cells. *Energy & Environmental Science*, doi:10.1039/C4EE02465F (2014).

152 Frost, J. M., Butler, K. T. & Walsh, A. Molecular ferroelectric contributions to anomalous hysteresis in hybrid perovskite solar cells. *Apl Materials* **2**, doi:10.1063/1.4890246 (2014).

153 Brenner, T. M., Egger, D. A., Kronik, L., Hodes, G. & Cahen, D. Hybrid organic-inorganic perovskites: low-cost semiconductors with intriguing charge-transport properties. *Nature Reviews Materials*, doi:doi:10.1038/natrevmats.2015.7 (2016).

154 Leijtens, T. *et al.* Modulating the Electron-Hole Interaction in a Hybrid Lead Halide Perovskite with an Electric Field. *Journal of the American Chemical Society* (2015).

155 Xing, J. *et al.* Ultrafast ion migration in hybrid perovskite polycrystalline thin films under light and suppression in single crystals. *Physical Chemistry Chemical Physics* **18**, 30484-30490, doi:10.1039/c6cp06496e (2016).

156 Christians, J. A., Herrera, P. A. M. & Kamat, P. V. Transformation of the Excited State and Photovoltaic Efficiency of CH3NH3PbI3 Perovskite upon Controlled Exposure to Humidified Air. *Journal of the American Chemical Society* **137**, 1530-1538, doi:10.1021/ja511132a (2015).

157 Leguy, A. M. A. *et al.* Reversible Hydration of CH(3)NH(3)Pbl(3) in Films, Single Crystals, and Solar Cells. *Chemistry of Materials* **27**, 3397-3407, doi:10.1021/acs.chemmater.5b00660 (2015).

158 Huang, W. X., Manser, J. S., Kamat, P. V. & Ptasinska, S. Evolution of Chemical Composition, Morphology, and Photovoltaic Efficiency of CH3NH3Pbl3 Perovskite

under Ambient Conditions. *Chemistry of Materials* **28**, 303-311, doi:10.1021/acs.chemmater.5b04122 (2016).

159 Yang, S. *et al.* Formation Mechanism of Freestanding CH3NH3PbI3 Functional Crystals: In Situ Transformation vs Dissolution-Crystallization. *Chemistry of Materials* **26**, 6705-6710, doi:10.1021/cm5028817 (2014).

160 Tang, X. F. *et al.* Photoinduced degradation of methylammonium lead triiodide perovskite semiconductors. *Journal of Materials Chemistry A* **4**, 15896-15903, doi:10.1039/c6ta06497c (2016).

161 Muller, C. *et al.* Water Infiltration in Methylammonium Lead Iodide Perovskite: Fast and Inconspicuous. *Chemistry of Materials* **27**, 7835-7841, doi:10.1021/acs.chemmater.5b03883 (2015).

162 Jeon, N. J. *et al.* Compositional engineering of perovskite materials for high-performance solar cells. *Nature* **517**, 476-480, doi:10.1038/nature14133 (2015).

163 Yi, C. *et al.* Entropic Stabilization of Mixed A-Cation ABX_3 Metal Halide Perovskites for High Performance Perovskite Solar CellsEntropic Stabilization of Mixed A-Cation ABX3 Metal Halide Perovskites for High Performance Perovskite Solar Cells. *Energy & Environmental Science*, doi:10.1039/C5EE03255E (2015).

164 Im, J. H., Lee, C. R., Lee, J. W., Park, S. W. & Park, N. G. 6.5% efficient perovskite quantum-dot-sensitized solar cell. *Nanoscale* **3**, 4088-4093, doi:10.1039/c1nr10867k (2011).

165 Jeon, N. J. *et al.* Solvent engineering for high-performance inorganic–organic hybrid perovskite solar cells. *Nat Mater* **13**, 897-903, doi:10.1038/nmat4014, http://www.nature.com/nmat/journal/v13/n9/abs/nmat4014.html - supplementary-information (2014).

166 Tian, Y. X. *et al.* Enhanced Organo-Metal Halide Perovskite Photoluminescence from Nanosized Defect-Free Crystallites and Emitting Sites. *Journal of Physical Chemistry Letters* **6**, 4171-4177, doi:10.1021/acs.jpclett.5b02033 (2015).

167 Galisteo-López, J. F., Anaya, M., Calvo, M. E. & Míguez, H. Environmental Effects on the Photophysics of Organic–Inorganic Halide Perovskites. *The Journal of Physical Chemistry Letters*, 2200-2205, doi:10.1021/acs.jpclett.5b00785 (2015).

168 Mosconi, E., Meggiolaro, D., Snaith, H. J., Stranks, S. D. & De Angelis, F. Light-induced annihilation of Frenkel defects in organo-lead halide perovskites. *Energy & Environmental Science* **9**, 3180-3187, doi:10.1039/c6ee01504b (2016).

169 Taylor, J. A. & Perry, D. L. An X-Ray Photoelectron and Electron-Energy Loss Study of the Oxidation of Lead. *Journal of Vacuum Science & Technology a-Vacuum Surfaces and Films* **2**, 771-774, doi:10.1116/1.572569 (1984).

170 Rondon, S. & Sherwood, P. M. A. Core Level and Valence Band Spectra of PbO by XPS. *Surface Science Spectra* **5**, 97-103 (1998).

171 Gunawan, O., Gokmen, T. & Mitzi, D. B. Suns-V-OC characteristics of high performance kesterite solar cells. *Journal of Applied Physics* **116**, doi:10.1063/1.4893315 (2014).

172 Rey, G. *et al.* The band gap of Cu2ZnSnSe4: Effect of order-disorder. *Applied Physics Letters* **105**, doi:10.1063/1.4896315 (2014).

173 Gershon, T. *et al.* Photovoltaic Materials and Devices Based on the Alloyed Kesterite Absorber (AgxCu1-x)2ZnSnSe4. *Advanced Energy Materials* **6**, doi:10.1002/aenm.201502468 (2016).

174 Chagarov, E. *et al.* Ag2ZnSn(S,Se)4: A highly promising absorber for thin film photovoltaics. *Journal of Chemical Physics* **144**, doi:10.1063/1.4943270 (2016).

175 Brinkmann, K. O. *et al.* Suppressed decomposition of organometal halide perovskites by impermeable electron-extraction layers in inverted solar cells. *Nature Communications* **8**, doi:10.1038/ncomms13938 (2017).

176 Noel, N. K. *et al.* Enhanced Photoluminescence and Solar Cell Performance via Lewis Base Passivation of Organic–Inorganic Lead Halide Perovskites. *ACS Nano*, doi:10.1021/nn5036476 (2014).

VITA

John Katahara is the only child of Lester and Janet Katahara. He spent his formative years as an Air Force brat, never living more than four years in locations such as Ohio, Utah, and Massachusetts. He spent his high school years in West Hartford, CT before studying chemical engineering at Brown University in Providence, RI. The call to graduate school brought him across the country to Seattle, WA, where he has become addicted to caffeine and good brunch food.